



ICEBE
IMAGINEERING
NATURE

Doctoral Thesis

Simulation and Optimization of Recovery Systems in the Pulp and Paper Industry

by Barbara Dorothe Weiß

carried out for the purpose of obtaining a degree of
Doctor technicae

in the
**Doctoral program in Engineering Sciences –
Chemical and Process Engineering**

submitted at
TU Wien, Faculty of Mechanical and Industrial Engineering

under the supervision of
Ao. Univ.-Prof. DI Dr. techn. Michael Harasek, TU Wien

and co-supervision of
Dr. Bahram Haddadi, TU Wien

reviewed by
Prof. Dr.-Ing. Marcus Grünewald, Ruhr-Universität Bochum

and
Ao. Univ.-Prof. DI Dr. techn. Andreas Werner, TU Wien

This research was conducted as part of the COMET Centre CHASE, funded within the COMET – Competence Centers for Excellent Technologies programme by the BMK, the BMDW and the Federal Provinces of Upper Austria and Vienna. The COMET programme is managed by the Austrian Research Promotion Agency (FFG).

Author

Barbara Dorothe Weiß
Matr. Nr.: 11938279

Supervisor

Michael Harasek
TU Wien
Institute of Chemical, Environmental and
Bioscience Engineering
Getreidemarkt 9/E166
1060 Wien, Austria

Co-Supervisor

Bahram Haddadi
TU Wien
Institute of Chemical, Environmental and
Bioscience Engineering
Getreidemarkt 9/E166
1060 Wien, Austria

Reviewers

Markus Grünewald
Ruhr University Bochum
Institute for Thermodynamics
and Fluid Dynamics
Universitätsstraße 150
44801 Bochum, Germany

Andreas Werner
TU Wien
Institute of Energy Systems
and Thermodynamics
Getreidemarkt 9/E302
1060 Wien, Austria

Affidavit

I declare in lieu of oath, that I wrote this thesis and performed the associated research myself, using only literature cited in this volume. If text passages from sources are used literally, they are marked as such. I confirm that this work is original and has not been submitted elsewhere for any examination, nor is it currently under consideration for a thesis elsewhere. I acknowledge that the submitted work will be checked electronically-technically using suitable and state-of-the-art means (plagiarism detection software). On the one hand, this ensures that the submitted work adheres to the high-quality standards of the current rules for ensuring good scientific practice "Code of Conduct" at the TU Wien. On the other hand, a comparison with other students' theses avoids violations of my personal copyright.

Vienna, June 2024

Barbara Dorothe Weiß

Kurzfassung

Die Chemikalienrückgewinnung (CRG) in der Zellstoffindustrie, in der Magnesiumbisulfit als Kochlauge zum Einsatz kommt, ist ein bewährter Prozess, der das Potenzial hat, ein nahezu geschlossener Chemikalienkreislauf zu sein. Nach der Verbrennung der Dicklauge wird Magnesiumoxid aus der Asche zurückgewonnen und zu Magnesiumhydroxid hydratisiert. In einem mehrstufigen Absorptionsprozess wird Schwefeldioxid (SO_2) mit dem zurückgewonnenen Magnesiumhydroxid aus dem Abgas absorbiert, wobei Magnesiumbisulfit entsteht, das dann wieder als Kochlauge eingesetzt wird. Suboptimale Prozessbedingungen führen allerdings häufig zu einem vermeidbaren zusätzlichen Chemikalienverbrauch, wodurch der Kreislaufcharakter des Prozesses verloren geht. Dieser zusätzliche Chemikalienverbrauch kann durch Prozessoptimierung minimiert werden. Diese Arbeit befasst sich mit der Optimierung der Chemikalienrückgewinnung in Magnesiumbisulfit-Aufschlussprozessen mithilfe von Simulation. Prozesssimulation ermöglicht es virtuelle Experimente durchzuführen und somit Prozessineffizienzen zu identifizieren und ein optimiertes Prozessdesign abzuleiten. In dieser Arbeit werden zwei Hauptquellen für den Einsatz von zusätzlichen Chemikalien und deren Minimierung betrachtet: Unerwünschte Ausfällungen im Absorptionssystem, die zu einem Chemikalienverlust führen und Rußbildung bei der Verbrennung, welche zu einem erhöhten Bedarf an Bleichmitteln bei der Zellstoffproduktion führt.

Das erste Ziel der Arbeit besteht darin, mit Hilfe von Prozesssimulation unerwünschte Ausfällungen im Prozesssystem zu detektieren und den Prozess so zu optimieren, dass Ausfällungen minimiert werden. Hierfür wurde ein thermodynamisches Prozessmodell entwickelt, das das komplexe Elektrolytsystem ($\text{MgO-CaO-SO}_2\text{-H}_2\text{O-O}_2\text{-CO}_2$) in der Chemikalienrückgewinnung beschreibt und potenzielle Ausfällungen vorhersagt. Durch die Anwendung des validierten Modells in Prozessfließbildberechnungen wurden pH-Wert, Temperatur und das Verhältnis von Mg(OH)_2 zu SO_2 als Schlüsselparameter identifiziert, die unerwünschte Niederschlagsreaktionen beeinflussen und Parametergrenzen festgelegt, bei deren Überschreitung es zu vermehrten Ausfällungen kommt. Abschließend wurde ein optimiertes Prozessdesign vorgestellt, das durch eine optimale Einstellung des $\text{Mg(OH)}_2\text{-SO}_2$ Verhältnisses eine Minimierung der Ausfällungen erreicht und somit erheblich zur Reduzierung des Chemikalienverbrauchs beiträgt.

Das zweite Ziel dieser Arbeit besteht darin, mithilfe von Computational Fluid Dynamic (CFD) Simulationen den Einfluss der Laugenzerstäubung auf die Verbrennung im Kessel zu ermitteln. Durch die Optimierung der Laugenzerstäubung in den Kessel kann die Verbrennung im Kessel optimiert werden und somit Rußbildung reduziert werden. Hierfür wurde ein CFD-Modell des Laugenkessels entwickelt, welches das Einsprühen der Lauge

und die Verbrennung im Kessel beschreibt. Im Anschluss an die Entwicklung des Modells wurde der Einfluss unterschiedlicher Sprüheigenschaften wie Partikelgröße, Sprühwinkel und Sprühform auf die Verbrennungsgeschwindigkeit in virtuellen Experimenten berechnet. Die durchgeführten Experimente ergaben, dass eine kleine Partikelgröße, ein weiter Sprühwinkel, sowie ein Hohlkegelsprühmuster gegenüber einem Vollkegelsprühmuster vorteilhaft für eine schnelle Tropfenverbrennung sind.

Die vorgestellte Forschung trägt zum Verständnis und zur Verbesserung der Chemikalienerückgewinnung in der Zellstoffindustrie bei und unterstreicht die Bedeutung einer simulationsbasierten Optimierung für nachhaltige und effiziente Prozesse. Die entwickelten Simulationsmodelle stellen Werkzeuge zur Bewertung von Prozess- und Systemdesigns dar, die über die durchgeführten Untersuchungen hinaus eingesetzt werden können. Das im Rahmen dieser Arbeit entwickelte thermodynamische Prozessmodell kann im Anlagenbetrieb, sowie in der Anlagenauslegung unterstützend eingesetzt werden. Anlagenbetreibern ermöglicht es die Betriebsgrenzen der Anlage zu finden und auf Betriebsprobleme mit einem umfassenden Verständnis des mechanistischen Zusammenspiels innerhalb des Prozesssystems zu reagieren. In der Anlagenauslegung können mit Hilfe des Modells verschiedene Prozessszenarien durchgerechnet werden und ein optimiertes Design gefunden werden, das auf die Bedürfnisse und die Infrastruktur des Anlagenbetreibers zugeschnitten ist. Mit Hilfe des im Rahmen dieser Arbeit entwickelten CFD-Modells kann ausgewertet werden, wie verschiedene Designänderungen die Strömungsverhältnisse und die Verbrennung im Kessel beeinflussen und wie effizient emissionsmindernde Maßnahmen umgesetzt werden können. Die angewandten Methoden lassen sich auch auf andere Verbrennungsszenarien übertragen. Durch die Anpassung kinetischer Parameter im Modell ist das entwickelte Simulationswerkzeug nicht auf die Verbrennung der hier untersuchten Lauge limitiert, sondern kann auch Verbrennungskessel anderer Brennstoffe abbilden.

Abstract

The chemical recovery process in the pulp industry, employing magnesium bisulfite as cooking liquor, has long been established and holds the potential to operate as a near-closed-loop system concerning chemical usage. Post-combustion of red liquor, magnesium oxide is reclaimed from the ash and hydrated into magnesium hydroxide. In a multistage absorption process, sulfur dioxide (SO_2) is extracted from exhaust gas using the recovered magnesium hydroxide, forming magnesium bisulfite, which is then reused as cooking liquor. However, suboptimal process conditions often result in avoidable additional chemical usage, compromising the closed-loop nature of the process. Hence, there is a significant opportunity for enhancing chemical recovery through process optimization. This thesis delves into optimizing chemical recovery within magnesium bisulfite pulping processes using simulation techniques. Simulation enables virtual experimentation, allowing the identification of primary process inefficiencies and the derivation of optimized process designs. This thesis addresses two main optimization potentials: minimizing unwanted precipitation in the absorption system and reducing soot formation during combustion, thereby reducing the necessity for bleaching chemicals in pulp production.

The first objective of this study is to employ process simulation to tackle unwanted precipitation in the system. A comprehensive thermodynamic process model of the chemical recovery process, encompassing the complex electrolyte system components ($\text{MgO-CaO-SO}_2\text{-H}_2\text{O-O}_2\text{-CO}_2$), was developed to predict precipitations accurately. By utilizing the validated model in process flowsheet calculations, the pH value, temperature, and Mg(OH)_2 to SO_2 ratio were identified as key parameters influencing undesired precipitation reactions, and parameter limits at which increased precipitations occur were defined. Finally, an optimized process design is presented that minimizes precipitation by optimally adjusting the $\text{Mg(OH)}_2\text{-SO}_2$ ratio, thereby significantly reducing chemical consumption.

The second objective of this thesis is to use Computational Fluid Dynamics (CFD) simulations to analyze the effect of red liquor spraying on combustion inside the furnace. By optimizing the spraying behavior, the combustion can be improved, and soot formation can be reduced. For this purpose, a CFD model of the combustion vessel was developed, which describes the spraying and combustion of red liquor. With the developed model, the influence of different spray characteristics, such as particle size, spray angle, and spray type, on the combustion speed was calculated in virtual experiments. The experiments revealed that a smaller particle size, a wider spray angle, and a hollow cone spray type, compared to a full cone spray type, are beneficial for faster droplet combustion.

This research contributes to understanding and improving chemical recovery processes in the pulp industry, emphasizing the importance of simulation-based optimization for sustainable and efficient operations.

The developed simulation models are tools for evaluating process and system designs that extend beyond the performed investigations. The thermodynamic process model developed in this work can support both plant operations and plant design. It enables plant operators to identify the operational limits of the plant and respond to operational problems with a comprehensive understanding of the mechanistic interplay within the process system. In plant design, the model allows the simulation of various process scenarios and supports finding an optimized design tailored to the needs and infrastructure of the plant operator. The developed CFD model facilitates evaluating how different design changes affect flow and combustion conditions in the furnace and how emission reduction measures can be implemented. The applied simulation approaches can be transferred to various combustion scenarios. By adjusting kinetic parameters in the model, the developed simulation tool is not limited to the combustion of the red liquor but can also simulate furnaces using other fuels.

Danksagung

Eine Dissertation ist nie nur eine individuelle Leistung, sondern immer das Ergebnis gemeinsamer Anstrengungen und glücklicher Umstände.

In diesem Sinne möchte ich an erster Stelle meinem Betreuer Michael Harasek danken für die Möglichkeit in seiner Forschungsgruppe zu arbeiten, für seine Unterstützung bei der Bearbeitung des Dissertationsthemas und dass er mich für die Welt der Prozesssimulation begeistert hat. Danke an meinen Co-Betreuer Bahram Haddadi, der mich im Abschluss der Arbeit unterstützt hat. Danke an meine Kolleg*innen an der TU Wien und bei CHASE für all die fachliche Unterstützung und die netten Gespräche zwischendurch. Durch Euch wurden alle Hürden meisterbar, Simulationscrashes erträglicher und die Arbeitstage lustiger. Besonders möchte ich Walter Wukovitz danken für die Unterstützung beim Einstieg in Aspen Plus und Karin Wieland für die nette Zusammenarbeit im Sappi-Projekt. Mein Dank gilt auch den Projektpartner*innen von Sappi für den Austausch und die Zusammenarbeit in diesem Projekt.

Ein besonderer Dank geht an Eva-Maria Wartha, die eingesprungen ist, als ich Mutter geworden bin und die Fortsetzung des Projektes sichergestellt hat. Denn Familie und Forschung gehen nur zusammen, wenn man Unterstützer*innen hat. Danke!

Thank you to all my colleagues, who became friends along the way. Thank you for making it easy to arrive in Vienna and to navigate through the joys and sorrows of life while being a PhD student. Danke! Thank you! Muchas gracias!

Und weil ohne Euch nichts geht: Danke an meine Freund*innen. Für euer offenes Ohr, die Ablenkung zur richtigen Zeit und dass ihr immer für mich da seid.

Danke an meine Familie. Meine Eltern, meine Geschwister und alle die dazu gehören.

Danke Ondra. Danke Noel.

Für alles.

Děkuji za všechno.

Contents

List of Appended Publications	XI
Research Summary	2
1 Introduction	3
2 Chemical Recovery in the Pulp Production – a Closed Loop?	5
3 Applied Approaches.....	10
3.1 Objective 1: Process Simulation to Target Precipitations	10
3.2 Objective 2: CFD Simulation to Target Soot Formation	18
4 Results – Summary of Publications	23
4.1 Objective 1: Process Simulation to Target Precipitations	23
4.2 Objective 2: CFD Simulation to Target Soot Formation	24
5 Conclusion and Outlook	25
Bibliography.....	29
List of Figures.....	31
List of Tables	32
Abbreviations and Symbols	33
Publications	34
Journal Paper I	35
Journal Paper II	53
Journal Paper III	68
Conference Paper	75
Submitted Journal Paper IV	81

List of Appended Publications

Journal Publications

Journal Paper I

Solubility Data of Potential Salts in the MgO-CaO-SO₂-H₂O-O₂ System for Process Modeling,

Barbara D. Weiß, Michael Harasek,

Processes 2021, 9, 50,

DOI: 10.3390/pr9010050

My contribution: Performing the research. Visualization of the results. Conceptualization and writing the paper.

Journal Paper II

Assessment of Modeling the MgO-CaO-CO₂-SO₂-H₂O-O₂ System Using the Electrolyte NRTL Activity Coefficient Model,

Barbara D. Weiß, Bahram Haddadi, Michael Harasek,

Industrial & Engineering Chemistry Research 2023, 62, 32, 12626–12639,

DOI: 10.1021/acs.iecr.3c00868

My contribution: Performing the research. Visualization of the results. Conceptualization and writing the paper.

Journal Paper III

Finding Optimized Process Conditions to Minimize Precipitations in an SO₂ Absorption Process Using Thermodynamic Process Simulation

Barbara D. Weiß, Wolfgang Fuchs, Michael Harasek,

Chemical Engineering Transactions 2021, 88, 535-540,

DOI: 10.3303/CET2188089

My contribution: Performing the research. Visualization of the results. Conceptualization and writing the paper.

Journal Paper IV (submitted)

Effect of Spraying Characteristics on Combustion of Red Liquor – Virtual Experiments using CFD Simulation

Barbara D. Weiß, Eva-Maria Wartha, Christian Jordan, Thomas Ladinek, Michael Harasek, Bahram Haddadi

Submitted to Applied Thermal Engineering

My contribution: Performing the research. Visualization of the results. Conceptualization and writing the paper. The simulation environment, specifically the phase change and reaction kinetics as well as the post processing of the simulation results were collaboratively developed with the second co-author.

Reviewed Conference Publication

Conference Paper I

Multistep SO₂ absorption – Making process design choices based on process simulation

Barbara D. Weiß, Bahram Haddadi, Michael Harasek,

Proceedings of the 17th Minisymposium Verfahrenstechnik and 8th Partikelforum, 2023

ISBN: 978-3-900397-08-1

My contribution: Performing the research. Visualization of the results. Conceptualization and writing the paper.

Research Summary

The main research results of this thesis are published or submitted to be published in journal and conference publications, which can be found in full length in the chapter *Publications* of this thesis. The chapter *Research Summary* provides the context and overview of those publications.

Firstly, the importance of the performed research is highlighted by introducing the circumstances, challenges, and barriers faced in transforming pulp production into a more resource-efficient and environmentally friendly process. The introduction leads to the importance of process optimization of established processes and the potential of simulation as a tool to find optimized process conditions. The introduction concludes by defining the objectives of this thesis.

This thesis focuses on the chemical recovery of magnesium bisulfite-based pulp production. Section 2 offers background information on the involved processes and explores the optimizing potential by going deeper into the objectives. Section 3 outlines the approaches applied to target the thesis' objectives. Furthermore, it gives insight into the application of the developed simulation tools at an industrial plant. Finally, section 4 summarizes the publications that constitute this thesis before a conclusion and outlook are provided in section 5.

1 Introduction

New technologies, new processes, new materials. High hopes are set on cutting-edge technologies to provide transformative solutions in tackling the climate and resource crisis. However, besides this wave of innovation, long-established processes can substantially influence reducing environmental impact when intensified and optimized. In the relentless pursuit of sustainability and efficiency, process optimization and intensification are a powerful and immediate tool for industries seeking to enhance their performance. The potential of process optimization is increasingly recognized among the research community, showing a sharp increase in publications on the topic since 2000 (Sitter et al. 2019). One of the long-established industries that can benefit from process intensification is the pulp and paper industry. 400 million tons of paper are produced globally annually (Furszyfer Del Rio et al. 2022). And even though digitalization is slowly removing paper from our offices, paper production is expected to grow to 900 Mt by 2050 due to increased demand for, e.g., packaging and hygiene products (Furszyfer Del Rio et al. 2022). Accounting for 1.1 % of direct global industrial combustion and process CO₂ emissions and being the largest final energy consumer of Austria, making up 7 % of Austria's industrial CO₂ emissions, the pulp and paper industry is both a vital economic player and a significant environmental contributor (Bashmakov et al. 2022; Furszyfer Del Rio et al. 2022). The need for capital, funding, and the potential halt in production from new technology adoption are cited as key barriers in the pulp and paper industry to transform the industry (Furszyfer Del Rio et al. 2022). With such barriers in place, optimizing and intensifying existing technologies gains in importance.

The key to performing process optimization lies in comprehending how process alterations influence overall process performance. An invaluable tool to analyze the effect of process parameters is the simulation of the process system. Thermodynamic simulations, coupled with flowsheet calculations and computational fluid dynamic simulations, offer insight into dependencies in complex systems, which couldn't be monitored without them. The development of simulations enables the performance of experiments in a virtual environment. This empowers scientists and engineers to derive optimized process designs for running industrial-sized systems without needing expensive experimental setups. Using process and computational fluid dynamic simulations, this thesis addresses the optimization of pulp production's chemical recovery. By identifying flaws in the existing process and proposing optimization strategies, we aim to contribute to the pursuit of sustainability within this industry. To achieve this, virtual experiments, facilitated by process simulation and computational fluid dynamics, are an invaluable tool.

By analyzing the chemical recovery of the pulp industry, two main optimizing potentials are identified: Avoiding precipitation during absorption and reducing soot formation during combustion. From this, two main objectives are derived for this thesis:

1. Process simulation to target precipitations in the absorption system
2. CFD Simulation to target soot formation during red liquor combustion

The following takes you through the process of addressing those objectives.

2 Chemical Recovery in the Pulp Production – a Closed Loop?

Before paper can be paper, it begins as pulp: a fibrous material obtained by breaking down cellulose-containing sources, traditionally wood or other plant materials, or recycled paper mechanically or chemically. Chemical pulping is the predominant pulping method (Pratima Bajpai 2016). During chemical pulping, lignin is dissolved under elevated temperature (up to around 180 °C) and pressure (up to around 9.5 bar) using an aqueous chemical solution, resulting in the extraction of pulp fibers. This chemical solution, known as white liquor, plays a crucial role in pulping. The type of white liquor distinguishes two primary chemical pulping methods used: Alkaline sulfate-based pulping (Kraft process) and sulfite-based pulping, with our focus on the latter. Among sulfite-based processes, magnesium sulfite pulping prevails due to its capacity for chemical recovery post-usage (Pratima Bajpai 2017). Before looking into chemical recovery in detail, we first briefly integrate the chemical recovery into the pulp production line (Figure 1).

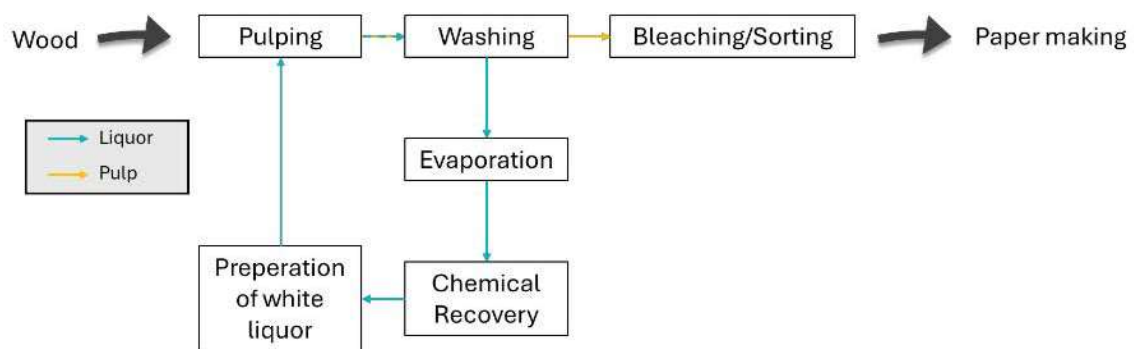


Figure 1: Main steps of the pulp production line

After pulping, the so-called red liquor is removed from the pulp through washing. The pulp undergoes further processing, including sorting and bleaching, before proceeding to the papermaking line. Bleaching is essential to achieve white paper and typically uses hydrogen peroxide, oxygen, chlorine, and other bleaching chemicals. To minimize the use of bleaching chemicals, the objective is to employ as much as necessary, as little as possible.

In addition to the utilized chemicals, the red liquor contains lignin residues and hemicellulose. Before entering the chemical recovery process, the water content of the red liquor is reduced through evaporation. The white liquor is reclaimed after chemical recovery and can be reused for pulping. Now, let us look at the chemical recovery.

Figure 2 shows a simplified flowsheet of the chemical recovery in magnesium bisulfite-based pulping processes.

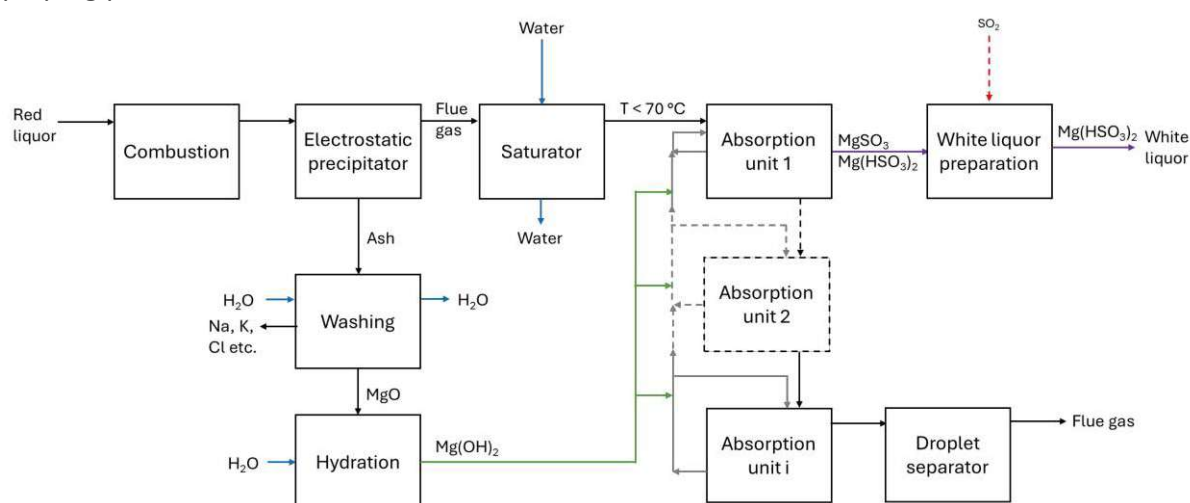
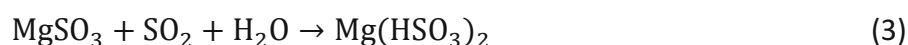
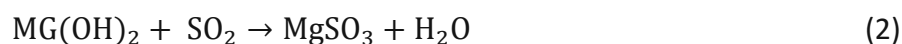
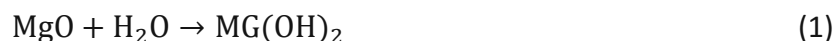


Figure 2: Simplified flowsheet of the chemical recovery in magnesium bisulfite-based pulping process

In the first step, red liquor is combusted. Magnesium bisulfite decomposes to MgO , SO_2 , O_2 , and H_2O through combustion. MgO is in the fly ash and is, subsequent combustion, separated from the gas in an electrostatic precipitation. After washing the ash to prevent accumulation of side elements such as Na, K, and Chlorides, MgO is hydrated to form magnesium hydroxide. The resulting magnesium hydroxide slurry serves as an absorbent within the chemical absorption process.

Meanwhile, the flue gas is saturated with water in a saturator and enters the absorption process. The absorption process can consist of several absorption units. In the chemical absorption process, sulfur dioxide (SO_2) is absorbed from the gas phase and reacts with the magnesium hydroxide slurry to yield magnesium sulfite. This magnesium sulfite then reacts further with SO_2 to produce magnesium bisulfite, which can be reintroduced as a cooking liquor within the pulp production process, thus establishing a closed-loop system.

Equations 1 to 3 summarize the main reactions leading to the recovery of magnesium bisulfite.



Under ideal conditions, a complete chemical recovery can be attained. However, unwanted precipitation reactions can occur under unideal process conditions besides the intended reactions. Precipitation of salts in the system highly influences the efficiency of the process. A high precipitation rate causes chemical loss as the precipitated salts will be washed out in a regular cleaning step rather than recycled in the process (Steindl et al. 2005). Uncontrolled precipitation of salts means interruption of the closed-loop process, leading to increased usage of fresh

chemicals and more frequent cleaning operations. Consequently, additional SO_2 and MgO must be introduced into the system to compensate for these losses, which reduces the economic viability of the process and challenges its ecological footprint.

Chemical losses can be compensated in various ways. They may be introduced into combustion as MgSO_4 or pure sulfur, added before hydration as MgO , or injected as SO_2 into the absorption unit. Finally, SO_2 is supplemented post-chemical recovery during white liquor preparation to ensure complete conversion from MgSO_3 to $\text{Mg}(\text{HSO}_3)_2$ and to adjust the pH of the white liquor to approximately 4.5, a prerequisite for utilizing it as cooking liquor in magnesium bisulfite pulping processes (Pratima Bajpai 2018). However, irrespective of the stage at which chemicals are introduced into the process, the guiding principle remains consistent: minimize their usage. Each additional chemical introduction disrupts the closed-loop system and challenges the ecological footprint and economic feasibility. Therefore, the overarching aim of this thesis is to minimize the necessity for adding fresh chemicals to the process. To achieve this, it is imperative to comprehend where chemical losses originate.

Precipitation in the absorption system

While equations 1 to 3 look like a straightforward, simple chain of reactions, the chemical system inside the absorption process is a complex electrolyte system in which many dissociation and precipitation reactions occur simultaneously and influence each other. Process simulation is invaluable for depicting a complex system in a process that includes multiple absorption steps. The primary objective of this thesis is to address chemical losses resulting from unwanted precipitation reactions within the system using process simulation. Objective 1 entails developing a process simulation tool capable of accurately predicting precipitates and facilitating improved process design choices. Absorption systems are commonly designed following absorption efficiencies. The developed tool allows us to expand the understanding of the complex system and to overview conditions that promote precipitation reactions, thus including this knowledge on top of absorption efficiency when making design choices.

Soot formation during combustion

Expanding our scope beyond the chemical recovery, we encounter another potential to minimize overall chemical usage. And this potential lies in reducing bleaching chemicals during the bleaching of pulp. The necessity for bleaching agents can, in part, be attributed to the chemical recovery process, specifically to the combustion of red liquor. Soot formed during combustion is carried throughout the entire chemical recovery process, ultimately ending up in the white liquor and causing coloration to the pulp during pulping. This increases the demand for bleaching chemicals. Soot are carbonaceous particles that form during the incomplete combustion or pyrolysis of hydrocarbons (Michelsen et al. 2020). Figure 3 schematically shows the complex process of soot formation.

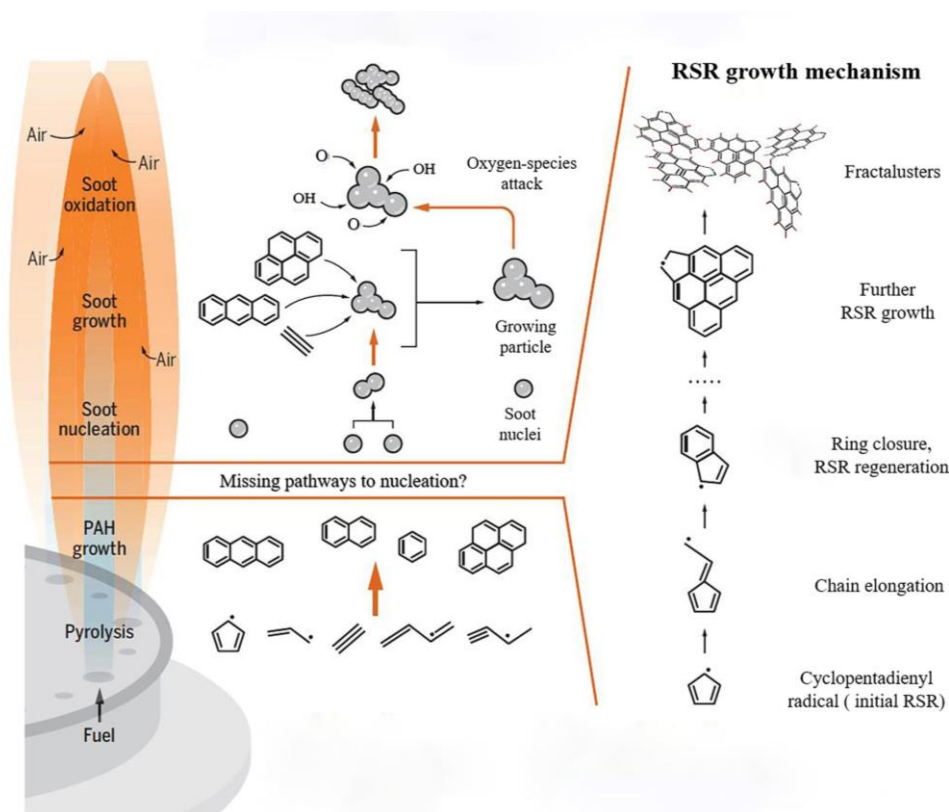


Figure 3: Schematic diagram of the physical and chemical steps in soot formation (Chu et al. 2023)

Soot formation occurs in several steps. Initially, hydrocarbons break down by losing hydrogen atoms, leading to radical sites forming. In the second step, smaller aromatic rings are formed, which grow into larger ring structures called polycyclic aromatic hydrocarbons (PAH). These larger structures form soot particles through coagulation, surface growth, and internal structural change (Chu et al. 2023; Baumbach et al. 2016). To avoid soot, the complete combustion of red liquor must be ensured. Besides fuel type, pressure, time, and temperature, the fuel-to-air ratio (equivalence ratio) is recognized as a significant parameter influencing soot formation (Gleason et al. 2022; Mansurov 2005). Optimized fuel dispersion leads to an optimized mixing of fuel and oxygen, enhancing combustion. Red liquor spraying is recognized as a parameter that can be fine-tuned by simply replacing the nozzles, thus eliminating the need for redesigning the combustion vessel while significantly impacting combustion efficiency. The second objective aims to identify optimized red liquor spraying to enhance combustion efficiency.

Combustion processes involve the complex interaction of fuel, oxidizer, and combustion products within a confined space—the combustion vessel. A spatially resolved understanding of how fluid dynamics, heat transfer, and chemical kinetics operate inside the combustion vessel is crucial to derive improvements in the combustion system. Computational fluid dynamics

can provide such an understanding. Objective 2 of this thesis focuses on simulating the combustion vessel using computational fluid dynamics (CFD). Through the development of the simulation, a tool for conducting virtual experiments is established, which allows for analyzing the effects of spraying characteristics on the combustion of red liquor.

3 Applied Approaches

This chapter summarizes the applied approaches to target the thesis' objectives.

3.1 Objective 1: Process Simulation to Target Precipitations

Figure 4 shows graphically the applied approaches that lead to fulfilling objective 1.

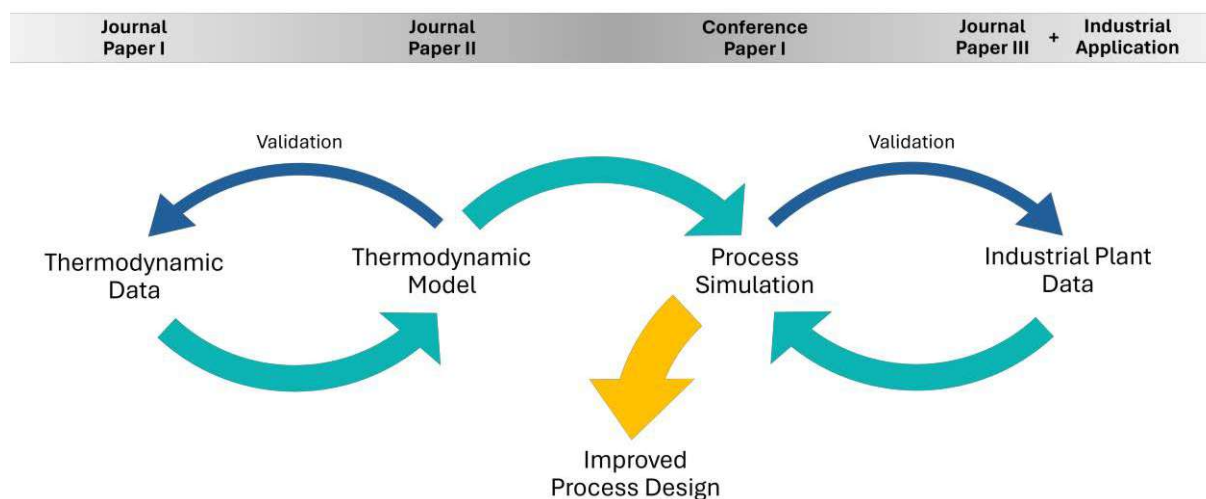


Figure 4: Applied approaches to target objective 1 and associated publications

In process modeling, an accurate description of the chemical system is essential. The initial step involved understanding the present chemical system and selecting available thermodynamic data to describe it. Based on this foundation, a thermodynamic model was developed to describe all dependencies adequately. The validated model was then integrated into a process simulation, utilizing data from an actual industrial plant for assessment. Once the process model was rigorously evaluated, virtual experiments were conducted to derive optimized process conditions. This systematic approach ensures a precise representation of the chemical system and facilitates the exploration and refinement of optimal operational parameters in a simulated environment.

The following takes you through the performed steps in detail and refers you to the corresponding publications.

Review of thermodynamic data

The chemical system present in the absorption system is a complex electrolyte system. Figure 5 summarizes the present compounds.

electrolyte NRTL model is widely used to model electrolyte systems. It incorporates short-range interactions as well as long-range electrostatic interactions between ions to describe the activity coefficients. The electrolyte NRTL model was applied as proposed by Chen and Evans and extended by Mock et al. (Chen and Evans 1986; Mock et al. 1986). The vapor phase properties were calculated using the Redlich-Kwong equation of state (Redlich and Kwong 1949). A detailed description of the model is provided in **Journal Paper II**. The model is embedded in Aspen Plus, which is why Aspen Plus V10 was chosen as the modeling software. After selecting the thermodynamic method, all dissociation and precipitation reactions were implemented into the model. Table 1 shows all implemented reactions.

Table 1: Implemented electrolyte reactions

Reaction	Type
$2 \text{H}_2\text{O} \leftrightarrow \text{OH}^- + \text{H}_3\text{O}^+$	Partial dissociation equilibrium
$2 \text{H}_2\text{O} + \text{SO}_2 \leftrightarrow \text{H}_3\text{O}^+ + \text{HSO}_3^-$	Partial dissociation equilibrium
$\text{H}_2\text{O} + \text{HSO}_3^- \leftrightarrow \text{H}_3\text{O}^+ + \text{SO}_3^{2-}$	Partial dissociation equilibrium
$\text{H}_2\text{SO}_4 + \text{H}_2\text{O} \leftrightarrow \text{H}_3\text{O}^+ + \text{HSO}_4^-$	Partial dissociation equilibrium
$\text{H}_2\text{O} + \text{HSO}_4^- \leftrightarrow \text{H}_3\text{O}^+ + \text{SO}_4^{2-}$	Partial dissociation equilibrium
$\text{MgOH}^+ \leftrightarrow \text{OH}^- + \text{Mg}^{2+}$	Partial dissociation equilibrium
$\text{CaOH}^+ \leftrightarrow \text{OH}^- + \text{Ca}^{2+}$	Partial dissociation equilibrium
$2 \text{H}_2\text{O} + \text{CO}_2 \leftrightarrow \text{H}_3\text{O}^+ + \text{HCO}_3^-$	Partial dissociation equilibrium
$\text{H}_2\text{O} + \text{HCO}_3^- \leftrightarrow \text{H}_3\text{O}^+ + \text{CO}_3^{2-}$	Partial dissociation equilibrium
$\text{Mg}(\text{OH})_2 \rightarrow \text{OH}^- + \text{MgOH}^+$	Complete dissociation
$\text{Ca}(\text{OH})_2 \rightarrow \text{OH}^- + \text{CaOH}^+$	Complete dissociation
$\text{MgSO}_4 \rightarrow \text{Mg}^{2+} + \text{SO}_4^{2-}$	Complete dissociation
$\text{MgSO}_3 \rightarrow \text{Mg}^{2+} + \text{SO}_3^{2-}$	Complete dissociation
$\text{CaSO}_4 \rightarrow \text{Ca}^{2+} + \text{SO}_4^{2-}$	Complete dissociation
$\text{CaSO}_3 \rightarrow \text{Ca}^{2+} + \text{SO}_3^{2-}$	Complete dissociation
$\text{MgCO}_3 \rightarrow \text{Mg}^{2+} + \text{CO}_3^{2-}$	Complete dissociation
$\text{CaCO}_3 \rightarrow \text{Ca}^{2+} + \text{CO}_3^{2-}$	Complete dissociation
$\text{Mg}(\text{OH})_2 (\text{s}) \leftrightarrow \text{OH}^- + \text{MgOH}^+$	Salt precipitation equilibrium
$\text{Ca}(\text{OH})_2 (\text{s}) \leftrightarrow \text{OH}^- + \text{CaOH}^+$	Salt precipitation equilibrium
$\text{MgSO}_3 * 6 \text{H}_2\text{O} (\text{solid}) \leftrightarrow \text{Mg}^{2+} + \text{SO}_3^{2-} + 6 \text{H}_2\text{O} (\text{aqueous})$	Salt precipitation equilibrium
$\text{MgSO}_3 * 3 \text{H}_2\text{O} (\text{solid}) \leftrightarrow \text{Mg}^{2+} + \text{SO}_3^{2-} + 3 \text{H}_2\text{O} (\text{aqueous})$	Salt precipitation equilibrium
$\text{CaSO}_3 * \frac{1}{2} \text{H}_2\text{O} (\text{solid}) \leftrightarrow \text{Ca}^{2+} + \text{SO}_3^{2-} + \frac{1}{2} \text{H}_2\text{O} (\text{aqueous})$	Salt precipitation equilibrium
$\text{MgSO}_4 * \text{H}_2\text{O} (\text{solid}) \leftrightarrow \text{Mg}^{2+} + \text{SO}_4^{2-} + 1 \text{H}_2\text{O} (\text{aqueous})$	Salt precipitation equilibrium
$\text{MgSO}_4 * 7 \text{H}_2\text{O} (\text{solid}) \leftrightarrow \text{Mg}^{2+} + \text{SO}_4^{2-} + 7 \text{H}_2\text{O} (\text{aqueous})$	Salt precipitation equilibrium
$\text{CaSO}_4 * 2 \text{H}_2\text{O} (\text{solid}) \leftrightarrow \text{Ca}^{2+} + \text{SO}_4^{2-} + 2 \text{H}_2\text{O} (\text{aqueous})$	Salt precipitation equilibrium
$\text{CaSO}_4 (\text{solid}) \leftrightarrow \text{Ca}^{2+} + \text{SO}_4^{2-} (\text{aqueous})$	Salt precipitation equilibrium

Journal paper II evaluates the applicability of the electrolyte NRTL method to model the SO_2 absorption and the solubility of all potential salts in the system.

Modeling the chemical recovery

With the validated thermodynamic model, it is possible to calculate process flowsheets. Before a generic flowsheet was built, an industrial plant served as an illustrative process example. Due to confidentiality, the details of the complete process model are not presented in this work. **Journal Paper III** presents exemplarily one absorption unit of the industrial example process. The following briefly describes the procedures performed to achieve a validated process model describing the full chemical recovery.

A comprehensive flowsheet depicting this industrial example plant was developed. Figure 6 shows the flowsheet in the simulation environment Aspen Plus.

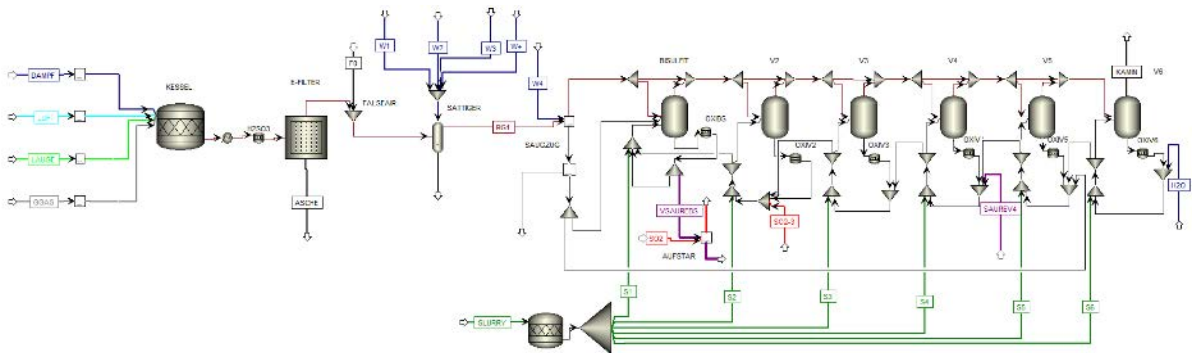


Figure 6: Constructed flowsheet of the industrial example process

The flowsheet covers the process steps of red liquor combustion, cooling of the exhaust gas, an electrostatic precipitator, a flue gas saturator, MgO hydration, absorption units, and finally, the white liquor preparation. The constructed flowsheet was fed and evaluated using real-world industrial plant data.

Initially, crucial measurement points were identified and precisely located. Daily measurements covering all characterizing parameters were collected spanning a duration of one year, resulting in a robust dataset. This dataset was subjected to data processing procedures. In the first phase, an analysis of the plotted data over time was conducted to identify intervals representing stable plant conditions indicative of standard operational scenarios. In the subsequent phase, data outliers within these identified stable time windows were identified and systematically excluded. A data point was defined as an outlier if its value exceeded five times the median absolute deviation (MAD) from the median:

$$5 * MAD = 5 * \frac{1}{n} \sum_{i=1}^n |x_i - \tilde{x}| \quad (4)$$

Where \tilde{x} is the median, x_i the measured value and n the number of measurement points. To confirm their status as outliers, the data plots over time were analyzed. By adhering to this

meticulous data processing approach, the resultant dataset was refined, ensuring its reliability and suitability for subsequent modeling analyses.

The combustion unit performs stoichiometric calculations, including the reactions given in Table 2.

Table 2: Implemented combustion reactions

Reaction	Reaction product type
$C + O_2 \rightarrow CO_2$	Gas phase
$N_2 + O_2 \rightarrow 2 NO$	Gas phase
$S + O_2 \rightarrow SO_2$	Gas phase
$2 H_2 + O_2 \rightarrow 2 H_2O$	Gas phase
$Cl_2 + H_2 \rightarrow 2 HCl$	Gas phase
$Mg + S + 2 O_2 \rightarrow MgSO_4$	Solid ash
$Ca + S + 2 O_2 \rightarrow CaSO_4$	Solid ash
$2 Mg + O_2 \rightarrow 2 MgO$	Solid ash
$2 Ca + O_2 \rightarrow 2 CaO$	Solid ash

The electrostatic precipitator is modeled to remove solid ash from the flue gas with defined efficiency. The saturator, modeled as a flash unit, calculates chemical and phase equilibrium and includes the hydration of residual MgO and CaO post-electrostatic precipitation. The hydration of MgO for slurry preparation is modeled using a stoichiometric reactor. The absorption units, modeled as flash units, calculate chemical and phase equilibrium. In industrial absorption venturi systems, the physical solubility of SO_2 is recognized as the limiting factor preventing the system from achieving equilibrium (Marocco 2010). A gas bypass was implemented to adjust venturi efficiency and align the equilibrium model with the actual process. A comprehensive description of the simulation of absorption unit 3 is provided in **Journal Paper III**. The process simulation of the entire chemical recovery system revealed that absorption unit 3 is most prone to precipitation, which is why this unit was selected as an exemplary absorption unit for publication.

The flowsheet was calibrated over the gas bypass to fit the industrial plant data of the combined $SO_3^{2-} + HSO_3^-$ in the liquid phase after white liquor preparation and after each absorption step. The combined $SO_3^{2-} + HSO_3^-$ in the liquid phase serves as a prevalent parameter within the pulp industry, commonly referred to as "total SO_2 ". This parameter is assessed daily in a laboratory following the extraction of a sample from the operational plant's absorption bottoms. Figure 7 shows the calculated and the measured combined $SO_3^{2-} + HSO_3^-$ in the liquid phase.

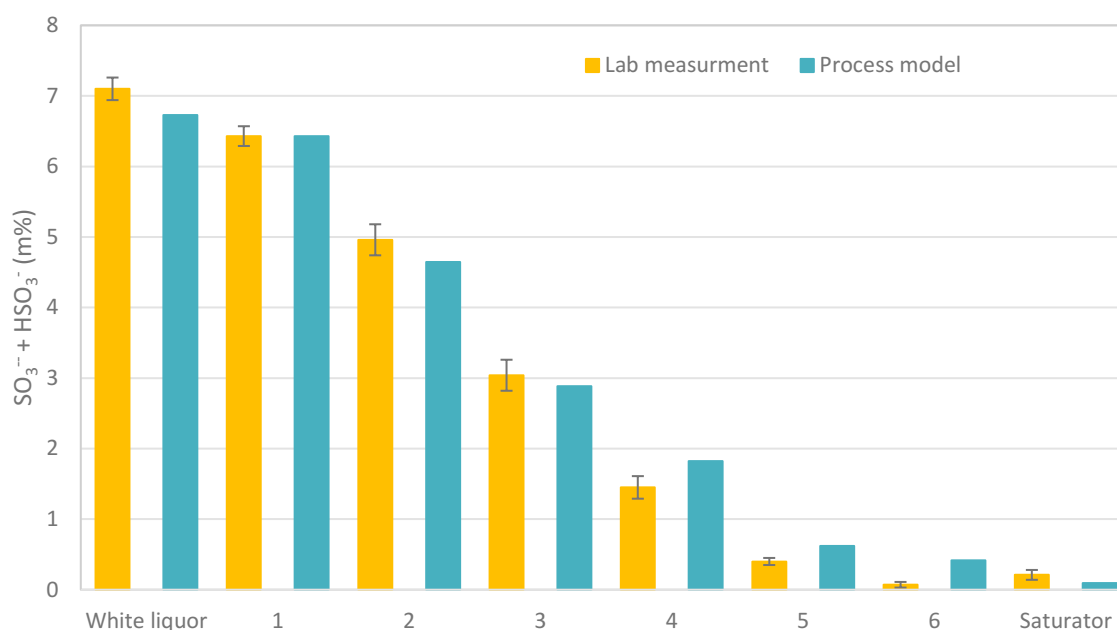


Figure 7: Combined $\text{SO}_3^{2-} + \text{HSO}_3^-$ in the liquid phase after white liquor preparation, after absorption units 1 to 6, and after the saturator; measured values with standard deviation

The absorption process occurs in a counterflow configuration. In absorption unit 6, a significant portion of the liquid consists of $\text{Mg}(\text{OH})_2$. The white liquor consists of $\text{Mg}(\text{HSO}_3)_2$. $\text{Mg}(\text{HSO}_3)_2$ exists in a dissociated state within the liquid phase, presenting as Mg^{++} , SO_3^{2-} , HSO_3^- and H_3O^+ (refer to Table 1 for the detailed electrolyte reactions). Following equations (2) and (3) in section 2, an increase in the absorption of SO_2 leads to a corresponding increase in $\text{SO}_3^{2-} + \text{HSO}_3^-$ within the liquid phase. The model and measurements confirm this trend of rising $\text{SO}_3^{2-} + \text{HSO}_3^-$ as we progress through the absorption units.

Finally, the flowsheet was evaluated using the following parameters:

1. CO_2 , O_2 , and SO_2 in the gas phase before the saturator
2. SO_2 in the exhaust gas after the last absorption step

Table 3 summarizes the calculated and measured CO_2 , O_2 , and SO_2 in the gas phase before the saturator.

Table 3: CO_2 , O_2 and SO_2 in the gas phase before the saturator in vol% N, dry

	Measurement with relative error	Calculation
CO_2	13.31 (relative error: 0.9 %)	13.42
O_2	5.42 (relative error: 3.3 %)	5.89
SO_2	1.13 (relative error: 2.3 %)	1.136

Figure 8 shows the SO_2 in the exhaust gas after the last absorption step.

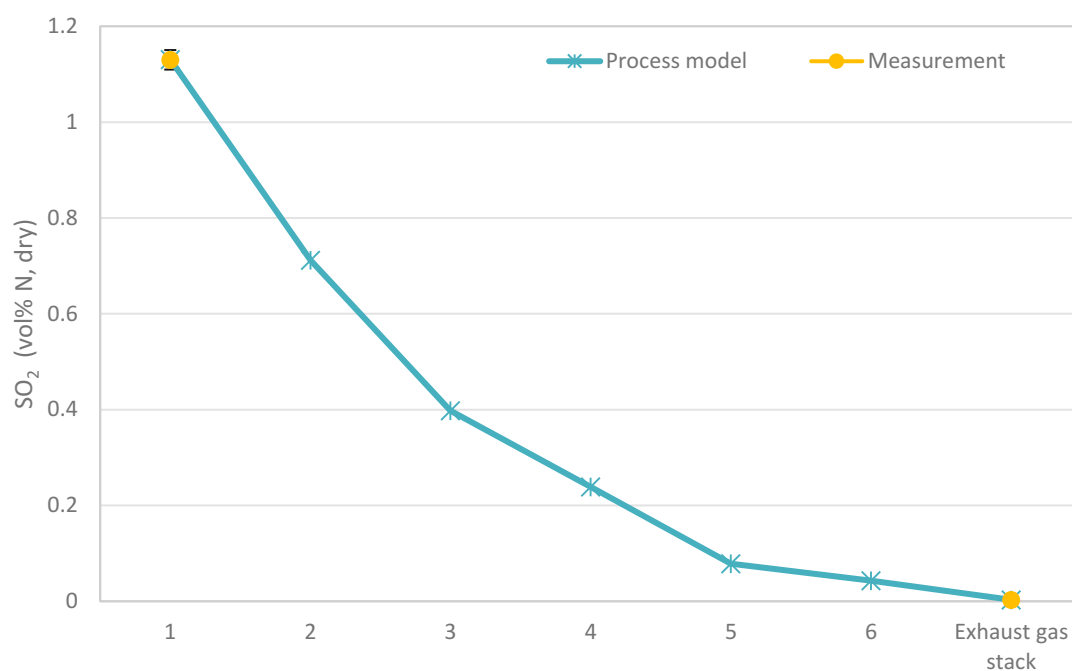


Figure 8: SO_2 in the gas before absorption units 1 to 6 and after absorption unit 6

The SO_2 content is measured at two distinct points: prior to the absorption units and at the exhaust gas stack. The measurement is upstream of the gas saturator, where the gas undergoes saturation with water. Both Table 3 and Figure 8 represent the concentration on a dry basis, resulting in uniform values before and after saturation at the saturator. The gas phase measurements demonstrate a high level of accuracy for the model. As anticipated, the SO_2 content in the gas phase decreases with each absorption step until it is ultimately discharged through the exhaust gas stack.

With the simulation of the industrial example process, the main precipitation phenomena were analyzed, and units where precipitation occurs were identified. Sensitivity analyses were performed to gain further insight into parameters influencing precipitation, investigating the effect of temperature, pH value, and $\text{Mg}(\text{OH})_2$ -slurry to SO_2 ratio. **Journal Paper III** summarizes the results of the performed sensitivity analyses for one exemplary absorption unit. The findings correspond to those from the literature study in Journal Paper I, confirming the reliability of the process simulation.

Building a process simulation tool and finding an optimized process design

To separate the process model from the industrial example process and derive generic recommendations for absorption system design, a generic absorption flowsheet was developed.

Conference Paper I presents this generic flowsheet along with two distinct process designs.

One design focuses on rapid SO_2 absorption, while the other aims to reduce precipitation within the system. Based on indications from Journal Paper III that excess $\text{Mg}(\text{OH})_2$ leads to the precipitation of MgSO_3 hydrates, the process design aimed at minimizing precipitation followed the principle of avoiding excess $\text{Mg}(\text{OH})_2$. **Conference Paper I** quantifies the chemical savings associated with adopting the process design that minimizes precipitation.

3.2 Objective 2: CFD Simulation to Target Soot Formation

Figure 9 shows graphically the applied approaches that lead to fulfilling objective 2.

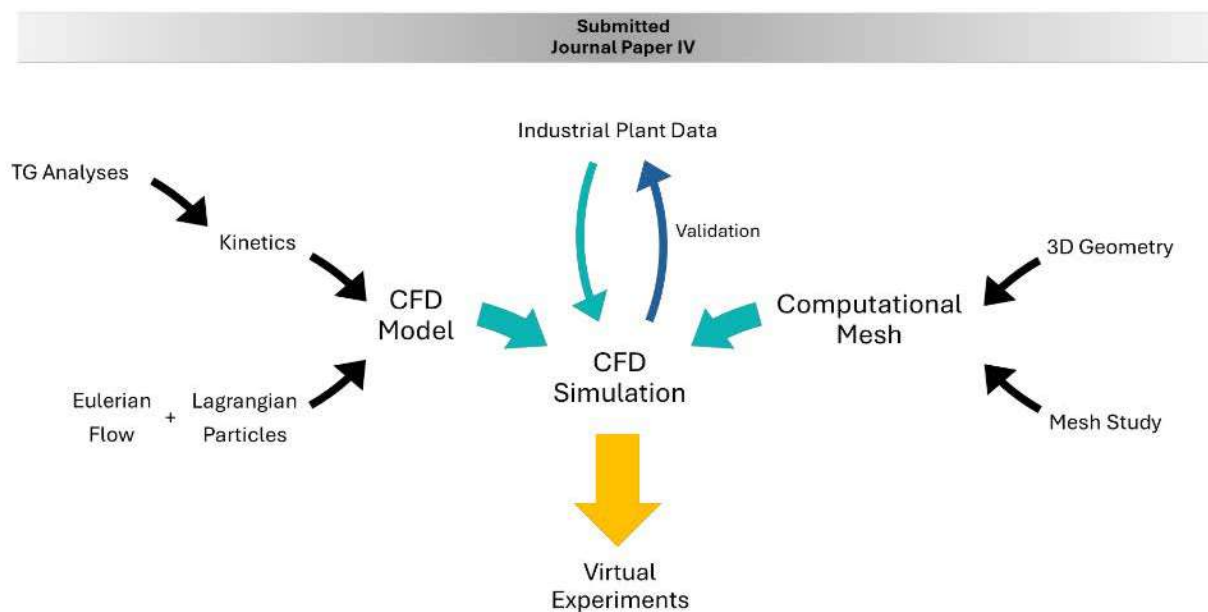


Figure 9: Applied approaches to target objective 2

A detailed spatial resolved approach is necessary to perform virtual experiments and derive the influence of different spraying characteristics on the combustion time, depicting the fluid dynamics, phase changes, and reaction kinetics. Therefore, a CFD model was developed, which describes the fuel spraying into the combustion vessel, the flow through the furnace, and the combustion inside the furnace. The developed CFD simulations were fed and evaluated using real-world industrial plant data from the same industrial example plant as for objective 1. Once evaluated, virtual experiments were performed to investigate the influence of spray angle, spray type, and particle size on combustion time. The results are submitted to be published in **Journal Paper IV**. The following takes you through the performed steps and refers you to the submitted paper for more details.

Development of the CFD Model

The CFD model was developed using the open-source simulation environment OpenFOAM® and employs an Eulerian-Lagrangian approach. The red liquor droplets, which are sprayed into the furnace, were treated as discrete particles, and the particle surrounding gas phase was modeled as a continuous phase. Figure 10 visualizes the concept of the applied Eulerian-Lagrangian approach with the employed two-way coupling.

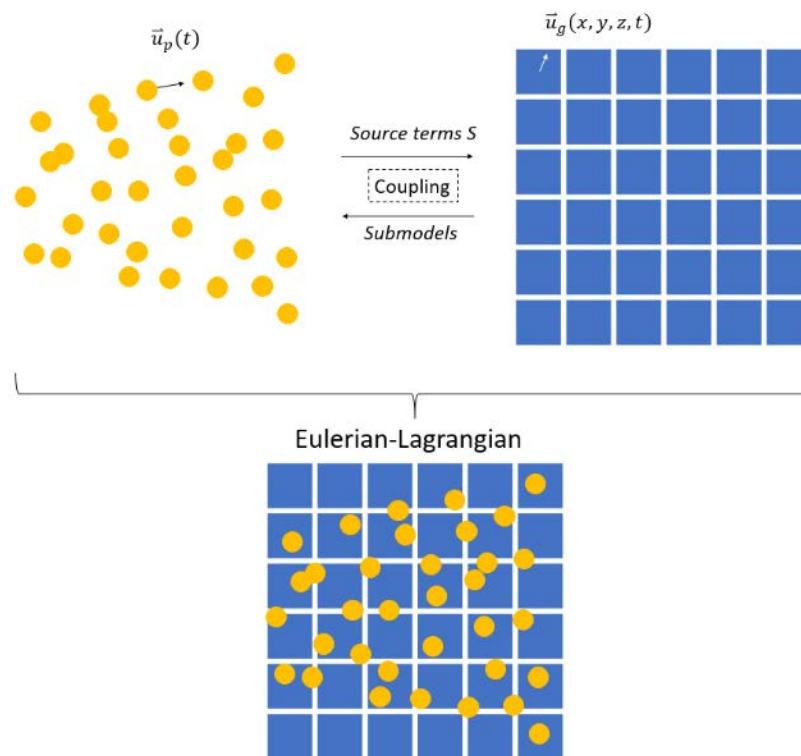


Figure 10: Top left: Lagrangian particles; Top right: Eulerian flow; Bottom: Eulerian-Lagrangian approach

While the description of Lagrangian particles can be computationally intensive, the benefit of this method lies in its ability to track specific properties of individual particles. The chosen approach, therefore, allows for tracking features such as the combustion time of red liquor droplets. The modeling approach with its underlying equations is thoroughly explained in **Journal Paper IV**.

Implementation of Phase Change and Combustion Reactions

The CFD model incorporates phase change phenomena and reaction kinetics to model the combustion process of red liquor. Red liquor combustion involves a complex system of reactions in which organic matter is oxidized and inorganic matter is recovered in the ash. However, the combustion process can be divided into four phases: Drying, devolatilization, volatile combustion, and char combustion (Pratima Bajpai 2017). Those phases were implemented into the CFD model. Figure 11 provides an overview of the simplified reaction system integrated into the CFD model.

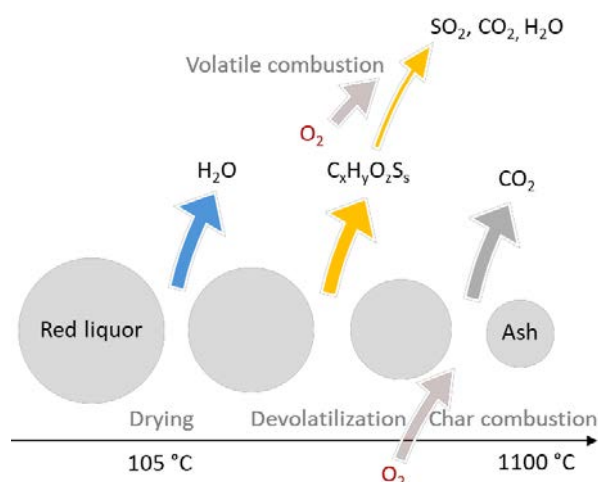


Figure 11: Visualization of implemented combustion steps

Drying was modeled following the Spalding evaporation model (Spalding 1953). The volatile components were represented as pseudo-species $C_xH_yO_zS_s$, which combusts in a gas phase combustion reaction. The stoichiometry of the gas phase reaction was derived from the known elemental composition of red liquor. The gas phase combustion was modeled using the non-kinetic Eddy Dissipation Diffusion Model (Magnussen and Hjertager 1977). The devolatilization and char combustion were modeled following an Arrhenius kinetic approach. Due to lack of available kinetic data on the combustion of red liquor, kinetic data were obtained by fitting data to results from non-isothermal thermogravimetric analyses (TGA). **Journal Paper IV** presents the results of the performed TGA and the kinetic data fitting and summarizes the applied phase changes and reaction models in detail.

Constructing a computational mesh

To depict the industrial combustion vessel, a 3D Geometry was built based on technical drawings from the industrial example plant. Figure 12 shows the 3D Geometry of the industrial combustion vessel.

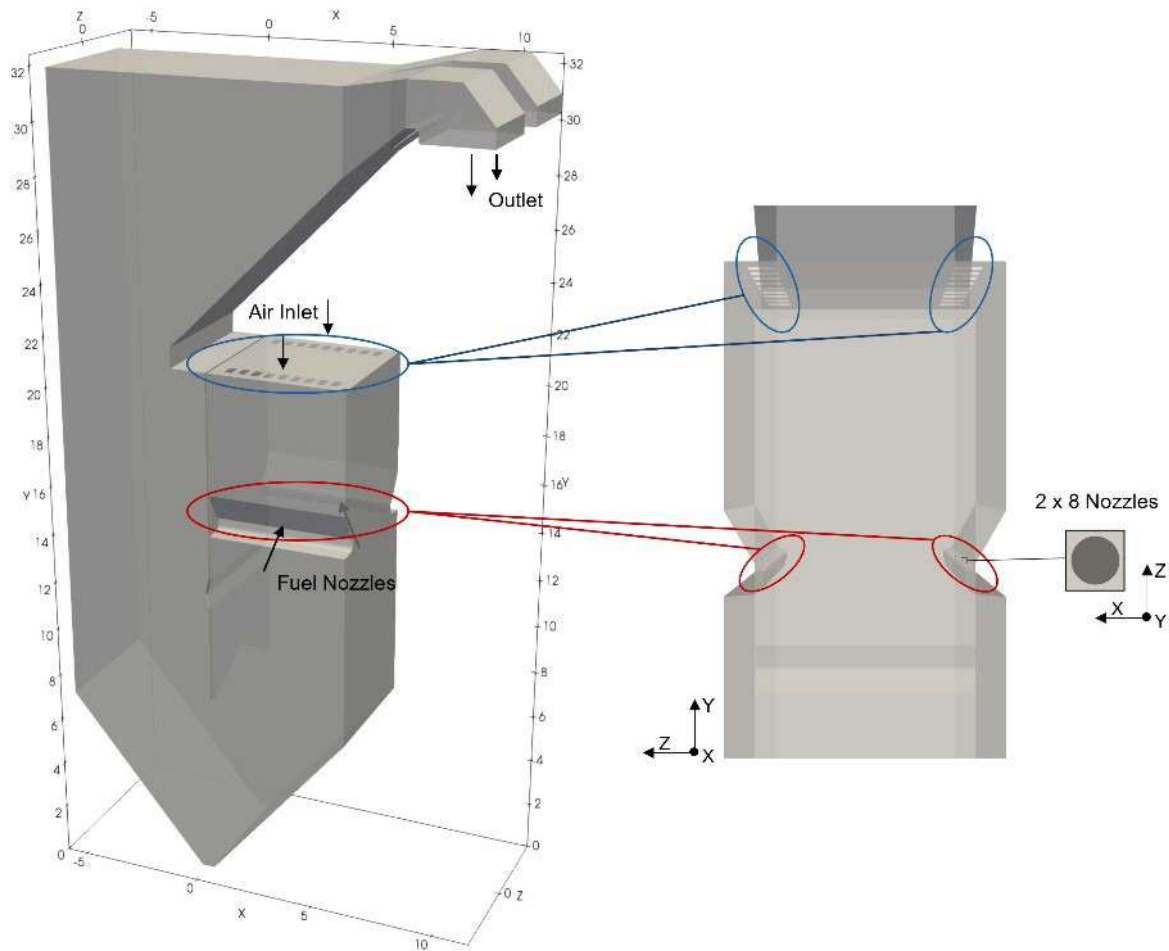


Figure 12: Left: 3D Geometry of the industrial combustion vessel (dimensional grid in m); Right: Close-up of combustion zone with air and fuel inlets

The combustion air enters from the top. Red liquor is sprayed into the combustion vessel through 16 two-phase nozzles. The combustion zone is lined with refractory material, simulated as adiabatic walls. As the combustion gas travels towards the outlet, it heats steam through tube bundle heat exchangers, which were modeled as anisotropic porous zones with a heat sink. The 3D geometry was discretized into a predominantly hexahedral mesh. When creating a computational mesh, the goal is to determine a cell size that is fine enough to depict the flow accurately while maintaining reasonable computational times. To achieve this, a mesh study was conducted, comparing the calculated velocity along the centerline of the fuel spraying for different mesh sizes with values from the literature. The geometry, the final mesh, and the performed mesh study are detailed in **Journal Paper IV**.

Performing virtual experiments

After the development of the CFD simulation, the simulation was fed with data from the industrial example plant. The data underwent the same processing as the data used for objective 1 (see 3.1). The reliability of the simulation was evaluated by comparing the results to

data from the industrial reference plant and literature expectations and by analyzing the simulation results of the Eulerian field and the Lagrangian particles for their physical accuracy. The evaluation concluded that the developed simulation model is a reliable tool to conduct comparative parameter studies. The evaluation and simulation results are detailed in **Journal Paper IV**. Finally, virtual experiments were performed on the developed CFD simulation tool to analyze the effect of three spraying characteristics (characteristic particle size, spraying angle, and spray type) on the mean particle combustion time. Table 4 summarizes the performed virtual experiments.

Table 4: Performed virtual experiments

Factor	Characteristic particle size	Spraying angle	Spray type
Experiment#1	2 mm	15 °	Hollow Cone
Experiment#2	2 mm	30 °	Hollow Cone
Experiment#3	3 mm	15 °	Hollow Cone
Experiment#4	3 mm	30 °	Hollow Cone
Experiment#5	2 mm	15 °	Full Cone
Experiment#6	2 mm	30 °	Full Cone
Experiment#7	3 mm	15 °	Full Cone
Experiment#8	3 mm	30 °	Full Cone

Journal Paper IV summarizes the virtual experiments, concluding with recommendations on designing fuel spraying to optimize the combustion.

4 Results – Summary of Publications

This chapter summarizes the research papers that constitute this thesis. My contribution to each publication is stated in the *List of Appended Publications* at the beginning of this thesis. The full papers are found in the chapter *Publications*.

4.1 Objective 1: Process Simulation to Target Precipitations

Journal Paper I is a comprehensive literature review paper on available solubility data of potential precipitations in the MgO-CaO-SO₂-H₂O system, the chemical system present in the absorption of the chemical recovery. The reviewed data serve as a reliable basis for process modeling of this system. The study identifies MgSO₃, MgSO₄, Mg(OH)₂, CaSO₃, CaSO₄, and Ca(OH)₂ as potential salts and analyzes their solubility behavior under various conditions. The stability of the salts depends on the state of the salts and on influencing factors such as pH value, SO₂ content, and the co-existence of other salts. Those factors are also investigated in the review study.

Literature data evaluated by the International Union of Pure and Applied Chemistry (IUPAC) are revisited, and additional and newer studies are supplemented to obtain a solid base of accurate experimental values. For a temperature range from 0 to 100 °C, the reviewed investigations and data provide a solid base to map precipitation issues accurately.

Journal Paper II assesses the thermodynamic modeling of the MgO-CaO-CO₂-SO₂-H₂O-O₂ system using the electrolyte NRTL activity coefficient model, primarily focusing on the solubility of potential salts in the system. The study investigates the solubility of SO₂ in water and its absorption equilibrium with Mg(OH)₂ as well as the precipitation of Mg(OH)₂, Ca(OH)₂, MgSO₃, CaSO₃, MgSO₄, CaSO₄, and their hydrate forms. The calculated equilibria and solubilities are evaluated using experimental literature data reviewed in Journal Paper I. The deviation from the experimental data is calculated and plotted for each calculation to visualize the model's performance. The study concludes the model's applicability to describe chemically stable systems and to predict precipitations during absorption processes. However, limitations of the model are recognized, such as capturing dynamic hydrate transition behavior in rapidly changing and unstable systems. Furthermore, the study highlights the scarcity of experimental data regarding SO₂ absorption in Mg(OH)₂ solutions, limiting the evaluation of thermodynamic models based on such data.

Journal Paper III applies the thermodynamic model evaluated in Journal Paper II and presents a process model featuring a single absorption unit. The process model is fed and validated using industrial plant data. It accurately depicts the pH value and the combined HSO₃⁻ and SO₃²⁻ content in the liquid phase after absorption. Sensitivity analyses are conducted to iden-

tify key parameters influencing unwanted precipitation reactions in the system, including temperature, pH value, and the Slurry/SO₂ ratio. The study identifies parameter limits at which increased precipitations occur. The process model simulates one absorption unit from an industrial plant and is tailored to that specific facility. Consequently, the extrapolation of results to a generic absorption process has limited validity. The study highlights the importance of not only considering removal efficiency but also potential solid precipitation when designing an SO₂ absorption process.

Conference Paper I presents two process designs for a multistep SO₂ absorption process utilizing an Mg(OH)₂ slurry representing a generic absorption process in the magnesium bisulfite-based pulp industry. The first design focuses on maximizing SO₂ absorption efficiency with the fewest steps needed to reach a target SO₂ content in the exhaust gas. In contrast, the second design aims to achieve the target SO₂ content while minimizing chemical loss due to precipitation in the system. The results indicate that the first design achieves the target SO₂ limit after four absorption steps but suffers from significant precipitation loss, accounting for almost 20 % of the product output by weight. The second design requires eight absorption steps to meet the target SO₂ limit, but it effectively reduces precipitation loss to only 5 % of the product output by weight. The process design that minimizes precipitation results in a fivefold reduction in SO₂ demand and a 20 % decrease in slurry demand compared to the design focused solely on maximizing absorption.

4.2 Objective 2: CFD Simulation to Target Soot Formation

The submitted **Journal Paper IV** presents virtual experiments using computational fluid dynamics simulations to investigate the impact of various spraying parameters on the combustion time of red liquor droplets within a combustion vessel. The simulations integrate computational fluid dynamics with kinetic modeling. Performed thermogravimetric analyses (TGA) of red liquor provide insights into combustion behavior and provide the basis for kinetic model fitting. One-step reaction kinetics are incorporated into the model. The virtual experiments include parameters such as spray angle, droplet size, and spray type. Through these experiments, recommendations on optimizing red liquor spraying for faster combustion are derived. The virtual experiments revealed that the fastest combustion is achieved with a 2 mm droplet size and a 30° spraying angle, using the hollow cone spray type, as these spray characteristics enhance fuel dispersion in the combustion vessel. The developed CFD model is presented as a tool for further investigations beyond the scope of the performed virtual experiments.

5 Conclusion and Outlook

This thesis aimed to derive process optimization strategies to minimize the necessity for adding fresh chemicals to the magnesium bisulfite pulping process through process and computational fluid dynamic simulations. Two main sources for the need to add chemicals were identified and targeted: precipitation in the absorption system causing chemical loss and soot formation during red liquor combustion, leading to an increased demand for bleaching agents in the pulp production line.

To tackle precipitation in the absorption system, a mechanistic process simulation tool for the chemical recovery was developed. For that purpose, comprehensive literature reviews, thermodynamic modeling, and flowsheet calculations were integrated. The literature review of solubility data for potential salts in the $\text{MgO-CaO-CO}_2\text{-SO}_2\text{-H}_2\text{O-O}_2$ establishes a reliable basis for process modeling. The assessment of the electrolyte NRTL activity coefficient model to depict the complex electrolyte system concludes that the model effectively describes chemically stable systems and predicts precipitations. The model assumes thermodynamic equilibrium. This entails that the model is limited to describing chemically stable systems and does not capture dynamic hydrate transitions. Furthermore, it was recognized that experimental data on the absorption capacity of SO_2 in Mg(OH)_2 are scarce. To overcome this, it is recommended that future studies investigate the absorption capacity experimentally. A setup to determine the absorption capacity experimentally was prepared as presented in Figure 13, which can be used for further studies on this topic.

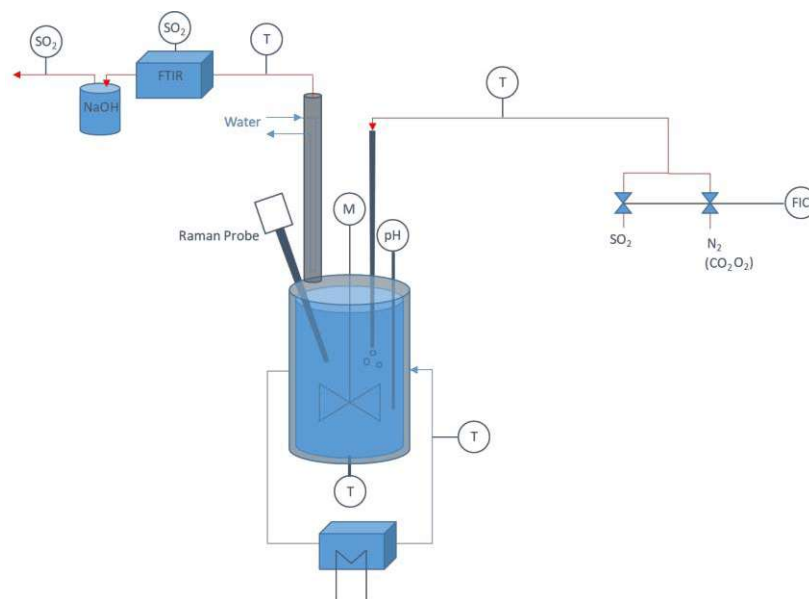


Figure 13: Prepared setup to determine the SO_2 absorption capacity of Mg(OH)_2

The setup requires improving the sensitivity of the measurement of SO_2 in the gas phase, which remains a topic for future research possibilities.

Finally, an industrial-scale process model of the chemical recovery was developed using the validated thermodynamic model. A real industrial example process was used as a reference process. Since the model's applicability to derive generic recommendations for $\text{Mg}(\text{OH})_2\text{-SO}_2$ absorption processes is limited due to its specific tailoring to a particular industrial setup, a more generic process flowsheet model was developed. This model was used to explore different process designs for multistep SO_2 absorption using an $\text{Mg}(\text{OH})_2$ slurry. The first design follows the conventional maxime to maximize SO_2 absorption efficiency, resulting in significant chemical loss due to precipitation. The second design focuses on minimizing precipitation. The proposed process design to minimize precipitation requires more absorption steps but significantly reduces both SO_2 and slurry demand. Focusing solely on chemical usage, this study suggests that the design aiming for minimized precipitation is advantageous over the conventional design aimed at fast absorption. To comprehensively evaluate the environmental impact of both designs, a cradle-to-grave life cycle assessment for both process designs is recommended.

The developed model has proven to be an invaluable tool for calculating and comparing different process designs and their impact on chemical loss and demand. Beyond the investigations performed, the model can be used to conduct parameter studies, find operational limits, and enhance the overall understanding of the process system. With this tool, industries can respond to operational problems with a comprehensive understanding of the mechanistic interplay within the process system. For future development, the process model can also serve as the foundation for creating digital twins of industrial absorption systems. A digital twin is a virtual replica of a physical system used for real-time monitoring, diagnostics, and predictive maintenance. By integrating the model with real-time data from the actual system, industries can achieve better control and oversight, anticipate issues before they occur, and optimize performance on the fly. Furthermore, the process model can be an effective teaching tool for both operating and development engineers, helping them understand the process beyond the operational flows. This educational application ensures that staff are well-versed in both the theoretical and practical aspects of the system, promoting more effective and informed operation. Such a teaching tool becomes increasingly valuable with higher staff fluctuation.

To tackle soot formation during red liquor combustion, a 3D resolved CFD simulation tool of an industrial sized combustion vessel was developed. The combustion behavior was implemented as a simplified reaction system, including drying, devolatilization, combustion of volatiles, and char combustion. The devolatilization as well as char combustion kinetics were derived by parameter fitting to non-isothermal TGA results. The developed simulation setup was used to perform virtual experiments varying spraying characteristics such as characteristic droplet size, spray angle, and spray type and to analyze their effect on the average particle

combustion time. Based on the performed calculation, it was derived that a reduction in particle size, a wider spray angle, and hollow cone over full cone spraying are advantageous for the combustion speed. To enhance the developed CFD simulation tool, future studies can focus on increasing the level of detail in modeling the reaction system. Refining the reaction system can include the implementation of char gasification with H_2O and CO_2 , resolving the volatiles into heavy and light volatiles as well as resolving the gas combustion reaction system. The refinement of the combustion model will necessitate mesh refinement, increasing computational complexity. Implementing a dynamic mesh that refines in reaction zones is a potential approach to managing computational demands. Literature reports that red liquor droplets swell significantly during devolatilization, a phenomenon also observed during the performed TGA experiments. The implementation of particle swelling and, with it, addressing the heat transfer within particles can further improve the model's accuracy while also adding complexity and increasing computational effort.

The developed CFD model serves as a tool that extends beyond the performed analyses of fuel spraying characteristics and their influence on combustion speed. The simulation of the combustion vessel allows for studying temperature zoning, oxygen supply, and fuel residence time in hot and cold combustion zones, providing detailed insights into the complex combustion system that are difficult to measure without extensive and expensive experimental setups. The CFD tool enables industries to test and evaluate various design modifications and retrofitting options for existing combustion vessels to improve combustion efficiency and reduce emissions. Such studies can include analyzing the effect of air staging and determining the optimal location of fuel nozzles. It also allows studying the effect of changing input conditions, including air inlet temperature and fuel-air ratio. Furthermore, the model can investigate fuel adaptation scenarios, such as changes in water content and the effects of additives. It is important to note that altering fuel composition can impact reaction kinetics, requiring adjustments to the model's kinetic parameters. The applied approaches in developing the CFD model are applicable to various combustion scenarios. By updating the kinetic input data, the model can be adapted to simulate the combustion of any liquid or solid particle fuel, making it a valuable tool for optimizing and controlling combustion processes across a wide range of industries.

Bibliography

Publication bibliography

Bashmakov, I. A.; L.J. Nilsson; A. Acquaye; C. Bataille; J.M. Cullen; S. de la Rue du Can et al. (2022): Industry. In P.R. Shukla, J. Skea, R. Slade, A. Al Khourdajie, R. van Diemen, D. McCollum et al. (Eds.): *Climate change 2022. Mitigation of climate change : Working Group III Contribution to the Sixth Assessment Report of the Intergovernmental Panel on Climate Change*. Cambridge, UK and New York, NY, USA: Cambridge University Press, pp. 1161–1244.

Baumbach, Günter; Hartmann, Hans; Höfer, Isabel; Hofbauer, Hermann; Hülsmann, Theresa; Kaltschmitt, Martin et al. (2016): Grundlagen der thermo-chemischen Umwandlung biogener Festbrennstoffe. In Martin Kaltschmitt, Hans Hartmann, Hermann Hofbauer (Eds.): *Energie aus Biomasse. Grundlagen, Techniken und Verfahren*. 3., aktualisierte und erweiterte Auflage. Berlin, Heidelberg: Springer Vieweg, pp. 579–814. Available online at https://link.springer.com/chapter/10.1007/978-3-662-47438-9_11.

Chen, Chau-Chyun; Evans, L. B. (1986): A local composition model for the excess Gibbs energy of aqueous electrolyte systems. In *AIChE J.* 32 (3), pp. 444–454. DOI: 10.1002/aic.690320311.

Chu, Huaqiang; Qi, Jiawei; Feng, Shunjie; Dong, Wenlong; Hong, Run; Qiu, Bingbing; Han, Weiwei (2023): Soot formation in high-pressure combustion: Status and challenges. In *Fuel* 345, p. 128236. DOI: 10.1016/j.fuel.2023.128236.

Furszyfer Del Rio; Dylan D.; Sovacool, Benjamin K.; Griffiths, Steve; Bazilian, Morgan; Kim, Jinsoo et al. (2022): Decarbonizing the pulp and paper industry: A critical and systematic review of sociotechnical developments and policy options. In *Renewable and Sustainable Energy Reviews* 167, p. 112706. DOI: 10.1016/j.rser.2022.112706.

Gleason, Kevin; Carbone, Francesco; Gomez, Alessandro (2022): Effect of equivalence ratio and temperature on soot formation in partially premixed counterflow flames. In *Combustion and Flame* 242, p. 112088. DOI: 10.1016/j.combustflame.2022.112088.

Magnussen, B. F.; Hjertager, B. H. (1977): On mathematical modeling of turbulent combustion with special emphasis on soot formation and combustion. In *Symposium (International) on Combustion* 16 (1), pp. 719–729. DOI: 10.1016/S0082-0784(77)80366-4.

Mansurov, Z. A. (2005): Soot Formation in Combustion Processes (Review). In *Combust Explos Shock Waves* 41 (6), pp. 727–744. DOI: 10.1007/s10573-005-0083-2.

Marocco, L. (2010): Modeling of the fluid dynamics and SO₂ absorption in a gas–liquid reactor. In *Chemical Engineering Journal* 162 (1), pp. 217–226. DOI: 10.1016/j.cej.2010.05.033.

Michelsen, Hope A.; Colket, Meredith B.; Bengtsson, Per-Erik; D'Anna, Andrea; Desgroux, Pascale; Haynes, Brian S. et al. (2020): A Review of Terminology Used to Describe Soot Formation and Evolution under Combustion and Pyrolytic Conditions. In *ACS Nano* 14 (10), pp. 12470–12490.

Mock, Bill; Evans, L. B.; Chen, Chau-Chyun (1986): Thermodynamic representation of phase equilibria of mixed-solvent electrolyte systems. In *AIChE J.* 32 (10), pp. 1655–1664. DOI: 10.1002/aic.690321009.

Pratima Bajpai (2016): Chapter 3 - Pulp and Paper Production Processes and Energy Overview. In Pratima Bajpai (Ed.): *Pulp and Paper Industry: Energy Conservation*. Amsterdam: Elsevier, pp. 15–49. Available online at <https://www.sciencedirect.com/science/article/pii/B9780128034118000032>.

Pratima Bajpai (2017): Chapter 1 - Introduction. In Pratima Bajpai (Ed.): *Pulp and Paper Industry: Chemical Recovery*: Elsevier, pp. 1–23. Available online at <https://www.sciencedirect.com/science/article/pii/B9780128111031000012>.

Pratima Bajpai (2018): Chapter 12 - Pulping Fundamentals. In Pratima Bajpai (Ed.): *Biermann's Handbook of Pulp and Paper* (Third Edition). Third Edition: Elsevier, pp. 295–351. Available online at <https://www.sciencedirect.com/science/article/pii/B9780128142400000124>.

Redlich, O.; Kwong, J. N. S. (1949): On the thermodynamics of solutions; an equation of state; fugacities of gaseous solutions. In *Chemical Reviews* 44 (1), pp. 233–244. DOI: 10.1021/cr60137a013.

Sitter, Sophie; Chen, Qi; Grossmann, Ignacio E. (2019): An overview of process intensification methods. In *Current Opinion in Chemical Engineering* 25, pp. 87–94. DOI: 10.1016/j.coche.2018.12.006.

Spalding, D. B. (1953): The combustion of liquid fuels. In *Symposium (International) on Combustion* 4 (1), pp. 847–864. DOI: 10.1016/S0082-0784(53)80110-4.

Steindl, M.; Röder, T.; Simharl, R.; Harasek, M.; Friedl, A.; Sixta, H. (2005): Online Raman monitoring of the phase transition of magnesium sulphite hydrate. In *Chemical Engineering and Processing: Process Intensification* 44 (4), pp. 471–475. DOI: 10.1016/j.cep.2004.06.011.

Weiß, Barbara D.; Haddadi, Bahram; Harasek, Michael (2023): Assessment of Modeling the MgO-CaO-CO₂-SO₂-H₂O-O₂ System Using the Electrolyte NRTL Activity Coefficient Model. In *Ind. Eng. Chem. Res.* 62 (32), pp. 12626–12639. DOI: 10.1021/acs.iecr.3c00868.

List of Figures

Figure 1: Main steps of the pulp production line.....	5
Figure 2: Simplified flowsheet of the chemical recovery in magnesium bisulfite-based pulping process	6
Figure 3: Schematic diagram of the physical and chemical steps in soot formation (Chu et al. 2023).....	8
Figure 4: Applied approaches to target objective 1 and associated publications	10
Figure 5: Electrolyte system in the absorption system (Weiß et al. 2023)	11
Figure 6: Constructed flowsheet of the industrial example process	13
Figure 7: Combined $\text{SO}_3^{2-} + \text{HSO}_3^-$ in the liquid phase after white liquor preparation, after absorption units 1 to 6, and after the saturator; measured values with standard deviation.....	15
Figure 8: SO_2 in the gas before absorption units 1 to 6 and after absorption unit 6	16
Figure 9: Applied approaches to target objective 2.....	18
Figure 10: Top left: Lagrangian particles; Top right: Eulerian flow; Bottom: Eulerian-Lagrangian approach	19
Figure 11: Visualization of implemented combustion steps.....	20
Figure 12: Left: 3D Geometry of the industrial combustion vessel (dimensional grid in m); Right: Close-up of combustion zone with air and fuel inlets	21
Figure 13: Prepared setup to determine the SO_2 absorption capacity of $\text{Mg}(\text{OH})_2$	25

List of Tables

Table 1: Implemented electrolyte reactions	12
Table 2: Implemented combustion reactions	14
Table 3: CO ₂ , O ₂ and SO ₂ in the gas phase before the saturator in vol% N, dry	15
Table 4: Performed virtual experiments	22

Abbreviations and Symbols

Abbreviations

CFD	Computational Fluid Dynamics
FTIR	Fourier-Transform Infrared Spectroscopy
MAD	Madian Absolute Deviation
NRTL	Non-Random-Two-Liquid-Model
PAH	Polycyclic Aromatic Hydrocarbons
TGA	Thermogravimetric Analyses

Roman symbols

n	Number of measurement points
s	Standard deviation
S	Source term
\vec{u}	m/s Velocity vector
x_i	Measured value
\tilde{x}	Median

Subscripts

g	Gas
p	Particle

Publications

The following presents the journal and conference paper that contain the main research findings of this thesis. A summary of the publication is given in section 4 of the chapter *Research Summary*.

Journal Paper I

Die approbierte gedruckte Originalversion dieser Dissertation ist an der TU Wien Bibliothek verfügbar.
The approved original version of this doctoral thesis is available in print at TU Wien Bibliothek.

Review

Solubility Data of Potential Salts in the MgO-CaO-SO₂-H₂O-O₂ System for Process Modeling

Barbara D. Weiß *  and Michael Harasek 

Institute of Chemical, Environmental and Bioscience Engineering, TU Wien, Getreidemarkt 9, 1060 Vienna, Austria; michael.harasek@tuwien.ac.at

* Correspondence: barbara.weiss@tuwien.ac.at

Abstract: This review studies unwanted precipitation reactions, which can occur in SO₂ absorption processes using a magnesium hydroxide slurry. Solubility data of potential salts in the MgO-CaO-SO₂-H₂O system are evaluated. The reviewed data can serve as a reliable basis for process modeling of this system used to support the optimization of the SO₂ absorption process. This study includes the solubility data of MgSO₃, MgSO₄, Mg(OH)₂, CaSO₃, CaSO₄, and Ca(OH)₂ as potential salts. The solubility is strongly dependent on the state of the precipitated salts. Therefore, this review includes studies on the stability of different forms of the salts under different conditions. The solubility data in water over temperature serve as a base for modeling the precipitation in such system. Furthermore, influencing factors such as pH value, SO₂ content and the co-existence of other salts are included and available data on such dependencies are reviewed. Literature data evaluated by the International Union of Pure and Applied Chemistry (IUPAC) are revisited and additional and newer studies are supplemented to obtain a solid base of accurate experimental values. For temperatures higher than 100 °C the available data are scarce. For a temperature range from 0 to 100 °C, the reviewed investigations and data provide a good base to evaluate and adapt process models for processes in order to map precipitations issues accurately.

Keywords: solid-liquid phase equilibria; precipitation; SO₂ absorption; magnesium hydroxide slurry; sulfates; sulfites; hydroxides



Citation: Weiß, B.D.; Harasek, M. Solubility Data of Potential Salts in the MgO-CaO-SO₂-H₂O-O₂ System for Process Modeling. *Processes* **2021**, *9*, 50. <https://doi.org/10.3390/pr9010050>

Received: 30 November 2020

Accepted: 25 December 2020

Published: 29 December 2020

Publisher's Note: MDPI stays neutral with regard to jurisdictional claims in published maps and institutional affiliations.

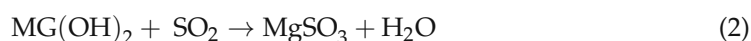


Copyright: © 2020 by the authors. Licensee MDPI, Basel, Switzerland. This article is an open access article distributed under the terms and conditions of the Creative Commons Attribution (CC BY) license (<https://creativecommons.org/licenses/by/4.0/>).

1. Introduction

The removal of SO₂ from exhaust gas using an absorptive magnesium-based slurry is a well-established method to control SO₂ emissions and simultaneously recover Sulfur as a resource of further usage. The pulp production industry using magnesium bisulfite as cooking liquor can ensure a nearly full chemical recovery if applying the absorption process in an optimized way.

After combustion, magnesium oxide is recovered from the ash, hydrated to magnesium hydroxide, and serves subsequently as absorbent. The absorption of SO₂ from the exhaust gas with hydrated magnesium oxide forms magnesium bisulfite, which serves again as cooking liquor. Equations (1)–(3) show the simplified reactions leading to the recovered cooking liquor.



This process allows the full reuse of required chemicals leading to a nearly closed-loop process control.

However, besides the intended reactions, unwanted precipitation reactions can occur under unideal process conditions. The precipitation of salts in the system highly influences the efficiency of the process. A high precipitation rate causes chemical loss as the

precipitated salts will be washed out in a regular cleaning step rather than recycled in the process [1]. Uncontrolled precipitation of salts therefore means interruption of the closed-loop process leading to an increased usage of fresh chemicals and to more frequent cleaning operations. This challenges not only the ecological footprint but also the economic feasibility.

To prevent precipitation and provide a cleaner and more efficient production, it is essential to understand the precipitation reactions in the system. Advanced process modeling can help in optimizing process conditions. A model, which covers the complex matter of precipitation reactions in electrolyte systems, requires the inclusion of all necessary dependencies sufficiently. Reliable literature data are of vital importance to ensure accuracy of the developed model. This makes a comprehensive review of available solubility data in the literature necessary.

While MgO, SO₂ and H₂O are process elements, CaO and O₂ can influence the reaction system as non-process elements. CaO can enter the process with process water and can consequently contribute to precipitation issues in the system. O₂ enters the process as remaining oxygen in the exhaust gas stream and can influence precipitation due to oxidation. To provide a comprehensive understanding of the precipitation process in the system, this review studies the solubility of salts in the MgO-CaO-SO₂-H₂O-O₂ system based on available literature data.

The following covers a comprehensive review of available solubility data for MgSO₃, CaSO₃, MgSO₄, CaSO₄, Mg(OH)₂ and Ca(OH)₂ as potential salts in the system. One major source for solubility data is the solubility data series of the International Union of Pure and Applied Chemistry (IUPAC) [2,3]. However, not all potential salts are covered in these evaluations. Therefore, this review includes additional data and also complements the data with newer studies to comprehensively review the state of the art of available solubility data. Furthermore, correlations describing the solubility reported in the literature are included and reviewed.

Based on the data, this paper recommends strategies for sufficiently accurate modeling of the precipitation. Although original data are partially given in molar units, this review gives all solubility data in g/100 g to provide consistency throughout the review.

2. Chemical System and Precipitation of Salts

Figure 1 visualizes simplified the chemical system leading to the formation and precipitation of sulfites, sulfates, and hydroxides in the studies system.

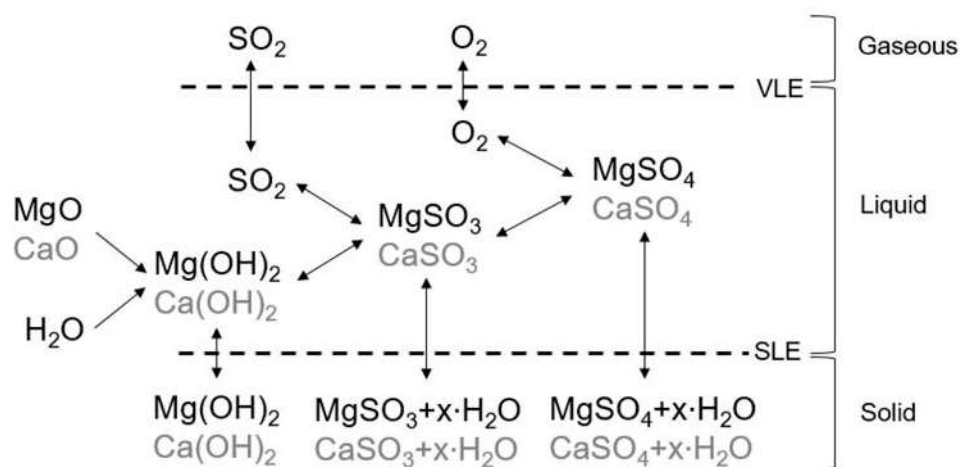


Figure 1. Chemical system leading to precipitations in the MgO-CaO-H₂O-SO₂-O₂ system.

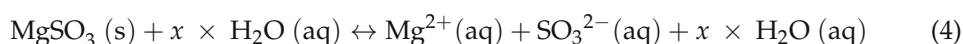
SO₂ and O₂ from the gas phase dissolve into the liquid phase according to the Vapor-Liquid-Equilibrium (VLE). The presence of Mg⁺ from dissolved Mg(OH)₂ (see Section 2.5) and the presence of SO₃—from dissolved SO₂ in the liquid phase lead to the formation

of MgSO_3 , $\text{Mg}(\text{OH})_2$ and MgSO_3 are intended products of the main process reactions (compare Equations (1)–(3)). $\text{Ca}(\text{OH})_2$ and CaSO_3 are formed in the presence of CaO as a non-process-element in the same manner. The presence of oxygen in the exhaust gas can lead to oxidation of sulfites and the formation of MgSO_4 and CaSO_4 [4]. $\text{Mg}(\text{OH})_2$, $\text{Ca}(\text{OH})_2$, MgSO_3 , CaSO_3 , MgSO_4 and CaSO_4 can precipitate in the system according to the Solid-Liquid-Equilibrium (SLE). The following focuses on the solubility of these potential salts.

Sulfites and Sulfates precipitate as different hydrates depending on process conditions [2]. The solubility of the hydrate forms can differ greatly. Understanding the stability behavior of these hydrate forms is therefore of great practical interest when developing a reliable process model.

2.1. Magnesium Sulfite (MgSO_3)

Equation (4) shows the solution equilibrium of MgSO_3 .



Lutz's evaluation in the Solubility Data Series of IUPAC reported that the stable hydrate form of MgSO_3 at temperatures lower than 37.85°C is hexahydrate ($\text{MgSO}_3 \cdot 6\text{H}_2\text{O}$). At temperatures higher than 37.85°C it is trihydrate ($\text{MgSO}_3 \cdot 3\text{H}_2\text{O}$) [2]. This report is based on the studies of Hagiwara, Okabe et al., Pinaev et al., and Lutz et al. [5]. However, a slow conversion rate from the metastable hexahydrate to trihydrate leads to the establishment of a metastable solubility equilibrium and the crystallization of hexahydrate even at temperatures higher than 37.85°C [6,7].

The conversion of hexahydrate to trihydrate is a pH and temperature depending process. Steindl et al. monitored the conversion using Raman Spectroscopy [1]. While at a temperature of 68°C the conversion was completed after around 50 min, at a temperature of 53°C the conversion was completed after around 580 min. The studies also showed an increasing conversion time with increasing starting pH value [1]. Following Steindl et al. a low pH value and high temperatures enhance therefore the conversion of hexahydrate to trihydrate. At temperatures higher than 40°C , magnesium hexahydrate has a higher solubility than trihydrate (see Figure 2). Preventing the conversion of hexahydrate to trihydrate is therefore of practical interest to lower precipitation.

2.1.1. Solubility of MgSO_3 Hydrates in Water

Figure 2 shows solubility data of magnesium hexa- and trihydrate in water.

The data found in the literature are mutually in very good agreement. The studies of Hagiwara and Markant were evaluated by Lutz in the IUPAC Solubility data series [2,5,8,9]. The data captured by Söhnel and Rieger and by Lowell et al. match those studies very well [6,8].

While the solubility of magnesium hexahydrate is increasing with temperature, the solubility of trihydrate is decreasing with temperature. This indicates that the dissolution of trihydrate is exothermic whereas the dissolution of hexahydrate is endothermic. Nyvlt was able to describe the temperature dependency of the solubility by correlating the data of Lowell, leading to the following equations with x being the molar fraction and T the temperature in K [10]:

$$\ln x_{\text{MgSO}_3 \cdot 6\text{H}_2\text{O}} = -82.918 - \frac{2668.11}{T} - 28.268 \log T \quad (5)$$

$$\ln x_{\text{MgSO}_3 \cdot 3\text{H}_2\text{O}} = -79.595 - \frac{4179.381}{T} - 25.435 \log T \quad (6)$$

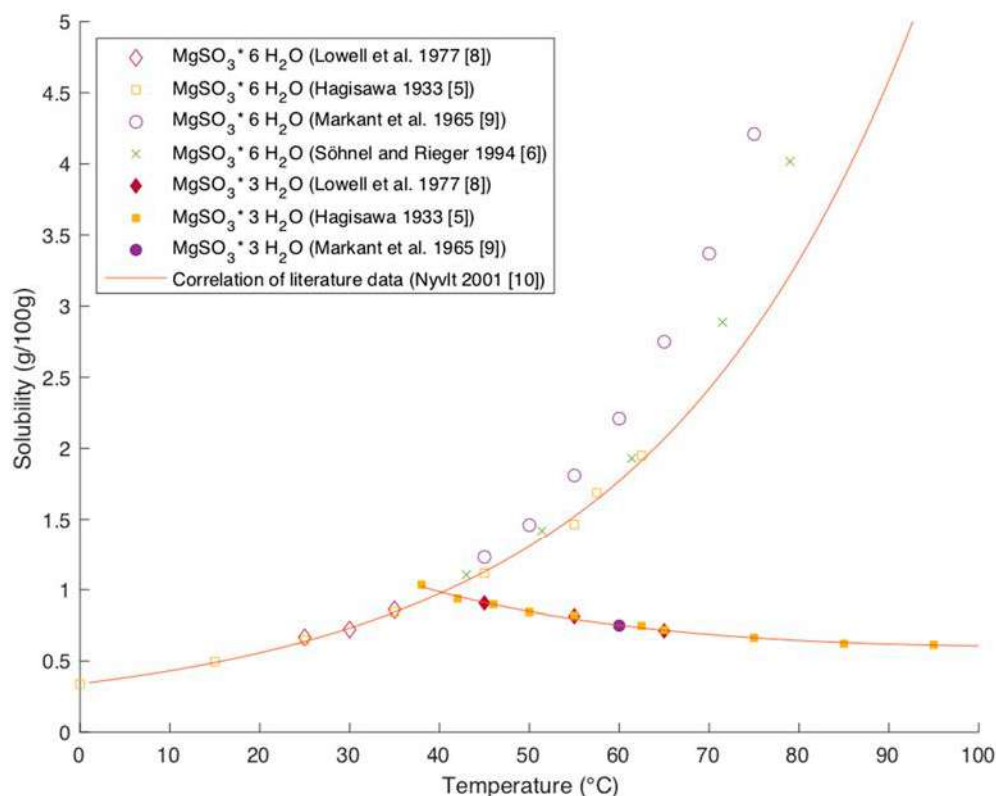


Figure 2. Solubility of MgSO₃ in Water [5,6,8–10].

The plot of these equations in Figure 2 shows a good correlation with existing literature data for trihydrate and hexahydrate at temperatures up to 60 °C. The correlation shows an increasing deviation from data points at higher temperatures.

The solubility of the two hydrate forms have an inverse dependency on temperature and the conversion times can be long. Consequently, occurring precipitation in the system is highly dependent on residence time and process conditions. While the given data provide a solid base for modeling purposes, a critical review of each given case is necessary to cover the change in solubility accurately.

However, the solubility of MgSO₃ in the MgO-CaO-SO₂-H₂O-O₂ system is not solely a function of temperature.

2.1.2. Influence of SO₂ on Solubility of MgSO₃ Hydrates

The solubility of MgSO₃ increases with increasing SO₂ content in the solution [2]. Figure 3 shows experimental data as well as a correlation of literature data of the solubility of magnesium sulfite over the SO₂ content in the solution at 25 °C [2,11].

Lutz recommends describing the change in solubility with the presence of SO₂ by following correlation with S being the Solubility of MgSO₃ in mol/kg and b the molality of SO₂ in mol/kg [2]:

$$S_{\text{MgSO}_3} = 0.0347 + 0.4885 \times b_{\text{SO}_2} \quad (7)$$

Figure 3 shows the good agreement of this correlation with the available experimental data by Conrad and Brice. The increasing solubility with an increasing SO₂ content can be explained with the formation of Mg(HSO₃)₂ (see Equation (3)). Several studies recorded an increasing amount of total dissolved magnesium sulfite with increasing amount of Mg(HSO₃)₂ in the MgSO₃-Mg(HSO₃)₂-H₂O system [2].

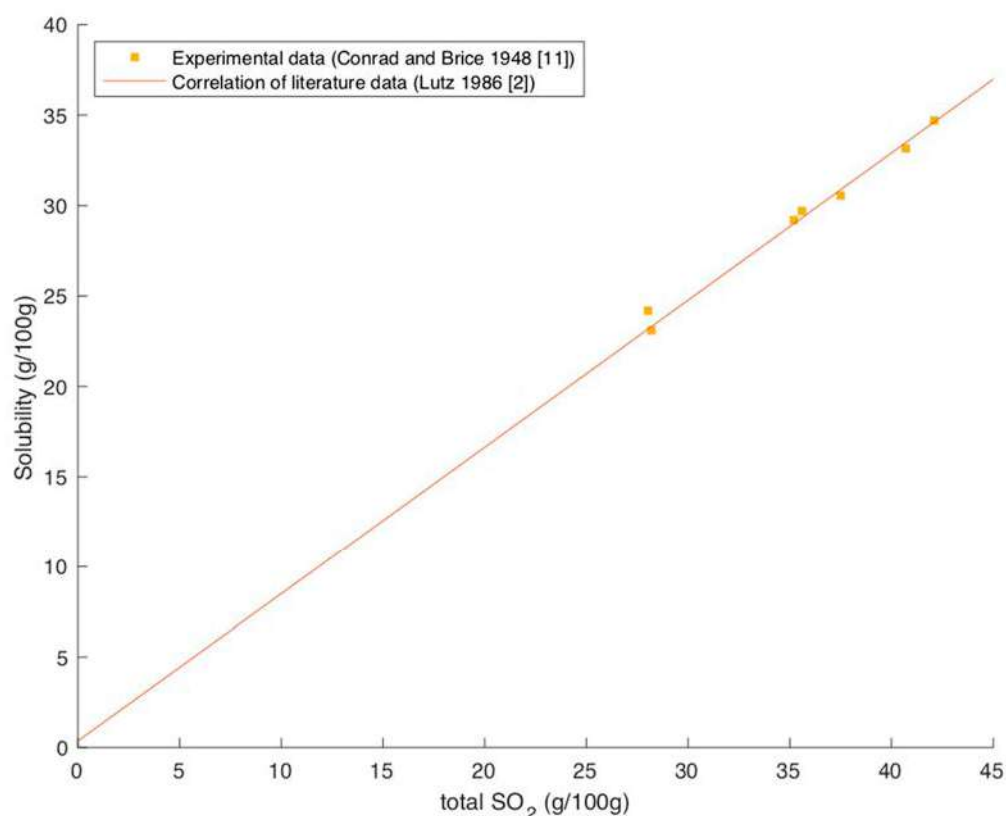


Figure 3. Solubility of MgSO₃ over total SO₂ content in the solution [2,11].

2.1.3. Influence of MgSO₄ on Solubility of MgSO₃ Hydrates

Several authors reported the influence of MgSO₄ on the solubility of MgSO₃. Figure 4 shows the solubility of MgSO₃ hexahydrate over the MgSO₄ content in the solution and Figure 5 the solubility of MgSO₃ trihydrate respectively. The presence of MgSO₄ may also influence whether trihydrate or hexahydrate is formed as stable form [6,8]. Pinaev explains this by the effect of MgSO₄ on the solution temperature and viscosity [8]. However, there are not enough studies found to confirm and characterize this influence sufficiently.

The data of Kovachev et al., 1970, Pinaev 1964 and Nvytl et al., 1977 are taken from the IPUAC solubility data series [2]. The experimental data for trihydrate and hexahydrate are in relatively good agreement with each other. All studies report an increase in solubility with increasing MgSO₄ content. Kovachev et al. covered the widest range of MgSO₄ content. The study covers the whole range of MgSO₄ content in which only MgSO₃ hydrates precipitate. At higher MgSO₄ contents than plotted in Figures 4 and 5, MgSO₄ hydrates precipitated besides MgSO₃ hydrates [2].

The data of Kovachev et al. show a maximum in solubility of MgSO₃ at MgSO₄ content of around 13 to 17 g per 100 g for trihydrate as well as for the hexahydrate [2]. The data for hexahydrate reported by Pinaev indicate as well that the solubility stabilizes when reaching a certain amount of MgSO₄ [2]. Lowel et al. present a graph showing the dependency between MgSO₄ content and the solubility of MgSO₃ hexahydrate based on values reported by Pinaev and McGlamery et al. [8].

The data of Söhnel and Kovachev et al. show that the effect of the presence of MgSO₄ on the solubility of MgSO₃ trihydrate is smaller for lower temperatures [2,6].

Nývtl correlated literature data to describe the influence of MgSO₄ on the solubility of hexahydrate with the following equation with S being the Solubility in kg/kg H₂O and x_{MgSO_4} being the content of MgSO₄ in kg/kg H₂O [10]:

$$S_{\text{MgSO}_3} = \left(1 + 8.54 \times x_{\text{MgSO}_4} - 28.92 \times x_{\text{MgSO}_4}^2\right) \times S_{\text{MgSO}_3 \text{ in water}} \quad (8)$$

Figure 4 shows the plot of this correlation for the solubility at 35 °C, 50 °C and 70 °C. While at 35 °C the correlation shows good agreements with experimental data, at higher temperatures the correlation increasingly underestimates the solubility of MgSO_3 with increasing MgSO_4 content.

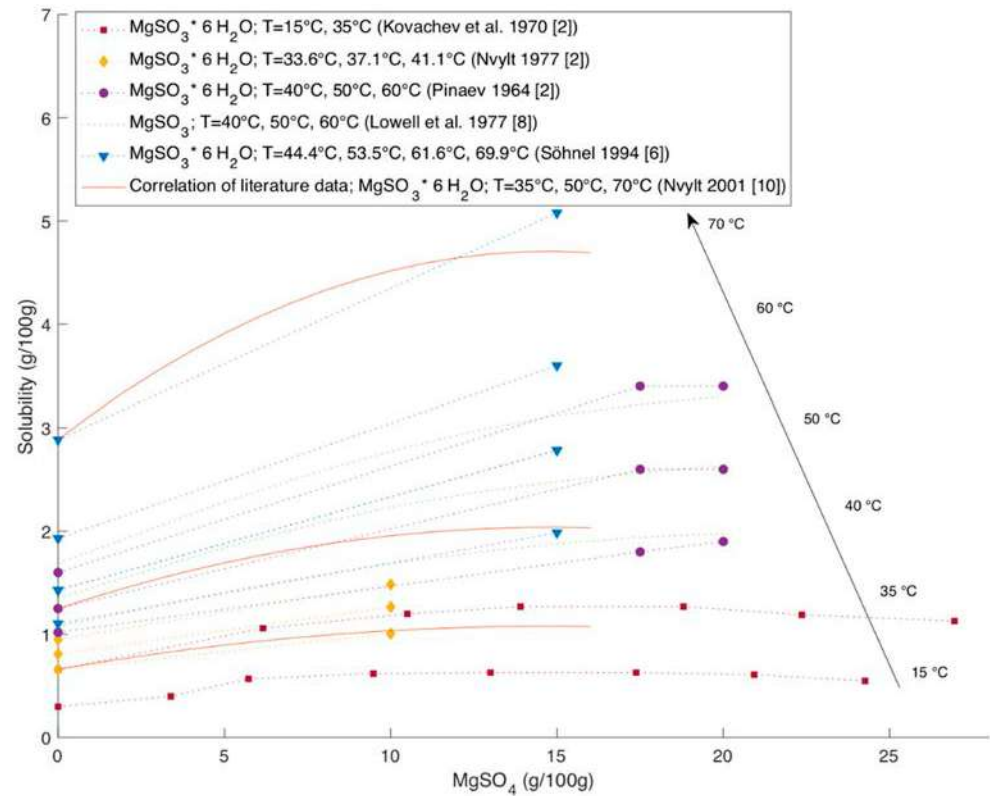


Figure 4. Solubility of MgSO_3 hexahydrate over MgSO_4 content at different temperatures [2,6,10].

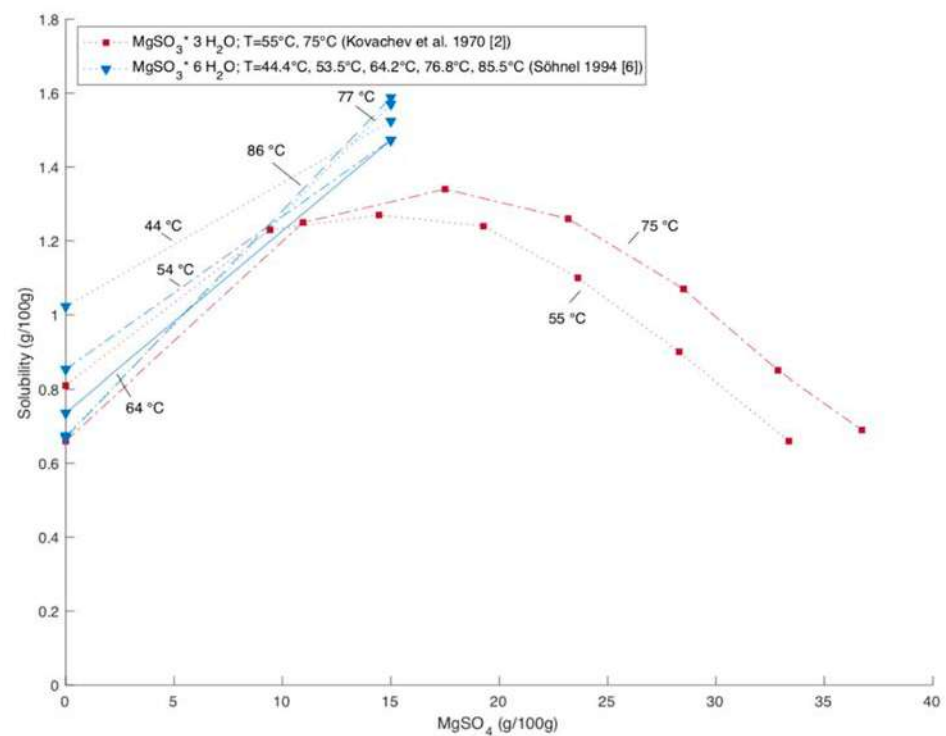
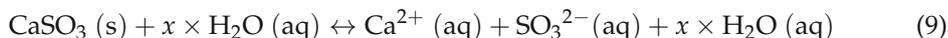


Figure 5. Solubility of MgSO_3 trihydrate over MgSO_4 content at different temperatures [2,6].

2.2. Calcium Sulfit (CaSO_3)

Equation (9) shows the solution equilibrium of CaSO_3 in water:



Lutz states in the IUPAC solubility series that CaSO_3 precipitates primarily as hemihydrate ($\text{CaSO}_3 \cdot 1/2\text{H}_2\text{O}$). The existence of dihydrate ($\text{CaSO}_3 \cdot 2\text{H}_2\text{O}$) and tetrahydrate ($\text{CaSO}_3 \cdot 4\text{H}_2\text{O}$) was also reported but not confirmed for the CaSO_3 - H_2O system [2].

2.2.1. Solubility of CaSO_3 Hydrates in Water

The solubility data of CaSO_3 in the literature are scarce and existing data scatter over a wide range. Lutz evaluated in the IUPAC solubility several studies found in the literature [2]. Based on the evaluated data, Lutz recommends a solubility value of 0.0054 g/100 g of water at 25 °C. However, this value comes with a deviance of ± 0.0012 g/100 g, which corresponds to around 22%. Lutz explains this strong scatter with the existence of different modifications of $\text{CaSO}_3 \cdot 1/2\text{H}_2\text{O}$ and its tendency to form supersaturated solutions [2].

Figure 6 shows the literature data of Bobrovnik and Kotelnikova and van der Linden, which were identified as the most accurate by Lutz, as wells as the newer data of Malghe and Kumar [2,12–14].

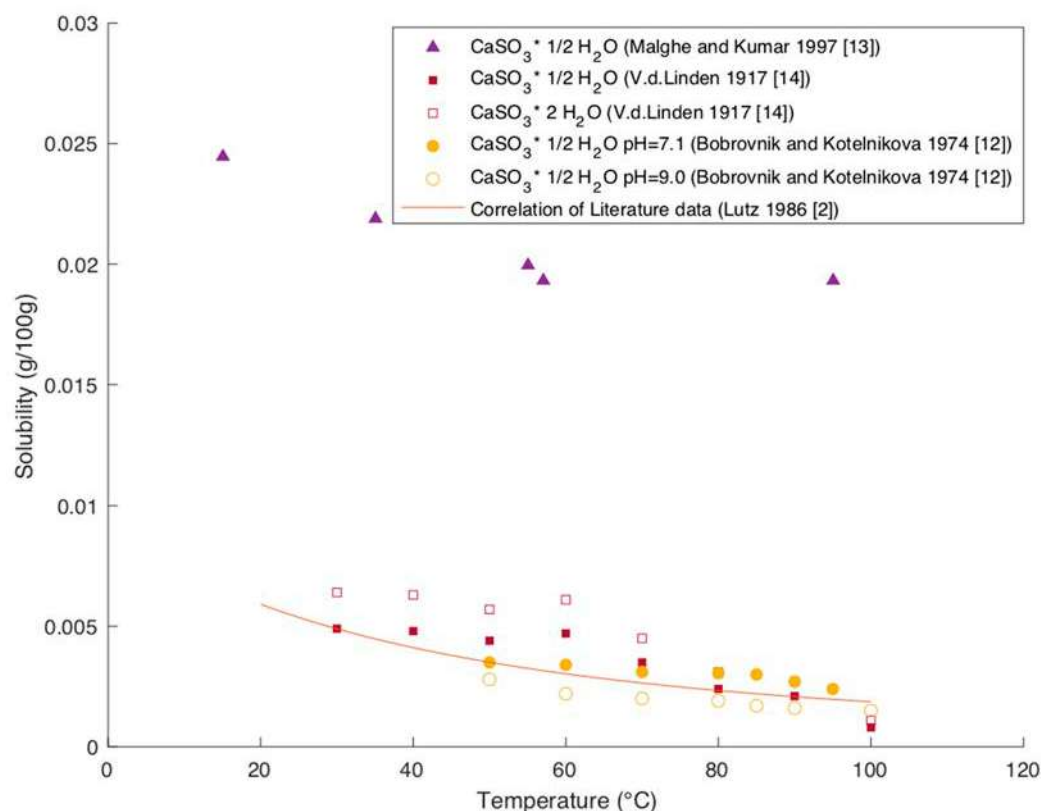


Figure 6. Solubility of CaSO_3 in water [2,12–14].

The original data reported by Van Der Linden give the solubility for CaSO_3 dihydrate [14]. Due to the conclusion that the stable form is the hemihydrate, the solubility for hemihydrate is given in the IUPAC solubility series as calculated values based on the data reported by Van der Linden [2]. All data show a decrease in solubility with increasing temperature. The data from Malghe and Kumar strongly deviate from other literature data and greatly extend the deviance stated by Lutz. As the study does not specify the form of the analyzed CaSO_3 and due to the strong discrepancy, it is recommended to exclude these values for modeling purposes.

Lutz was able to correlate the literature data from Bobrovnik and Kotelnikova and van der Linden using the following equation with S as the solubility in mol/K and T as the temperature in Kelvin [2]:

$$\log S = -15.367 - \frac{1155.67}{T} - 3.290 \log T \quad (10)$$

The plot of this correlation in Figure 6 shows good agreement with the literature data when excluding the data by Malghe and Kumar [13].

2.2.2. Influence of SO₂ on Solubility of CaSO₃ Hydrates

As for the MgSO₃-SO₂-H₂O system, the SO₂ content also has an increasing effect on the solubility of CaSO₃ [2]. Figure 7 shows the solubility of CaSO₃ over the total SO₂ content in the solution at 25 °C.

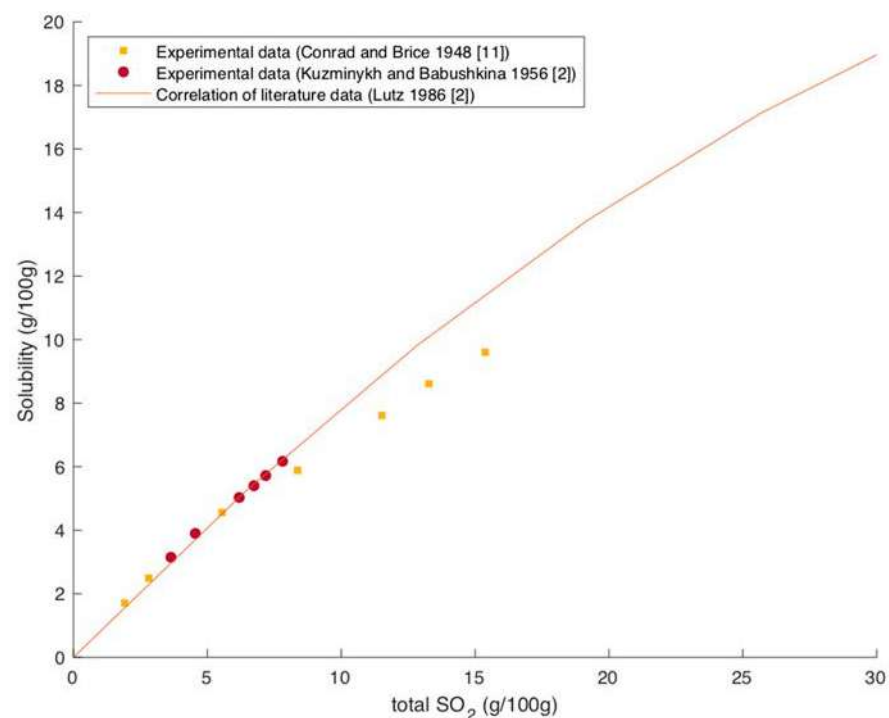


Figure 7. Solubility of CaSO₃ over total SO₂ content in the solution [2,11].

The data from Kuzminykh and Babushkina in 1956 are taken from the IUPAC solubility data series [2]. Lutz recommends describing the change in solubility with the presence of SO₂ by following correlation with S being the Solubility of CaSO₃ in mol/kg and b the molality of SO₂ in mol/kg.

$$S_{\text{CaSO}_3} = 0.460 \times b_{\text{SO}_2} - 0.026 \times b_{\text{SO}_2}^2 \quad (11)$$

Figure 7 shows the applicability of this correlation for an SO₂ content up to 10 g per 100 g water. For higher SO₂ contents, the correlation slightly overestimates the solubility compared to the data from Conrad and Brice.

As for MgSO₃, the increasing solubility with increasing SO₂ content can be explained with the formation of Ca(HSO₃)₂.

2.2.3. Influence of CaSO₄ on Solubility of CaSO₃ Hydrates

CaSO₄ has a decreasing effect on the solubility of CaSO₃ [2]. Figure 8 shows solubility data of CaSO₃ in water and in solution, which is saturated with CaSO₄ over temperature.

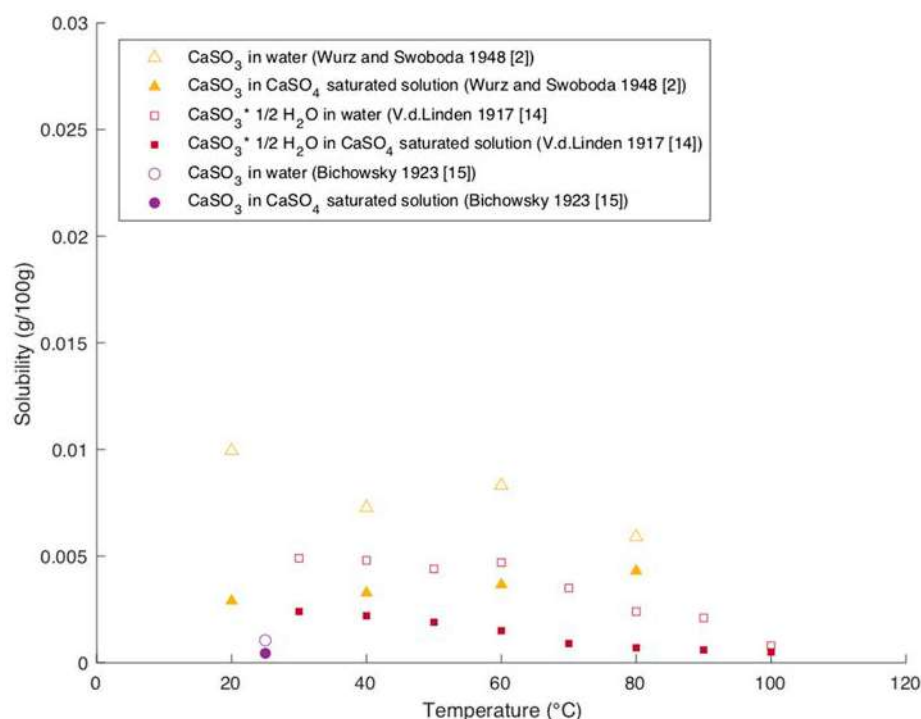
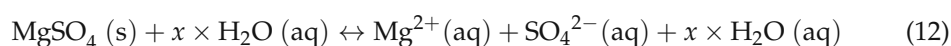


Figure 8. Solubility of CaSO_3 in water and in CaSO_4 saturated solution [2,14,15].

All reported data show a significant decrease in the solubility of CaSO_3 in a solution, which is saturated with CaSO_4 compared to the solubility in water. The effect of decreasing solubility is on average around -58% and maximum -75% . Unlike for MgSO_3 , there are no data reported, which analyze the effect of different sulfate concentrations on the solubility of CaSO_3 .

2.3. Magnesium Sulfate (MgSO_4)

Equation (12) shows the solution equilibrium of MgSO_4 :



Many studies have examined the stability of different hydrate forms of MgSO_4 [16–20]. Following the study by Li et al. MgSO_4 exists stably as kieserite ($\text{MgSO}_4 \cdot \text{H}_2\text{O}$) and hexahydrate ($\text{MgSO}_4 \cdot 6\text{H}_2\text{O}$) at 50°C and only as kieserite at 75°C in the MgCl_2 - MgSO_4 - H_2O system [18]. Starksyite ($\text{MgSO}_4 \cdot 4\text{H}_2\text{O}$) was recognized as metastable form at both temperatures and pentahydrate ($\text{MgSO}_4 \cdot 5\text{H}_2\text{O}$) as metastable form at 50°C . In a very recent study, Dongdong et al. have developed a thermodynamic model to predict the thermodynamic behavior of the $\text{Mg}(\text{OH})_2$ - MgSO_4 - H_2O system. The model defines heptahydrate ($\text{MgSO}_4 \cdot 7\text{H}_2\text{O}$) as stable form at temperatures lower than 45.85°C , hexahydrate for the temperature range of around 45.85 to 71.85°C and kieserite for temperatures higher than 71.85°C [20]. A solubility diagram of the MgSO_4 - H_2O system presented by Steiger et al. supports this observation giving similar temperature windows for the existence of heptahydrate, hexahydrate and kieserite as stable hydrate forms of MgSO_4 [17]. Nevertheless, several metastable hydrate forms, such as starksyite or pentahydrate, may coexist in this temperature range [16–18] and different studies give partially contradictory new insights in the complicated reaction system [18].

Solubility of MgSO_4 Hydrates in Water

Figure 9 presents measured and correlated solubilities of the different hydrate forms over temperature.

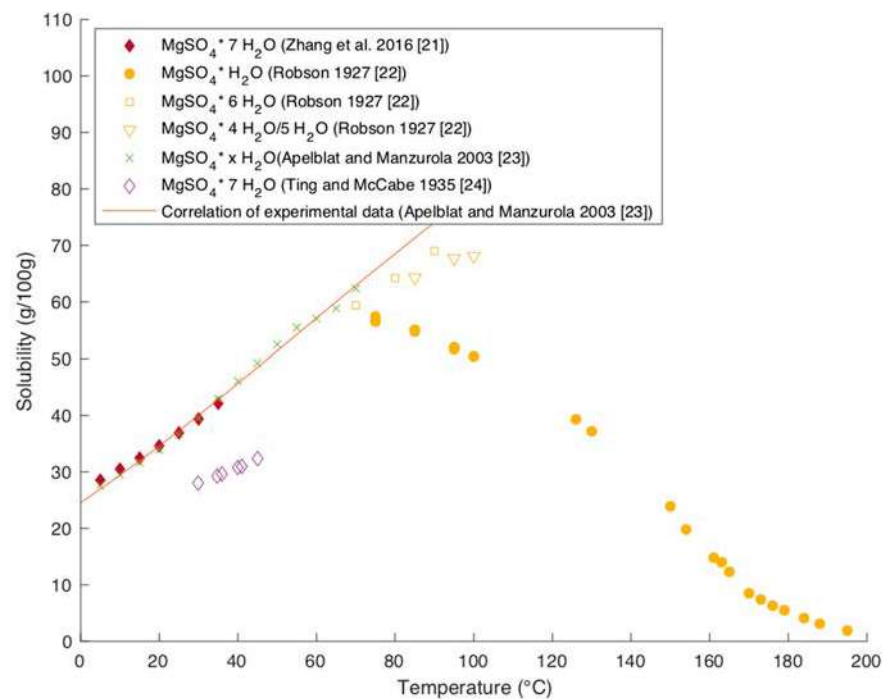


Figure 9. Solubility of MgSO_4 in water [21–24].

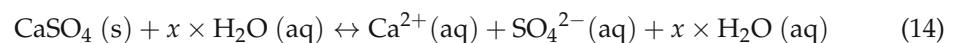
The solubility of MgSO_4 salts in water is almost by factor 100 higher than the solubility of MgSO_3 hydrates (compare Figures 2 and 9). Except for kieserite, the different hydrate forms show a similar solubility behavior. The data from Ting and McCabe report around 25% lower solubility than the other data. Otherwise, the data are in very good agreement with each other. The solubility of all hydrate forms except kieserite increases with increasing temperature. Apelblat and Manzurola correlated their data with the following equation with S being the Solubility in mol/kg and T being the temperature in K [23]:

$$\ln S = 39.172 - \frac{2795.9}{T} - 5.0309 \ln T \quad (13)$$

This correlation describes the solubility of all hydrate forms up to a temperature of 70 °C well when excluding the data from Ting and McCabe (see Figure 9). At higher temperatures, the solubility decrease of kieserite reported by Robson needs to be taken into account and cannot be covered by the given correlation.

2.4. Calcium Sulfate (CaSO_4)

Equation (14) describes the solution equilibrium of CaSO_4 in water:



Several studies report three main forms of CaSO_4 , which is hemihydrate ($\text{CaSO}_4 \cdot 1/2\text{H}_2\text{O}$), dihydrate ($\text{CaSO}_4 \cdot 2\text{H}_2\text{O}$), and anhydrite (CaSO_4) [25,26]. While dihydrate is recognized as the stable form at temperatures lower than 40 °C and anhydrite at higher temperatures, hemihydrate is a metastable form and can coexist at temperatures around 90 to 130 °C [27–29].

2.4.1. Solubility of CaSO_4 Hydrates in Water

The solubility of the different CaSO_4 hydrates was studied by several researchers [25,28–33]. The data are summarized in Figure 10.

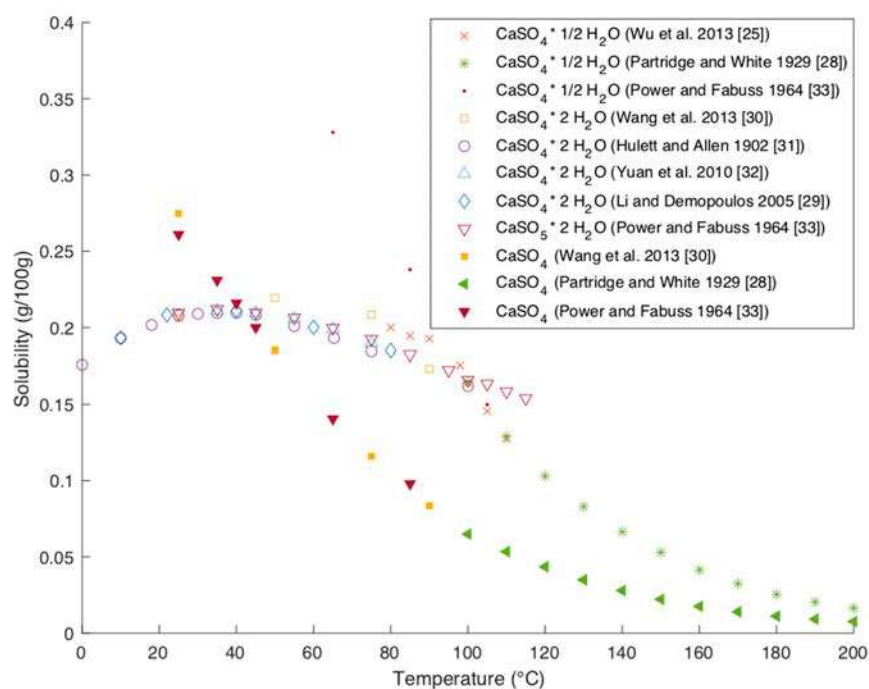


Figure 10. Solubility of CaSO_4 in water [25,28–33].

The newer data are in good agreement with older data, which indicates good accuracy of the data. The solubility curves are clearly distinguishable between the three different hydrate forms. While the solubility of dihydrate increases with temperature in the stable window to up to 40 °C, a further increase in temperature leads to a decrease in solubility for all hydrate forms. The phenomenon that the solubility of dihydrate starts decreasing at around 40 °C can be explained thermodynamically with the change of the sign of the heat of solution [31].

2.4.2. Influence of Mg^{++} on Solubility of CaSO_4 Hydrates

The presence of magnesium and calcium can influence each other's solubility. Several authors have reported the association effect of magnesium, which increases the solubility of CaSO_4 with an increasing presence of magnesium cations as the cation associates the partial sulfate ion to form stable MgSO_4 [25,34]. As a consequence of the formation of MgSO_4 the solubility of CaSO_4 increases. Wu et al. studied the influence of magnesium chloride on the solubility of CaSO_4 . They report that at a MgCl_2 content of around 9 mol/kg the solubility of CaSO_4 dihydrate is around half the solubility at the same temperature in water [25].

2.5. Magnesium Hydroxide ($\text{Mg}(\text{OH})_2$)

When describing the solubility of $\text{Mg}(\text{OH})_2$ in an aqueous solution, two main equilibria need to be considered. One is the dissociation of $\text{Mg}(\text{OH})_2$ and the other is the formation of the ion pair MgOH^+ .



Therefore the solubility of $\text{Mg}(\text{OH})_2$ is a distinctive function of the pH value of the solution [3,35]. Scholz and Kahlert studied the pH dependence of the solubility of metal hydroxides and established an equation describing the solubility $S_{\text{Mg}(\text{OH})_2}$ as a function of pH, the solubility product $K_{\text{sol}, \text{Mg}(\text{OH})_2}$ and the autoprotolysis constant of water K_w [35]:

$$\log S_{\text{Mg}(\text{OH})_2} = \log K_{\text{sol}, \text{Mg}(\text{OH})_2} + 2\log K_w - 2\text{pH} \quad (17)$$

This equation is based on the consideration that formed OH^- ions are part of the autoprotolysis reaction of water and takes the following definitions into account [35]:

$$S_{\text{Mg}(\text{OH})_2} = c_{\text{Mg}^{2+}} \quad (18)$$

$$K_{\text{sol, Mg}(\text{OH})_2} = c_{\text{Mg}^{2+}} \times c_{\text{OH}^-}^2 \quad (19)$$

$$K_W = c_{\text{H}_3\text{O}^+} \times c_{\text{OH}^-} \quad (20)$$

$$\text{pH} = -\log c_{\text{H}_3\text{O}^+} \quad (21)$$

Knowing the solubility product of $\text{Mg}(\text{OH})_2$ this equation allows an easy calculation at which pH value the precipitation of $\text{Mg}(\text{OH})_2$ starts at a given temperature. While a lower pH value is leading to a higher solubility, $\text{Mg}(\text{OH})_2$ is almost insoluble at neutral pH or higher.

Solubility of $\text{Mg}(\text{OH})_2$ in Water

Lambert and Clever evaluated comprehensively available data in the IUPAC solubility data series [3]. Figure 11 shows solubility data of $\text{Mg}(\text{OH})_2$ in water.

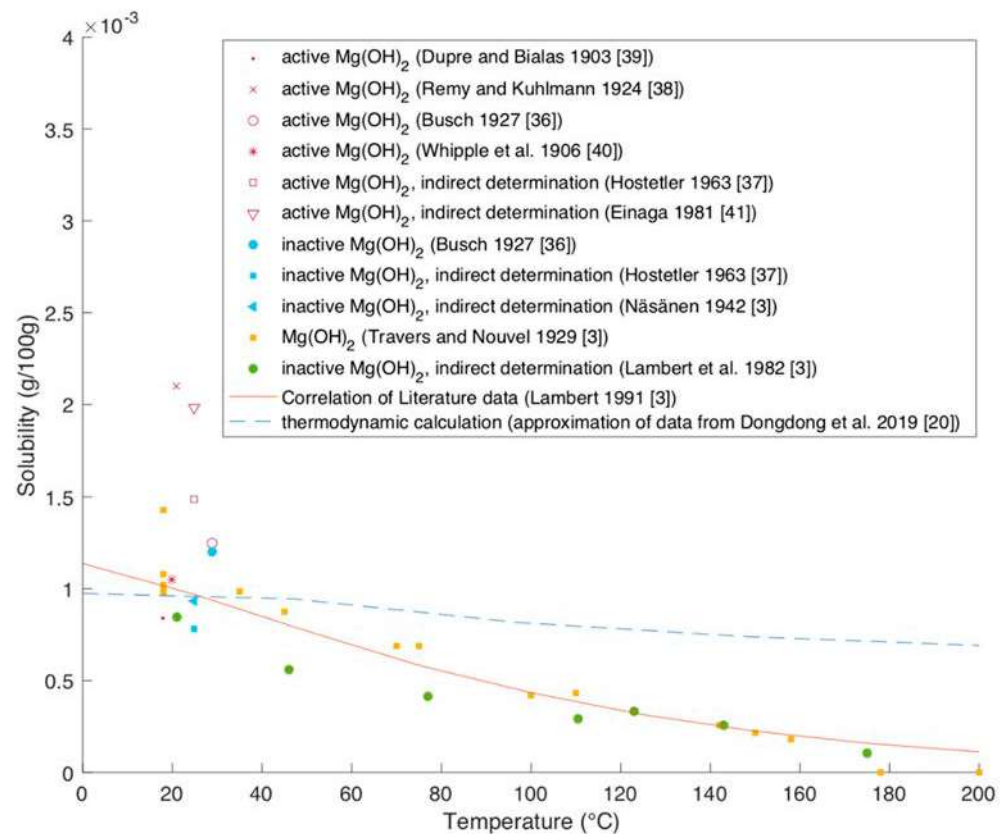


Figure 11. Solubility of $\text{Mg}(\text{OH})_2$ in water [3,20,36–41].

The data from Näsänen (1942), Travers and Nouvel (1929), and Lambert (1982) were taken from the IUPAC solubility data series [3]. Due to the low solubility, the direct measurement of a precise value is difficult. Therefore, several studies derived the solubility in water indirectly from the solubility product determined by measurements in a ternary system [3]. These values are designated as indirect determination in Figure 11. Literature data distinguish between active and inactive $\text{Mg}(\text{OH})_2$. Active $\text{Mg}(\text{OH})_2$ describes the amorphous form of $\text{Mg}(\text{OH})_2$ after precipitation or hydration of MgO . Aging leads to a thermodynamic stable form with a lower solubility described as inactive $\text{Mg}(\text{OH})_2$ [3]. Several studies focused on the solubility change from active to inactive $\text{Mg}(\text{OH})_2$ [36,37]. Although

there is a general trend visible that active $\text{Mg}(\text{OH})_2$ has a higher solubility, the spread of data points at room temperature makes it impossible to derive a systematic trend [3]. While the direct measurements done by Busch show only a slight decrease of solubility with progressing aging, Hostetler observed a solubility decrease by almost 50% [36,37]. As the value for the active $\text{Mg}(\text{OH})_2$ from Busch is taken after 8 h of equilibration time, the small decrease can be explained with an already progressed aging at this time.

While there are several studies analyzing the solubility at room temperature, there are only a few studies covering a wider temperature range. Travers and Nouvel performed direct measurements of the solubility in water, Lambert and Clever determined the solubility indirectly [3]. Lambert and Clever explain the difference between the values of these two studies with insufficient aging of the $\text{Mg}(\text{OH})_2$ by Travers and Nouvel [3]. Correlating the literature data Lambert and Clever recommend the following equation to describe the tentative values for the solubility of $\text{Mg}(\text{OH})_2$ in water as a function of temperature with S being the solubility in mol/kg and T the temperature in Kelvin [3]:

$$\ln S = 81.965 - \frac{3432.07}{T} - 13.893 \ln T \quad (22)$$

The plot of this correlation in Figure 11 shows a good agreement with experimental data for temperatures higher than 20 °C.

In a very recent study, Dongdong et al. developed several thermodynamic models to describe the $\text{Mg}(\text{OH})_2\text{-H}_2\text{O}$ system based on the CALPHAD methodology [20]. The model describes the thermodynamic properties of the system through the Gibbs free energy. Adjustable parameters allow the optimization of the model by fitting it to literature data. They were able to describe the system by fitting the adjustable parameters to solubility data described in the literature. However, they found that using the previously described literature data to fit the model leads to inconsistent thermodynamic results. Whereas a model using the solubility product given by McGee and Hostetler to complement the determination of the Gibbs energy equation showed consistency at least in the temperature window from 0 °C to 50 °C [20,42]. The solubility product reported by McGee and Hostetler shows only a small temperature dependency with $-\log(K) = 10.89$ at 10 °C and $-\log(K) = 11.10$ at 90 °C [42]. Especially at higher temperatures, the model based on these values shows a high deviation from solubility data found in the literature (see Figure 11) [20]. Dongdong et al. conclude that the limitations in modeling the $\text{Mg}(\text{OH})_2\text{-H}_2\text{O}$ system are due to the general lack of reliable experimental data of the solubility of $\text{Mg}(\text{OH})_2$.

2.6. Calcium Hydroxide $\text{Ca}(\text{OH})_2$

Equation (23) shows the solution equilibrium of $\text{Ca}(\text{OH})_2$:



Like $\text{Mg}(\text{OH})_2$, the solubility of $\text{Ca}(\text{OH})_2$ depends on the state of aging and the pH value of the solution. Following the study by Scholz and Kahlert, the pH dependency of the solubility can be expressed in the same way as for $\text{Mg}(\text{OH})_2$ with the solubility product of $\text{Ca}(\text{OH})_2$ respectively, leading to the following equation [35]:

$$\log S_{\text{Ca}(\text{OH})_2} = \log K_{\text{sol, Ca}(\text{OH})_2} + 2\log K_w - 2\text{pH} \quad (24)$$

The evaluation of solubility data of $\text{Ca}(\text{OH})_2$ by Lambert and Clever revealed that the difference in solubility between fresh and aged $\text{Ca}(\text{OH})_2$ decreased with increasing temperature and was in general small [3]. Which justifies the focus on the solubility of aged $\text{Ca}(\text{OH})_2$ only.

Solubility of Ca(OH)₂ in Water

Figure 12 shows the solubility of Ca(OH)₂ over temperature. Except for the data of Yuan et al. all shown literature data were evaluated by Lambert and Clever in the IUPAC solubility data series [3].

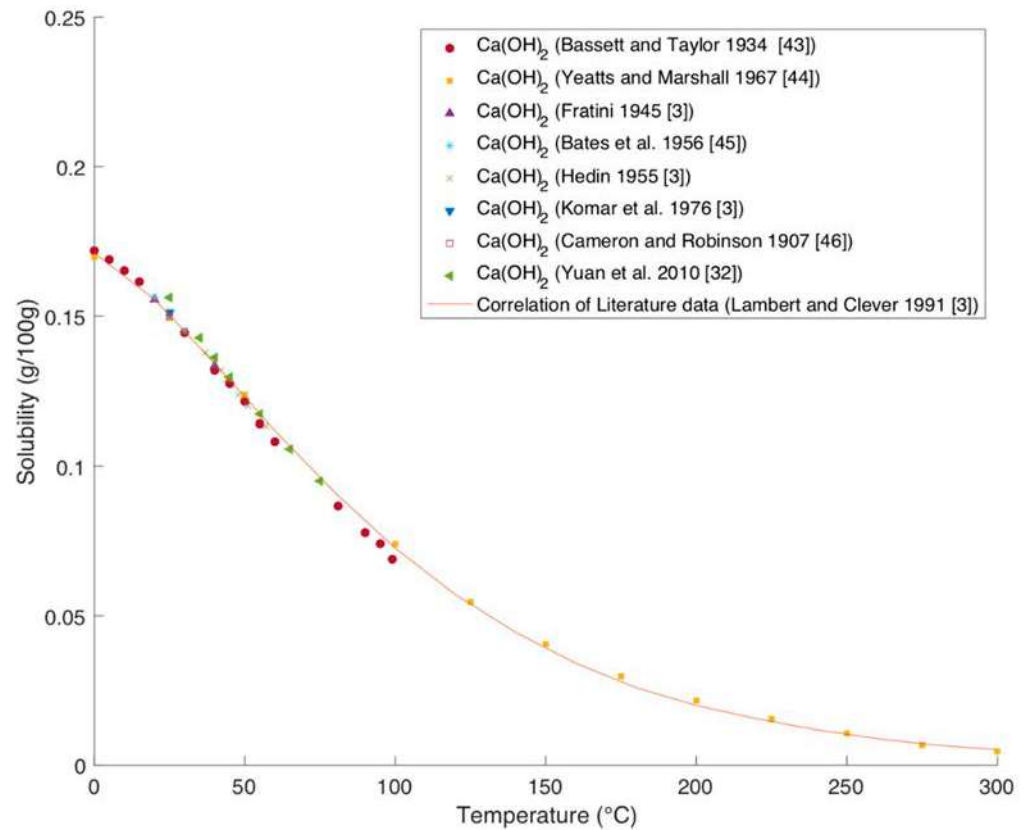


Figure 12. Solubility of Ca(OH)₂ in water [3,32,43–46].

The data from Fratini (1945), Hedin (1955), and Komar et al. (1976) were taken from the IUPAC solubility series [3]. The newer and older data are in very good agreement with each other. The solubility is around 100 times lower than for Mg(OH)₂ and decreases with increasing temperatures.

Lambert and Clever were able to correlate the literature data using the following equation with S being the solubility in mol/kg and T the temperature in Kelvin [3]:

$$\ln S = 86.1534 - \frac{3492.14}{T} - 13.7494 \ln T \quad (25)$$

Also the younger experimental data of Yuan et al. fit the correlation very nicely, which confirms the applicability of that correlation [3,32].

3. Conclusions

Solubility data for MgSO₃, CaSO₃, MgSO₄, CaSO₄, Mg(OH)₂ and Ca(OH)₂ were summarized and reviewed to provide a solid base for modeling purposes.

To cover the precipitation of MgSO₃ the solubility of its hexa- and trihydrate needs to be taken into account. The existence of these hydrate forms depends on the process conditions. Available solubility data for both hydrates cover a temperature range of 0 to 100 °C and are in good agreement with each other. The inverse dependency on temperature of the two hydrate forms makes it necessary to critical review, which hydrate form occurs under the given conditions in the process prior to its modeling.

The solubility data of CaSO_3 are scarce, and only for a temperature range of 50 to 100 °C is more than one corresponding data source available. CaSO_3 precipitates as different hydrate forms. However, the solubility behavior of these hydrate forms does not differ apparently. A differentiated consideration of the single hydrate forms is therefore not required to model precipitation accurately.

Much data reports the influence of the sulfates MgSO_4 and CaSO_4 on MgSO_3 and CaSO_3 respectively. To describe the precipitation accurately, it is essential to include this influence into a process model.

Investigations on the precipitation of MgSO_4 report multiple existences of metastable hydrate forms varying with temperature and relative humidity and sluggish kinetics [16,17,19]. The available solubility data of MgSO_4 cover a temperature range of 0 to 200 °C. The available data for each single hydrate form are scarce. The solubility behavior of all studied hydrate forms except kieserite do not differ apparently. The available data imply that the different hydrate forms can be described together based on their combined data. The solubility of kieserite however shows an inverse temperature dependency and needs to be considered separately.

The precipitation and solubility of CaSO_4 are well studied. To cover the solubility behavior accurately, the hemihydrate, the monohydrate and the dihydrate need to be taken into account. For all hydrate forms, more than one data source is available for a temperature range of 0 to 100 °C. All available data are in very good agreement with each other.

Studies of the solubility of Mg(OH)_2 and Ca(OH)_2 show that at pH value lower than 7, the precipitation of the hydroxides can be disregarded when modeling an industrial process. A change to higher pH values, however, can cause heavy precipitation. Mg(OH)_2 is almost insoluble in water. The precise values of the solubility scatter at room temperature between around 0.75×10^{-3} and 2×10^{-3} g/100 g, partially explained by the solubility difference of active and inactive Mg(OH)_2 . Only two data sources are available for a wider temperature range of up to 200 °C, which show a corresponding trend. The solubility of Ca(OH)_2 in water is well studied by many different researchers in a temperature range of 0 to 100 °C. All available data are in very good agreement with each other. For temperatures higher than 100 °C only one data set was found, which blends very well with the data for lower temperatures.

Author Contributions: Conceptualization, B.D.W. and M.H.; investigation, B.D.W.; writing—original draft preparation, B.D.W.; writing—review and editing, B.D.W. and M.H.; visualization, B.D.W.; supervision, M.H.; project administration, M.H.; funding acquisition, M.H. All authors have read and agreed to the published version of the manuscript.

Funding: This work was financially supported by the Competence Center CHASE GmbH. CHASE Competence Center is subsidized in the frame of COMET—Competence Centers for Excellent Technologies by BMVIT, BMWFW, Wirtschaftsagentur Wien, State of Upper Austria and its scientific partners. The COMET program is handled by FFG.

Data Availability Statement: No new data were created or analyzed in this study. Data sharing is not applicable to this article.

Acknowledgments: The support by the project partner Sappi Papier Holding GmbH is greatly acknowledged. Open Access Funding by TU Wien.

Conflicts of Interest: The authors declare no conflict of interest. The funders had no role in the design of the study; in the collection, analyses, or interpretation of data; in the writing of the manuscript, or in the decision to publish the results.

References

1. Steindl, M.; Röder, T.; Simharl, R.; Harasek, M.; Friedl, A.; Sixta, H. Online Raman monitoring of the phase transition of magnesium sulphite hydrate. *Chem. Eng. Process. Process. Intensif.* **2005**, *44*, 471–475. [CrossRef]
2. Lutz, H.D. Sulfites, Selenites and Tellurites. *Solubility Data Ser.* **1986**, *26*, 153–193.
3. Lambert, I.; Clever, H.L. Alkaline Earth Hydroxides in Water and aqueous solutions. *Solubility Data Ser.* **1992**, *52*, 49–226.

4. Li, Q.; Yang, Y.; Wang, L.; Xu, P.; Han, Y. Mechanism and kinetics of magnesium sulfite oxidation catalyzed by multiwalled carbon nanotube. *Appl. Catal. B Environ.* **2017**, *203*, 851–858. [[CrossRef](#)]
5. Hagiwara, H. Studies of Magnesium Sulphite. *Bull. Inst. Phys. Chem. Res.* **1933**, *12*, 976–983.
6. Söhnel, O.; Rieger, A. Solubilities of Magnesium Sulfite Hydrates. *J. Chem. Eng. Data* **1994**, *39*, 161–162. [[CrossRef](#)]
7. Söhnel, O.; Rieger, A. Phase Transition of Magnesium Sulphite Hydrates in Aqueous Suspension. *Cryst. Res. Technol.* **1993**, *28*, 487–493. [[CrossRef](#)]
8. Lowell, P.S.; Meserole, F.P.; Parsons, T.B. *Precipitation Chemistry of Magnesium Sulfite Hydrates in Magnesium Oxide Scrubbing*; Interagency Energy-Environment Research and Development Series; Radian Corp.: Austin, TX, USA, 1977; EPA-600/7-77/109.
9. Markant, H.P.; Mc LROY, R.A.; Matty, R.E. Absorption Studies—MgO-SO₂ Systems. *Tappi J.* **1962**, *45*, 849–854.
10. Nyvlt, J. Solubilities of Magnesium Sulfite. *J. Therm. Anal. Calorim.* **2001**, *66*, 509–512. [[CrossRef](#)]
11. Conrad, F.H.; Brice, D.B. Some Equilibrium Relations in the System Magnesium Oxide—Sulfur Dioxide—Water (Acid Region) at Pressures below Atmospheric. *J. Am. Chem. Soc.* **1948**, *70*, 2179–2182. [[CrossRef](#)]
12. Bobrovnik, L.D.; Kotelnikova, L.P. Solubility of calcium sulphite in sugar solutions. *Izv. Vyssh. Uchebn. Zaved. Pishch. Tekhnol.* **1974**, *4*, 155–156.
13. Malghe, Y.S.; Kumar, A. Solubility of CaSO₃ in aqueous sucrose solutions from 288 to 368 K. *Indian J. Chem. Sect. A* **1998**, *37*, 56–58.
14. Van der Linden, T. Solubility of calcium sulphite in water and in sugar solutions. *J. Chem. Technol. Biotechnol.* **1917**, *36*, 96. [[CrossRef](#)]
15. Bichowsky, F.R. Free energy of the thiosulfate ion. *J. Am. Chem. Soc.* **1923**, *45*, 2225–2235. [[CrossRef](#)]
16. Chipera, S.J.; Vaniman, D.T. Experimental stability of magnesium sulfate hydrates that may be present on Mars. *Geochim. Cosmochim. Acta* **2007**, *71*, 241–250. [[CrossRef](#)]
17. Steiger, M.; Linnow, K.; Ehrhardt, D.; Rohde, M. Decomposition reactions of magnesium sulfate hydrates and phase equilibria in the MgSO₄-H₂O and Na⁺-Mg²⁺-Cl⁻-SO₄²⁻-H₂O systems with implications for Mars. *Geochim. Cosmochim. Acta* **2011**, *75*, 3600–3626. [[CrossRef](#)]
18. Li, H.; Zeng, D.; Yao, Y.; Gao, C.; Yin, X.; Han, H. Solubility Phase Diagram of the Ternary System MgCl₂-MgSO₄-H₂O at 323.15 and 348.15 K. *J. Chem. Eng. Data* **2014**, *59*, 2177–2185. [[CrossRef](#)]
19. Chou, I.-M.; Seal, R.R. Magnesium and calcium sulfate stabilities and the water budget of Mars. *J. Geophys. Res.* **2007**, *112*, 96. [[CrossRef](#)]
20. Dongdong, L.; Dandan, G.; Yaping, D.; Wu, L. Modeling of phase relations and thermodynamics in the Mg(OH)₂ + MgSO₄ + H₂O system with implications on magnesium hydroxide sulfate cement. *Calphad* **2019**, *67*, 101675. [[CrossRef](#)]
21. Zhang, Y.; Asselin, E.; Li, Z. Solubility Measurement and Chemical Modeling of MgSO₄·7H₂O in the Ti(SO₄)₂-H₂SO₄-H₂O System. *J. Chem. Eng. Data* **2016**, *61*, 2363–2370. [[CrossRef](#)]
22. Robson, H.L. The System MgSO₄-H₂O from 68 TO 240°1. *J. Am. Chem. Soc.* **1927**, *49*, 2772–2783. [[CrossRef](#)]
23. Apelblat, A.; Manzurola, E. Solubilities and vapour pressures of saturated aqueous solutions of sodium tetraborate, sodium carbonate, and magnesium sulfate at freezing-temperature lowerings of sodium tetraborate and sodium carbonate solutions. *J. Chem. Thermodyn.* **2003**, *35*, 221–238. [[CrossRef](#)]
24. Ting, H.H.; McCabe, W.L. Solubility of Magnesium Sulfate Heptahydrate. *Ind. Eng. Chem.* **1934**, *26*, 1207–1208. [[CrossRef](#)]
25. Wu, X.; Wang, K.; Xiong, Z.; Ye, X. Solubility of α-Calcium Sulfate Hemihydrate in Ca-Mg-K Chloride Salt Solution at (353.0 to 371.0) K. *J. Chem. Eng. Data* **2013**, *58*, 48–54. [[CrossRef](#)]
26. Yang, L.; Guan, B.; Wu, Z.; Ma, X. Solubility and Phase Transitions of Calcium Sulfate in KCl Solutions between 85 and 100 °C. *Ind. Eng. Chem. Res.* **2009**, *48*, 7773–7779. [[CrossRef](#)]
27. Shen, L.; Sippola, H.; Li, X.; Lindberg, D.; Taskinen, P. Thermodynamic Modeling of Calcium Sulfate Hydrates in the CaSO₄-H₂O System from 273.15 to 473.15 K with Extension to 548.15 K. *J. Chem. Eng. Data* **2019**, *64*, 2697–2709. [[CrossRef](#)]
28. Partridge, E.P.; White, A.H. The solubility of calcium sulfate from 0 to 200°. *J. Am. Chem. Soc.* **1929**, *51*, 360–370. [[CrossRef](#)]
29. Li, Z.; Demopoulos, G.P. Solubility of CaSO₄ Phases in Aqueous HCl + CaCl₂ Solutions from 283 K to 353 K. *J. Chem. Eng. Data* **2005**, *50*, 1971–1982. [[CrossRef](#)]
30. Wang, W.; Zeng, D.; Chen, Q.; Yin, X. Experimental determination and modeling of gypsum and insoluble anhydrite solubility in the system CaSO₄-H₂SO₄-H₂O. *Chem. Eng. Sci.* **2013**, *101*, 120–129. [[CrossRef](#)]
31. Hulett, G.A.; Allen, L.E. The solubility of gypsum. *J. Am. Chem. Soc.* **1902**, *24*, 667–679. [[CrossRef](#)]
32. Yuan, T.; Wang, J.; Li, Z. Measurement and modelling of solubility for calcium sulfate dihydrate and calcium hydroxide in NaOH/KOH solutions. *Fluid Phase Equilibria* **2010**, *297*, 129–137. [[CrossRef](#)]
33. Power, W.H.; Fabuss, B.M. Transient Solubilities in the Calcium Sulfate-Water System. *J. Chem. Eng. Data* **1964**, *9*, 437–442. [[CrossRef](#)]
34. Templeton, C.C.; Rodgers, J.C. Solubility of anhydrite in several aqueous salt solutions between 250.degree. and 325.degree. *J. Chem. Eng. Data* **1967**, *12*, 536–547. [[CrossRef](#)]
35. Scholz, F.; Kahlert, H. The calculation of the solubility of metal hydroxides, oxide-hydroxides, and oxides, and their visualisation in logarithmic diagrams. *ChemTexts* **2015**, *1*, 7. [[CrossRef](#)]
36. Busch, W. Über die Verwendbarkeit der elektrometrischen Titration zur Löslichkeitsbestimmung schwerlöslicher Oxyde. *Z. Anorg. Allg. Chem.* **1927**, *161*, 161–179. [[CrossRef](#)]
37. Hostetler, P.B. The stability and surface energy of brucite in water at 25 degrees C. *Am. J. Sci.* **1963**, *261*, 238–258. [[CrossRef](#)]

38. Remy, H.; Kuhlmann, A. Löslichkeitsbestimmungen an schwer löslichen Stoffen. II. Wasserlöslichkeit der Oxyde von Beryllium, Aluminium, Zink, Cadmium, Blei, Kupfer und Silber. *Anal. Bioanal. Chem.* **1924**, *65*, 161–181. [[CrossRef](#)]
39. Dupré; Bialas, J. Zur Bestimmung der Löslichkeit von Magnesia und Zinkoxyd in Wasser auf Grund des elektrischen Leitvermögens. *Angew. Chem.* **1903**, *16*, 54–55. [[CrossRef](#)]
40. Whipple, G.C.; Mayer, A. The Solubility of Calcium Carbonate and of Magnesium Hydroxide and the Precipitation of These Salts with Lime Water. *J. Infect. Dis.* **1906**, *3*, S151–S165. [[CrossRef](#)]
41. Einaga, H. The hydrolytic precipitation reaction of Mg(II) from aqueous NaNO₃ solution. *J. Inorg. Nucl. Chem.* **1981**, *43*, 229–233. [[CrossRef](#)]
42. McGee, K.A.; Hostetler, P.B. Activity-product constant of brucite from 10 °C to 90 °C. *J. Res. US Geol. Surv.* **1977**, 227–233.
43. Bassett, H.; Taylor, H.S. CLXXX.—Calcium nitrate. Part III. The three-component system: Calcium nitrate–lime–water. *J. Chem. Soc. Trans.* **1914**, *105*, 1926–1941. [[CrossRef](#)]
44. Yeatts, L.B.; Marshall, W.L. Aqueous systems at high temperature. XVIII. Activity coefficient behavior of calcium hydroxide in aqueous sodium nitrate to the critical temperature of water. *J. Phys. Chem.* **1967**, *71*, 2641–2650. [[CrossRef](#)]
45. Bates, R.G.; Bower, V.E.; Smith, E.R. Calcium hydroxide as a highly alkaline pH standard. *J. Res. Natl. Inst. Stand.* **1956**, *56*, 305. [[CrossRef](#)]
46. Cameron, F.K.; Robinson, W.O. The System, Lime, Nitric Acid and Water. *J. Phys. Chem.* **1907**, *11*, 273–278. [[CrossRef](#)]

Journal Paper II

Assessment of Modeling the MgO-CaO-CO₂-SO₂-H₂O-O₂ System Using the Electrolyte NRTL Activity Coefficient Model

Barbara D. Weiß, Bahram Haddadi,* and Michael Harasek



Cite This: *Ind. Eng. Chem. Res.* 2023, 62, 12626–12639



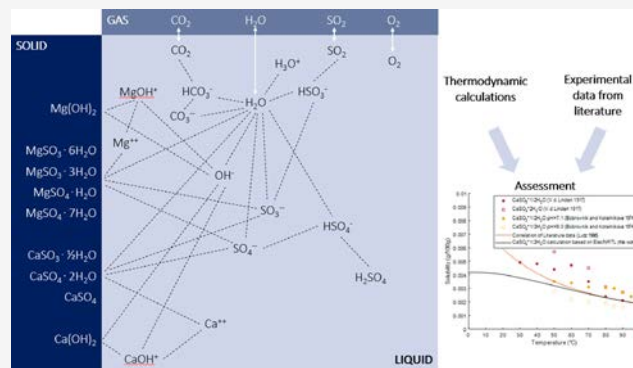
Read Online

ACCESS |

Metrics & More

Article Recommendations

ABSTRACT: This work assesses the thermodynamic modeling of the MgO-CaO-CO₂-SO₂-H₂O-O₂ system using the electrolyte NRTL activity coefficient model, primarily focusing on the solubility of potential salts in the system. The assessment includes the SO₂-H₂O and SO₂-Mg(OH)₂ vapor-liquid equilibria as well as the precipitation of Mg(OH)₂, Ca(OH)₂, MgSO₃, CaSO₃, MgSO₄, CaSO₄, and their hydrate forms. The analysis covers a temperature range of 0 to 100 °C and focuses on calculations at atmospheric pressure. The performed calculations assess the necessity of defining equilibrium constants K_{eq} as a function of temperature to describe the chemical equilibria accurately. The SO₂ solubility in water is studied for a pressure range of 0.545 to 1.788 bar. The SO₂-Mg(OH)₂ absorption equilibrium is studied for a SO₂ partial pressure range of 0.00963 to 1.101325 bar and a MgO concentration of up to 14.5 kg/m³ H₂O. The results are evaluated using experimentally determined data from the literature. The study shows that the model recognizes all reported precipitation forms in the correct temperature range in chemically stable systems. The solubility of Mg(OH)₂ is calculated with a deviation from literature data of <6% for a temperature range of 70 to 90 °C and a maximum deviation of -40% for temperatures close to 0 °C. The calculated Ca(OH)₂ solubility at the complete studied temperature range deviates less than 11% from the literature data. The model also recognizes the pH dependency of the solubility of both hydroxides. The calculated solubility of MgSO₃ hexahydrate deviates less than 1% from literature data, and the calculated solubility of MgSO₃ trihydrate shows a maximum deviation from literature data of 20% at temperatures up to 90 °C. The solubility of CaSO₃ hemihydrate is predicted with a deviation of <1% at a temperature range of 70 to 100 °C and a deviation of <30% for temperatures higher than 20 °C. The model predicts the solubility of MgSO₄ monohydrate with a maximum deviation from literature data of 20% and overestimates the solubility of MgSO₄ heptahydrate by up to 118% compared to literature data. The solubility of CaSO₄ monohydrate is calculated with a deviation from literature data of <2%, and the solubility of CaSO₄ dihydrate with a deviation of <7%. The model's accuracy in predicting the SO₂ solubility in water varies strongly depending on which literature data points it is compared to. The smallest deviation from literature data is 1% compared to data measured at 60 °C and a pressure of 1.377 bar. The highest deviation is 60% compared to data measured at 90 °C and atmospheric pressure. The study shows that the experimental data in literature describing the SO₂ absorption in an Mg(OH)₂ solution are scarce. This leads to a limited ability to evaluate thermodynamic models based on experimental data. The model describes the SO₂ absorption in Mg(OH)₂ with a deviation between 8 and 52% compared to available literature data.



1. INTRODUCTION

The MgO-CaO-CO₂-SO₂-H₂O-O₂ system is an important electrolyte system for flue gas treatment processes, where SO₂ is removed from the gas by absorption. It has particular importance in the pulp and paper industry, as the absorption of SO₂ using Mg(OH)₂ slurry allows the recovery of magnesium bisulfite, which then can be used as cooking liquor for pulp production again. The absorption of SO₂ using magnesium hydroxide slurry has recently gained increased attention due to the possibility of removing pollutants SO₂ and NO_x simultaneously.¹ Complex industrial absorption processes often have up to 10 absorption steps. To run the process in an optimized

way, mechanistic models are of great importance. A mechanistic model allows a deeper understanding of the complex electrolyte system and the detection of critical zones in the process chain. A mechanistic model combined with process control data of a

Received: March 16, 2023

Revised: July 14, 2023

Accepted: July 20, 2023

Published: August 2, 2023



plant can provide a digital twin of the plant, which can be used to find optimized process parameters or to control the process.

The MgO-CaO-CO₂-SO₂-H₂O-O₂ system is prone to precipitation in the system. While in some processes, precipitation is wanted to separate the solids from the liquid, in the chemical recovery of the pulp industry, precipitation is highly undesired. Uncontrolled precipitation causes the blockage of pipes and consequential chemical loss.² Whether the precipitation is desired or avoided, a rigorous thermodynamic model can serve as a valuable tool to identify precipitation in the system. The occurrence of precipitation depends on the complex present electrolyte system. Therefore, a mechanistic model needs to cover all relevant reactions of that system.

The electrolyte NRTL model is a commonly used method to model electrolyte systems. Si et al. applied the electrolyte NRTL method to an SO₂ absorption system based on calcium.³ Schögl et al. described the MgO-H₂O-SO₂ system using the electrolyte NRTL method.⁴ Their study indicates that the method is applicable to model that system. However, the study also suggests improving the model by adapting the calculation results to literature data through an external function that overwrites the calculation results with input data. Zidar et al. modeled the MgO-H₂O-SO₂ equilibrium using the Rudzinski+Pitzer-Ion activity coefficient model.⁵ They used the Pitzer's ion interaction model to calculate the activity coefficients in the mixture and the Rudzinski method to determine the pH value. While there are earlier studies available building up to the results of Zidar et al.,⁶ there are no newer studies found in literature that target the topic of thermodynamic modeling of the absorption system. The lack of available studies motivated the authors to conduct a comprehensive assessment of the applicability of the semi-empirical electrolyte NRTL method to model the absorption equilibrium as well as precipitations in the system. This study evaluates the applicability of the electrolyte NRTL method to model the SO₂ absorption using up-to-date available thermodynamic property data and the solubility of all potential salts in the system. The calculated results are compared to available experimental data from the literature.

2. METHODS

The system was rigorously modeled using the simulation environment and data banks of Aspen Plus V10. The electrolyte system is described using the true component approach. The true component approach, unlike the apparent component approach, means that all true components of the electrolyte system, including ions, salts, and molecular species, are reported. The results were evaluated using literature data reviewed in a previous study.⁷ The following summarizes the applied methodology.

2.1. Thermodynamic Framework. The electrolyte NRTL activity coefficient model was applied as proposed by Chen and Evans and extended by Mock et al.^{8,9} The vapor phase properties were calculated using the Redlich–Kwong equation of state.¹⁰

The system was calculated in phase equilibrium. The equality of the fugacity of every component in the different present phases is the basis of the performed key thermodynamic property calculations:

$$f_i^v = f_i^l \quad (1)$$

2.1.1. Vapor Phase Properties—Redlich–Kwong Equation of State. The fugacity of the vapor phase is expressed as follows:

$$f_i^v = \varphi_i^v y_i p \quad (2)$$

The fugacity coefficients are represented by

$$\ln \varphi_i^v = -\frac{1}{RT} \int_{\infty}^{V^v} \left[\left(\frac{\partial p}{\partial n_i} \right)_{T,V,n_{j \neq i}} - \frac{R}{TV} \right] dV - \ln Z_m^v \quad (3)$$

with

$$Z_m^v = \frac{pV}{nRT} \quad (4)$$

The vapor phase properties are calculated by the cubic equation of state Redlich–Kwong:¹⁰

$$p = \frac{RT}{V_m - b} - \frac{a}{V_m(V_m + b)} \quad (5)$$

$$\sqrt{a} = \sum_i y_i \sqrt{a_i} \quad (6)$$

$$b = \sum_i y_i b_i \quad (7)$$

$$a_i = 0.42748023 \frac{R^2 T_{ci}^{2.5}}{p_{ci}} \quad (8)$$

$$b_i = 0.08664 \frac{RT_{ci}}{p_{ci}} \quad (9)$$

The critical temperature and the critical pressure of the pure components were retrieved from the standard implemented data banks in Aspen Plus V10.

2.1.2. Liquid Phase Properties—Electrolyte NRTL Activity Coefficient Model. The fugacity of the liquid phase is expressed as follows:

$$f_i^l = f_i^{*,l} x_i \gamma_i \quad (10)$$

$$f_i^{*,l} = F_{p,i}^* \varphi_i^* p_i^* \quad (11)$$

$$F_{p,i}^* = e^{1/RT \int_{p_i^*}^p V_{mi}^{*,l} dp} \quad (12)$$

The activity coefficient represents the deviation of the mixture from ideality. The reference state defines which state is referred to as ideal. In other words, the reference state dictates the conditions at which the activity coefficient is assigned to the value of 1.¹¹ The properties of the reference state are denoted by *. For supercritical components (CO₂, O₂, and SO₂) and ions, the model was calculated using an unsymmetric reference state, which means that the reference state is at infinite dilution at system temperature and pressure:

$$\gamma_i^* = \frac{\gamma_i}{\gamma_i^\infty} \quad (13)$$

The basis for the unsymmetric activity coefficient is the actual mixed solvent present. For all other components, the reference state is that of a pure compound. The liquid phase reference fugacity is then defined as that of the pure liquid component *i* at system temperature and pressure.

The behavior of dissolved gases, such as CO₂, O₂, and SO₂, is represented using Henry's law. The expression of the fugacity of the liquid phase becomes the following:

$$f_i^l = H_i x_i \gamma_i^* \quad (14)$$

The temperature-dependent Henry's constants were retrieved from the standard implemented data banks in Aspen Plus V10. Table 1 gives the applied $\ln(H)$ exemplary for 70 °C.

Table 1. Applied Henry's Constants Expressed as $\ln(H_{ij})$ at 70 °C

component <i>i</i>	component <i>j</i>	$\ln(H_{ij})_{T=70^\circ\text{C}}$
SO ₂	H ₂ O	4.91122046
O ₂	H ₂ O	-18.0625181
CO ₂	H ₂ O	8.26167044

The activity coefficients were calculated using the electrolyte NRTL activity coefficient model.^{8,9} The model is based on the assumptions that, due to strong repulsive forces between ions of like charge, the immediate neighbors of any ions are ions of opposite charge and that the distribution of ions results in local electroneutrality.

The model describes the excess Gibbs energy based on the following relation:

$$\ln \gamma_i = \left(\frac{\partial \left(n_{\text{total}} \frac{G^E}{RT} \right)}{\partial n_i} \right)_{T,P,n_i} \quad (15)$$

The model describes the activity coefficient with a Pitzer–Debye–Hückel (PDH) and a Born (Born) expression for long-

range electrostatic interactions and an NRTL-local composition contribution (lc) for the short-range interactions:

$$\ln \gamma_i = \ln \gamma_i^{\text{PDH}} + \ln \gamma_i^{\text{Born}} + \ln \gamma_i^{\text{lc}} \quad (16)$$

$$\ln \gamma_i^{\text{PDH}} = -\sqrt{\frac{1000}{M_s}} A_\varphi \left[\left(\frac{2z_i^2}{\rho} \right) \ln(1 + \rho\sqrt{I_x}) + \frac{z_i^2 \sqrt{I_x} - 2\sqrt{I_x^3}}{1 + \rho\sqrt{I_x}} \right] \quad (17)$$

$$A_\varphi = \frac{1}{3} \sqrt{\frac{2\pi N_A d_s}{1000}} \sqrt{\frac{Q_e^2}{\epsilon_s kT}} \quad (18)$$

$$I_x = \frac{1}{2} \sum x_i z_i^2 \quad (19)$$

$$\ln \gamma_i^{\text{Born}} = \frac{Q_e^2}{2kT} \left(\frac{1}{\epsilon_s} - \frac{1}{\epsilon_w} \right) \frac{z_i^2}{r_i} 10^{-2} \quad (20)$$

$$\ln \gamma_i^{\text{lc}} = \frac{\sum_j x_j \tau_{ji} G_{ji}}{\sum_k x_k G_{ki}} + \sum_j \frac{x_j G_{ji}}{\sum_k x_k G_{kj}} \left(\tau_{ji} - \frac{\sum_m x_m \tau_{mj} G_{mj}}{\sum_k x_k G_{kj}} \right) \quad (21)$$

$$G_{ij} = e^{-\alpha_{ij} \tau_{ij}} \quad (22)$$

$$\tau_{ij} = a_{ij} + \frac{b_{ij}}{T} + e_{ij} \ln(T) + f_{ij} T \quad (23)$$

Table 2. Considered Electrolyte System

reaction	type
2 H ₂ O ↔ OH ⁻ + H ₃ O ⁺	partial dissociation equilibrium
2 H ₂ O + SO ₂ ↔ H ₃ O ⁺ + HSO ₃ ⁻	partial dissociation equilibrium
H ₂ O + HSO ₃ ⁻ ↔ H ₃ O ⁺ + SO ₃ ²⁻	partial dissociation equilibrium
H ₂ SO ₄ + H ₂ O ↔ H ₃ O ⁺ + HSO ₄ ⁻	partial dissociation equilibrium
H ₂ O + HSO ₄ ⁻ ↔ H ₃ O ⁺ + SO ₄ ²⁻	partial dissociation equilibrium
MgOH ⁺ ↔ OH ⁻ + Mg ²⁺	partial dissociation equilibrium
CaOH ⁺ ↔ OH ⁻ + Ca ²⁺	partial dissociation equilibrium
2 H ₂ O + CO ₂ ↔ H ₃ O ⁺ + HCO ₃ ⁻	partial dissociation equilibrium
H ₂ O + HCO ₃ ⁻ ↔ H ₃ O ⁺ + CO ₃ ²⁻	partial dissociation equilibrium
Mg(OH) ₂ → OH ⁻ + MgOH ⁺	complete dissociation
Ca(OH) ₂ → OH ⁻ + CaOH ⁺	complete dissociation
MgSO ₄ → Mg ²⁺ + SO ₄ ²⁻	complete dissociation
MgSO ₃ → Mg ²⁺ + SO ₃ ²⁻	complete dissociation
CaSO ₄ → Ca ²⁺ + SO ₄ ²⁻	complete dissociation
CaSO ₃ → Ca ²⁺ + SO ₃ ²⁻	complete dissociation
MgCO ₃ → Mg ²⁺ + CO ₃ ²⁻	complete dissociation
CaCO ₃ → Ca ²⁺ + CO ₃ ²⁻	complete dissociation
Mg(OH) ₂ (s) ↔ OH ⁻ + MgOH ⁺	salt precipitation equilibrium
Ca(OH) ₂ (s) ↔ OH ⁻ + CaOH ⁺	salt precipitation equilibrium
MgSO ₃ * 6 H ₂ O (solid) ↔ Mg ²⁺ + SO ₃ ²⁻ + 6 H ₂ O (aqueous)	salt precipitation equilibrium
MgSO ₃ * 3 H ₂ O (solid) ↔ Mg ²⁺ + SO ₃ ²⁻ + 3 H ₂ O (aqueous)	salt precipitation equilibrium
CaSO ₃ * 1/2 H ₂ O (solid) ↔ Ca ²⁺ + SO ₃ ²⁻ + 1/2 H ₂ O (aqueous)	salt precipitation equilibrium
MgSO ₄ * H ₂ O (solid) ↔ Mg ²⁺ + SO ₄ ²⁻ + 1 H ₂ O (aqueous)	salt precipitation equilibrium
MgSO ₄ * 7 H ₂ O (solid) ↔ Mg ²⁺ + SO ₄ ²⁻ + 7 H ₂ O (aqueous)	salt precipitation equilibrium
CaSO ₄ * 2 H ₂ O (solid) ↔ Ca ²⁺ + SO ₄ ²⁻ + 2 H ₂ O (aqueous)	salt precipitation equilibrium
CaSO ₄ (solid) ↔ Ca ²⁺ + SO ₄ ²⁻ (aqueous)	salt precipitation equilibrium

Table 3. Applied Equilibrium Constants Expressed as $\ln(K_{\text{eq}})$ at 70 °C

reaction	$\ln(K)_{T=70^\circ\text{C}}$
$2 \text{H}_2\text{O} \leftrightarrow \text{OH}^- + \text{H}_3\text{O}^+$	-37.510985
$2 \text{H}_2\text{O} + \text{SO}_2 \leftrightarrow \text{H}_3\text{O}^+ + \text{HSO}_3^-$	-9.31441704
$\text{H}_2\text{O} + \text{HSO}_3^- \leftrightarrow \text{H}_3\text{O}^+ + \text{SO}_3^{--}$	-21.4048358
$\text{MgSO}_3 \cdot 6 \text{H}_2\text{O} (\text{solid}) \leftrightarrow \text{Mg}^{++} + \text{SO}_3^{--} + 6 \text{H}_2\text{O} (\text{aqueous})$	-15.6969191
$\text{MgSO}_3 \cdot 3 \text{H}_2\text{O} (\text{solid}) \leftrightarrow \text{Mg}^{++} + \text{SO}_3^{--} + 3 \text{H}_2\text{O} (\text{aqueous})$	-16.7808349
$\text{MgSO}_4 \cdot \text{H}_2\text{O} (\text{solid}) \leftrightarrow \text{Mg}^{++} + \text{SO}_4^{--} + 1 \text{H}_2\text{O} (\text{aqueous})$	-12.3224139
$\text{MgSO}_4 \cdot 7 \text{H}_2\text{O} (\text{solid}) \leftrightarrow \text{Mg}^{++} + \text{SO}_4^{--} + 7 \text{H}_2\text{O} (\text{aqueous})$	-13.1206858
$\text{CaSO}_4 \cdot 2 \text{H}_2\text{O} (\text{solid}) \leftrightarrow \text{Ca}^{++} + \text{SO}_4^{--} + 2 \text{H}_2\text{O} (\text{aqueous})$	-18.4221215

$$\alpha_{ij} = c_{ij} + d_{ij}(T - 273.15K) \quad (24)$$

The adjustable parameters—born radius, the dielectric constant coefficients, and the binary interaction parameters—were retrieved from the standard implemented data banks in Aspen Plus V10.

2.1.3. Chemical System. The model includes partial dissociation equilibrium reactions, complete dissociations reactions, and salt precipitation equilibrium reactions. Table 2 summarizes all considered reactions.

The chemical equilibrium is calculated using built-in or user-supplied parameters to describe the equilibrium constants K_{eq} as a function of temperature. If no equilibrium constants are given, the equilibrium is calculated from the reference state Gibbs free energies of the participating components following:

$$\ln(K) = \frac{\Delta G_{\text{m}}^*}{RT} \quad (25)$$

The applied parameters to describe the temperature-dependent equilibrium constants are retrieved from the Aspen Plus V10 data bank. Table 3 gives the applied $\ln(K)$ exemplary for 70 °C.

2.2. Performed Analyses for Assessment. To assess the accuracy of the thermodynamic calculations, the calculated properties were compared with experimental data retrieved from the literature. The deviation of the calculated value from literature data is given as

$$\text{deviation (\%)} = \frac{(x_{\text{calculated}} - x_{\text{literature}})}{x_{\text{literature}}} \times 100 \quad (26)$$

The following summarizes the performed calculations and the referenced literature data.

2.2.1. Solubility of SO_2 . The solubility of SO_2 in water was calculated following two different approaches. First, it was calculated solely using Henry's Law without any electrolyte reactions. Then, it was calculated considering electrolyte reactions (see 2.1) to evaluate the influence of including the electrolyte equilibrium on the calculated SO_2 solubility. The solubility was calculated for a temperature range from 20 to 90 °C and a pressure range from 0.545 to 1.788 bar. The calculations were compared to experimental data from Rumpf and Maurer and Young et al.^{12,13}

2.2.2. SO_2 Absorption in $\text{Mg}(\text{OH})_2$ Solution. The SO_2 absorbed in $\text{Mg}(\text{OH})_2$ - H_2O solution was calculated considering all electrolyte reactions given in 2.1. The calculation was performed to be comparable to available experimental literature data. In the experimental data, the temperatures range from 24 to 29.85 °C and the SO_2 partial pressures from 0.0095 to 0.888 atm. The MgO concentration in water ranges from 0 to 14.5 kg/ m^3 . The quantitative effect of the presence of $\text{Mg}(\text{OH})_2$ on the solubility of SO_2 is expressed as enhancement factor. The enhancement factor describes the increase in solubility of SO_2

when $\text{Mg}(\text{OH})_2$ is present in the solution compared to the solubility in pure water. The calculations were compared to experimental data from Mondal and Young et al.^{13,14}

2.2.3. Solubility of $\text{Mg}(\text{OH})_2$ and $\text{Ca}(\text{OH})_2$. Two dissociation reactions describe the solubility of the hydroxides: the dissociation of $\text{Mg}(\text{OH})_2$ or $\text{Ca}(\text{OH})_2$ and the formation of the ion pair MgOH^+ or CaOH^+ . This makes the solubility of the hydroxides strongly pH-dependent. This dependency is better described by calculating the equilibrium from the reference state Gibbs free energies of the participating components rather than from equilibrium constants. Therefore, the equilibrium was described by the reference state Gibbs free energy calculations. The solubility of $\text{Mg}(\text{OH})_2$ and $\text{Ca}(\text{OH})_2$ was calculated for a temperature range from 0 to 100 °C and a pH range from 7 to 13. The pH was adjusted by adding HCl to the system, as HCl does not affect the equilibrium equations of the chemical system. To evaluate the influence of modeling the formation of the MgOH^+ or CaOH^+ ion pair on the calculated solubility, the calculation was performed with and without considering its formation. The calculations were compared to experimental data from Dupré and Bialas, Remy and Kuhlmann, Busch, Whipple and Mayer, Hostetler, Einaga, Lambert and Clever, Dongdong et al., Scholz and Kahlert, Bassett and Taylor, Yeatts and Marshall, Bates et al., and Cameron and Robinson.^{15–27}

2.2.4. Solubility of MgSO_3 and CaSO_3 Hydrates. The solubility of MgSO_3 and CaSO_3 hydrates was calculated for a temperature range from 0 to 100 °C. The chemical equilibrium was first calculated by the reference state Gibbs free energy calculations and then by applying equilibrium constants (see Table 3). Literature studies report a solubility dependency of MgSO_3 and CaSO_3 hydrates on the presence of sulfate. Therefore, the influence of MgSO_4 or CaSO_4 on the solubility was calculated. The calculations were compared to experimental data from Lowell et al., Hagiwara, Markant et al., Söhnel and Rieger, Nývlt, Lutz, van der Linden, Bobrovnik and Kotelnikova, and Bichowsky.^{28–36}

2.2.5. Solubility of MgSO_4 and CaSO_4 Hydrates. The solubility of MgSO_4 and CaSO_4 hydrates was calculated for a temperature range from 0 to 100 °C. The chemical equilibrium was first calculated by the reference state Gibbs free energy calculations and then by applying equilibrium (see Table 3). The calculations were compared to experimental data from Zhang et al., Robson, Apelblat and Manzurola, Ting and McCabe, Wu et al., Patridge and White, Power and Fabuss, Wang et al., Hulett and Allen, Yuan et al., and Li and Demopoulos.^{37–47}

3. RESULTS AND DISCUSSION

The following summarizes and discusses the results of the performed calculations including the SO_2 solubility in water, the SO_2 absorption in $\text{Mg}(\text{OH})_2$, the solubility of $\text{Mg}(\text{OH})_2$ and

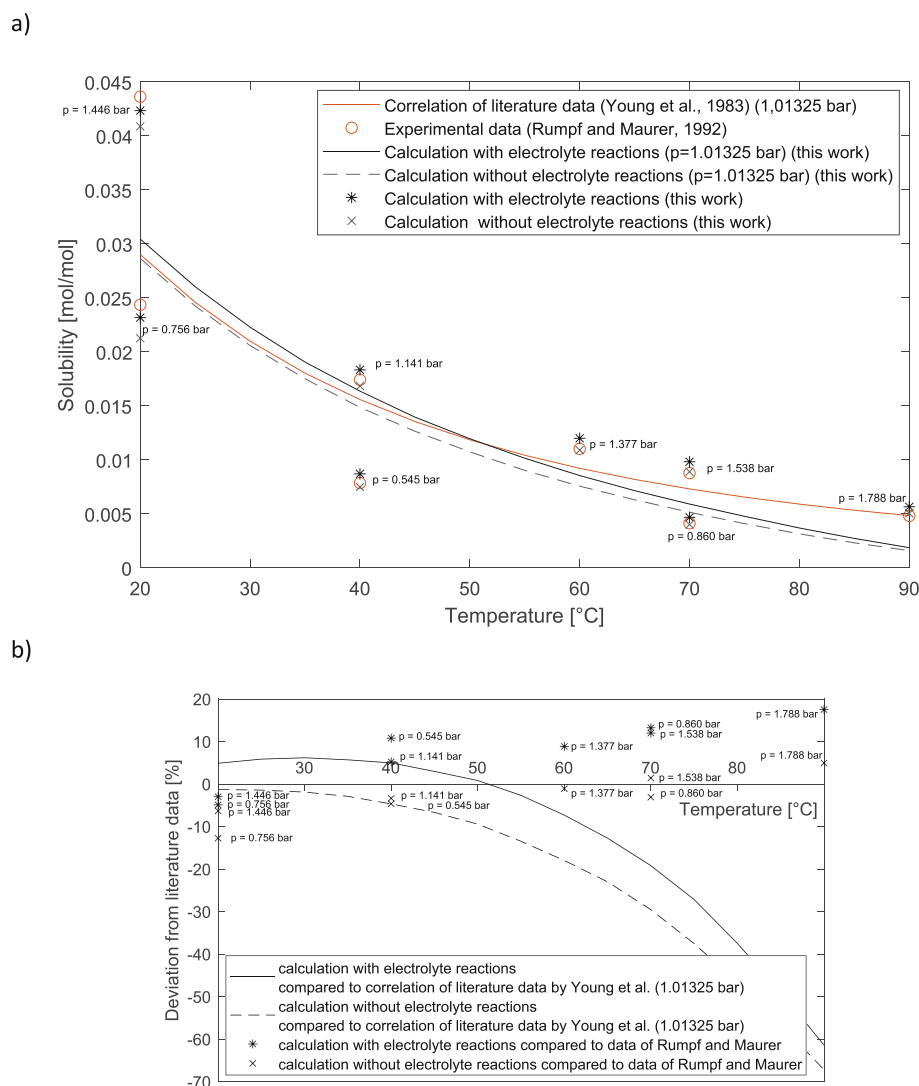


Figure 1. (a) SO_2 solubility in water over temperature at different pressures.^{12,13} (b) Deviation of calculated values from literature data (see eq 26).

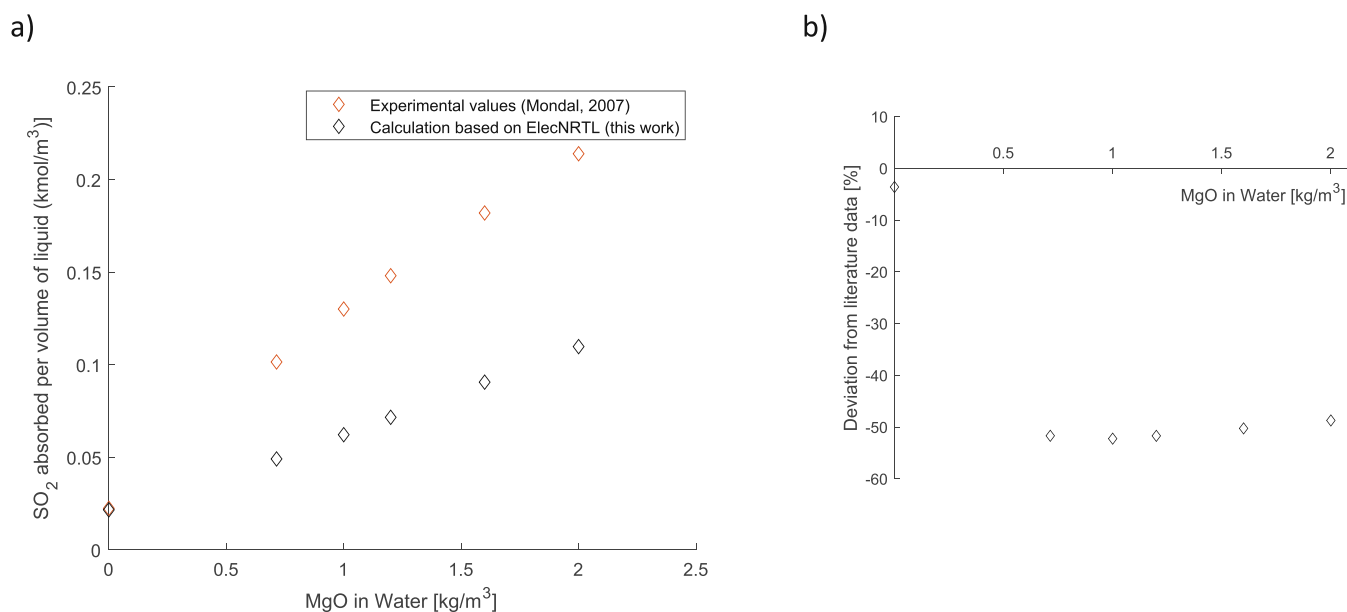


Figure 2. (a) SO_2 absorbed in $\text{Mg}(\text{OH})_2\text{-H}_2\text{O}$ solution ($T = 29.85^\circ\text{C}$, SO_2 partial pressure = 0.963 kPa).¹⁴ (b) Deviation of calculated values from literature data (see eq 26).

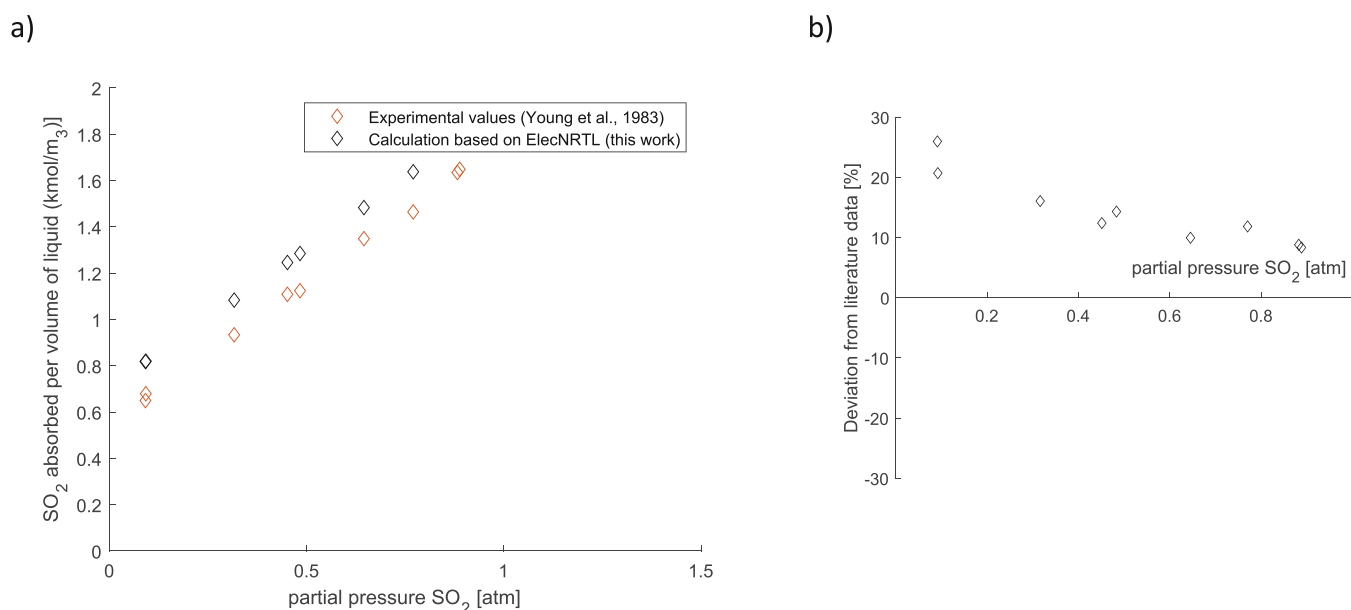


Figure 3. (a) SO₂ absorbed in Mg(OH)₂-H₂O solution ($T = 24\text{ }^{\circ}\text{C}$, MgO concentration: 14.5 kg/m³ MgO in water).¹³ (b) Deviation of calculated values from literature data (see eq 26).

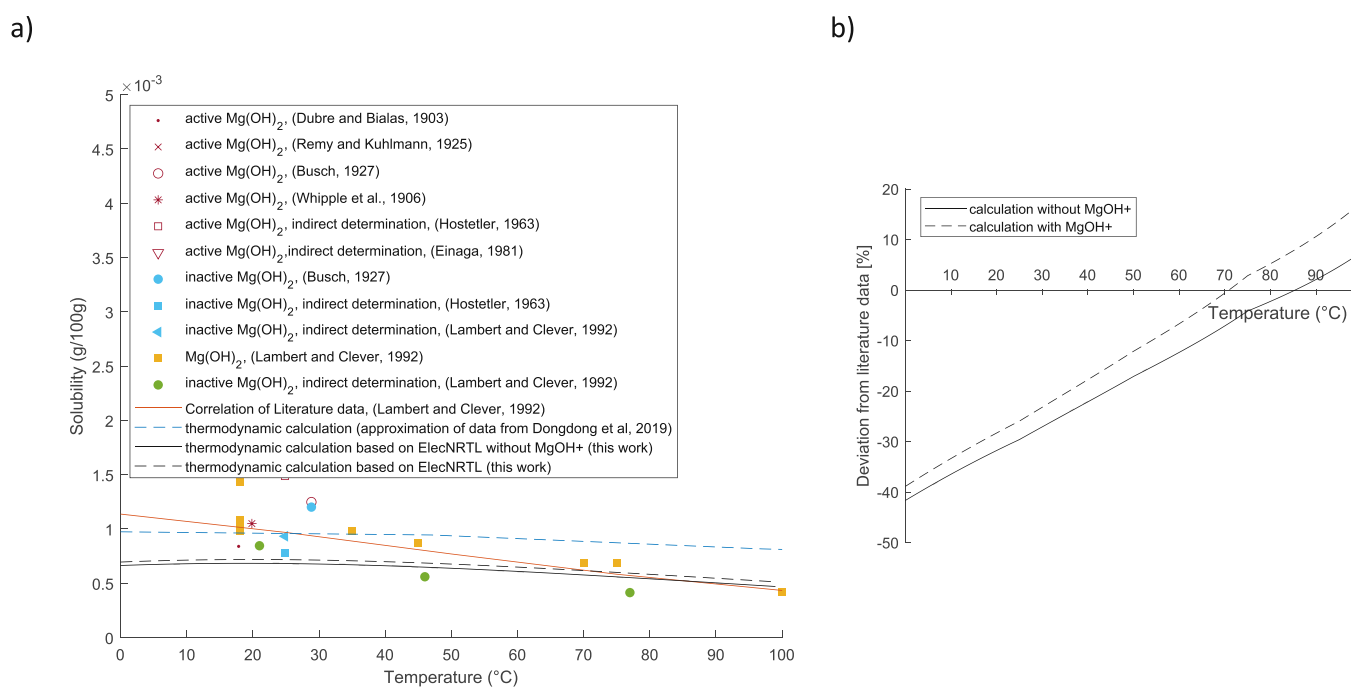


Figure 4. (a) Solubility of Mg(OH)₂ in water over temperature.^{15–22} (b) Deviation of calculated values from the correlation of literature data by Lambert and Clever (see eq 26).

Ca(OH)₂, the solubility of MgSO₃ and CaSO₃ hydrates, and the solubility of MgSO₄ and CaSO₄ hydrates.

3.1. SO₂ Solubility. 3.1.1. *SO₂ Solubility in Water.* Figure 1 shows the calculated SO₂ solubility in water compared with experimental data from the literature.

When calculating the solubility in water, the model shows, in general, a good agreement with the literature data. It is expected that electrolyte reactions increase the solubility of SO₂. This increase can also be observed when comparing the calculated results with and without considering electrolyte reactions. The calculated increase in solubility is around 6% at 20 °C and around 18% at 90 °C. Even if the calculation with the electrolyte

reactions is the more detailed approach, the performed calculations cannot justify the necessity to implement the electrolyte reactions to calculate the SO₂ solubility in water. Compared to the newer data from Rumpf and Maurer, the calculation without electrolyte reactions performs better than the calculation with electrolyte reactions at temperatures >50 °C. Compared with the IUPAC correlation of literature data, however, the calculation with electrolyte reactions performs better at temperatures >40 °C. Considering electrolyte reactions does therefore not necessarily improve the accuracy of the calculation when compared to experimental data from the literature.

3.1.2. SO₂ Absorption in Mg(OH)₂ Solution. Due to the chemical absorption, the presence of Mg(OH)₂ increases the solubility of SO₂ significantly. Figures 2 and 3 show the calculated absorbed SO₂ compared to experimental values from the literature.

The simulation results show the same trend as the experimental values found in the literature, but the absolute values show some deviation. However, the deviation is not consistent. For low MgO concentration, as studied by Mondal,¹⁴ the model underestimates the absorbed SO₂ by around 49 to 51% (Figure 2). Mondal derives an enhancement factor of 5 at a MgO concentration of 1 kg/m³. The calculation leads only to an enhancement factor of 2.5. The calculated effect of the Mg(OH)₂ on the SO₂ absorption is, therefore, only half compared to the measured effect by Mondal.

For high MgO concentrations, as studied by Young et al. and reported in the IUPAC solubility data series, the model overestimates the absorbed SO₂¹³ (Figure 3). At a low SO₂ partial pressure of 0.091 atm, the model calculates a between 20 and 26% higher absorption. At a high partial pressure of 0.888 atm, it calculates an 8% higher absorption than reported in the literature. The overestimation of the absorbed SO₂ by the model compared to the measured values could indicate that the experiment's equilibrium has not been reached. In the model calculation, it was assumed that all the MgO present in water hydrates to Mg(OH)₂ and takes part in the absorption reactions. However, reaching a total hydration rate in a real system is difficult. The overestimation by the model could also indicate that there was not a 100% hydration rate reached in the experimental setup. However, the present data do not deliver enough evidence for such theories. Furthermore, the contrary deviation for low MgO concentrations¹⁴ does not support this theory either. The available experimental data are too scarce to derive a trustful evaluation of the model in this regard. Therefore, the model was not adapted to fit one of the experimental data sets.

3.2. Solubility of Magnesium Hydroxide (Mg(OH)₂).

Figure 4 shows the calculated solubility of Mg(OH)₂ in water compared with data from the literature.

The calculated solubility shows very good agreement with the literature data. The trend of the calculated solubility is parallel to that of Dongdong et al. using the Calphad method²² but reveals lower solubility values. While at a temperature around 20 to 30 °C the model predicts a lower solubility than most experimental data, the model fits the experimental data very well in the temperature range from 70 to 90 °C with a deviation close to 0%. Furthermore, the calculation shows that including the formation of the MgOH⁺ ion pair in the calculation has little effect on the solubility of Mg(OH)₂. The model would therefore allow a simplification of the chemical system by disregarding the formation of MgOH⁺. It needs to be considered that the model describes the solubility of thermodynamic stable (inactive) Mg(OH)₂. In real systems, Mg(OH)₂ can also be present as active Mg(OH)₂. Literature data indicate that active Mg(OH)₂ has a higher solubility and that the solubility decreases with aging and the transformation to inactive Mg(OH)₂. This might be relevant for the temperature range of 20 to 30 °C. However, literature data are not definite about this decrease.²¹

Figure 5 shows the modeled pH dependency of the solubility of Mg(OH)₂ and the pH dependency given by the equation of Scholz and Kahlert.²³

The calculation shows the same trend as the trend given by Scholz and Kahlert,²³ which is the solubility drop at a specific pH

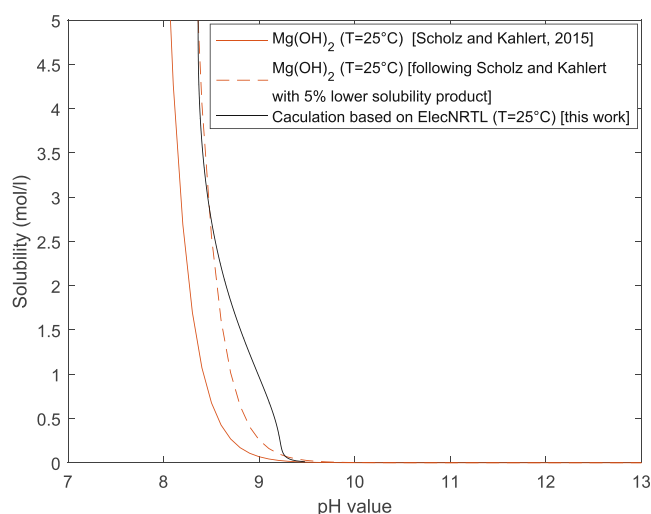


Figure 5. Solubility of Mg(OH)₂ depending on the pH value.²³

value. While Mg(OH)₂ is very soluble at a low pH value, the solubility drops rapidly between a pH of 8 and 9. According to the model, this solubility drop happens at a pH of 8.36. According to Scholz and Kahlert's calculation, it occurs at a pH of 8.1. The pH dependency given by Scholz and Kahlert is derived from an equation to calculate the solubility as a function of pH value, solubility product taken from literature, and the acid constant of water and is not derived directly from experimental data.²³ Using Scholz and Kahlert's equation with a 5% lower solubility product, the model's calculation and the calculation following Scholz and Kahlert match very well. This shows that the underlying solubility product input can be one cause for the deviation from Scholz and Kahlert's dependency.

3.3. Solubility of Calcium Hydroxide (Ca(OH)₂). Figure 6 shows the calculated solubility of Ca(OH)₂ in water compared with data from the literature.

The calculated solubility shows the same trend as the experimental data from the literature. Unlike for Mg(OH)₂, including the formation of the CaOH⁺ ion pair in the calculation shows an improving effect on the calculated solubility of Ca(OH)₂. Without considering the formation of CaOH⁺, the model underestimates the solubility by 19 to 33% compared to the correlation of Lambert and Clever.²¹ Considering the formation of CaOH⁺, the model underestimates the solubility only by around 4.5 to 11%.

Like Mg(OH)₂, the solubility of Ca(OH)₂ is strongly pH-dependent. Figure 7 shows the modeled pH dependency of the solubility of Ca(OH)₂ and the pH dependency given by the equation of Scholz and Kahlert.²³

As for Mg(OH)₂, the solubility is very high for low pH values and drops rapidly when reaching a certain pH level. The modeled solubility drop happens at a pH value of around 11.6; using Scholz and Kahlert's equation reveals a solubility drop at a pH value of 11.1.²³ As for Mg(OH)₂, one reason for this deviation between the two calculated pH dependencies can be the underlying solubility product taken from the literature. Lowering the underlying solubility product in Scholz and Kahlert's equation by 17% reveals a very good match to the model calculation.

3.4. Solubility of Magnesium Sulfite (MgSO₃). Figure 8 shows the calculated solubility of MgSO₃ hydrates in water compared with data from the literature.

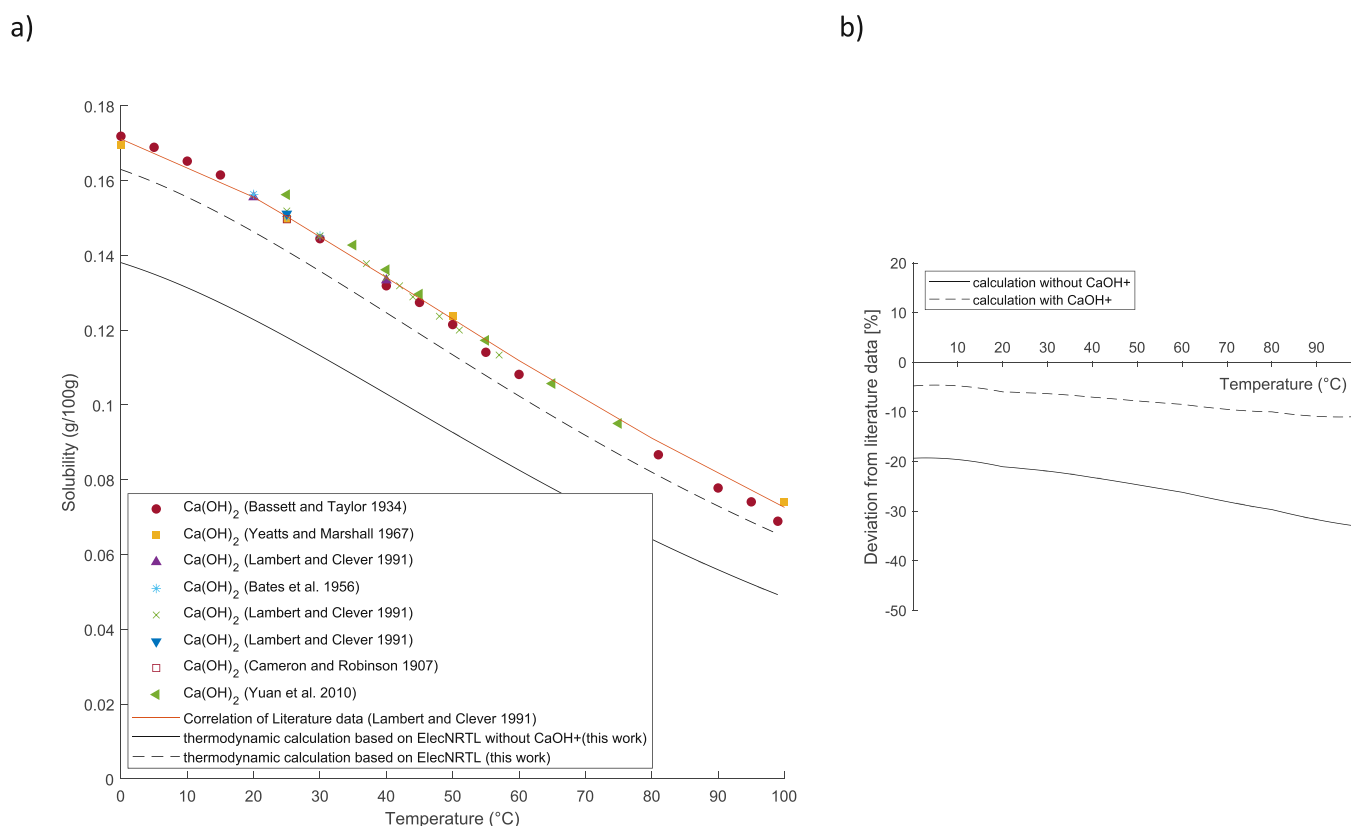


Figure 6. (a) Solubility of Ca(OH)_2 in water over temperature.^{21,24–27} (b) Deviation of calculated values from the correlation of literature data by Lambert and Clever (see eq 26).

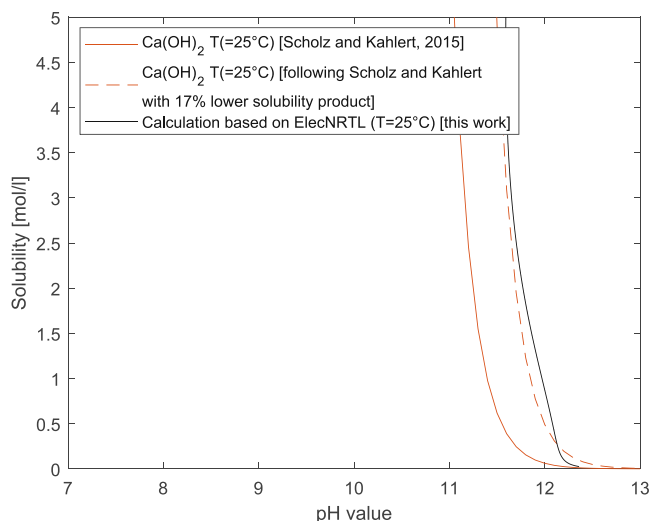


Figure 7. Solubility of Ca(OH)_2 depending on the pH value.²³

The model predicts the hexahydrate as the stable form at lower temperatures and the trihydrate as the stable form at higher temperatures. This fits with the experimental data reported in the literature. When calculating the solubility of MgSO_3 hydrates based on the reference state Gibbs free energies, the model overestimates the hexahydrate's solubility and underestimates the trihydrate's solubility compared to the experimental data. Furthermore, the model predicts the change from hexahydrate to trihydrate as the stable hydrate form at around 12 $^{\circ}\text{C}$. Following experimental data, this change happens at about 40 $^{\circ}\text{C}$. This deviation between the model and

experimental values is closed when calculating with the temperature-dependent equilibrium constants. The calculated solubility fits very well with the experimental data from the literature. When using the model to calculate a real system, it must be considered that it predicts the formation and solubility of the stable hydrate form at the given temperature. Therefore, at temperatures higher than 40 $^{\circ}\text{C}$, the model reports solely the formation of MgSO_3 trihydrate, as this is the stable form at those temperatures. However, the conversion from hexahydrate to trihydrate can be very slow in real systems. This can lead to the co-presence of meta-stable hexahydrate at temperatures above 40 $^{\circ}\text{C}$ even though trihydrate is the stable form at this temperature.^{29,31,48} The equilibrium model cannot cover the dynamic behavior of the transition from hexahydrate to trihydrate. As trihydrate has a higher solubility than hexahydrate at temperatures over 40 $^{\circ}\text{C}$, this can lead to an overestimation of precipitates in the system when modeling the system.

Figure 9 shows the calculated solubility of MgSO_3 trihydrate depending on the MgSO_4 content in the system compared to experimental data from the literature.

The model predicts the dependency of the solubility on the MgSO_4 content in the solution satisfactorily. Up to a MgSO_4 content of 10 g/100 g, the calculated solubility lies within the deviation of the available literature data. At higher MgSO_4 content, the model underestimates the solubility of the trihydrate. However, the deviation compared to the data of Lutz does not exceed 30%.

Figure 10 shows the calculated solubility of MgSO_3 hexahydrate depending on the MgSO_4 content in the system compared to experimental data from the literature.

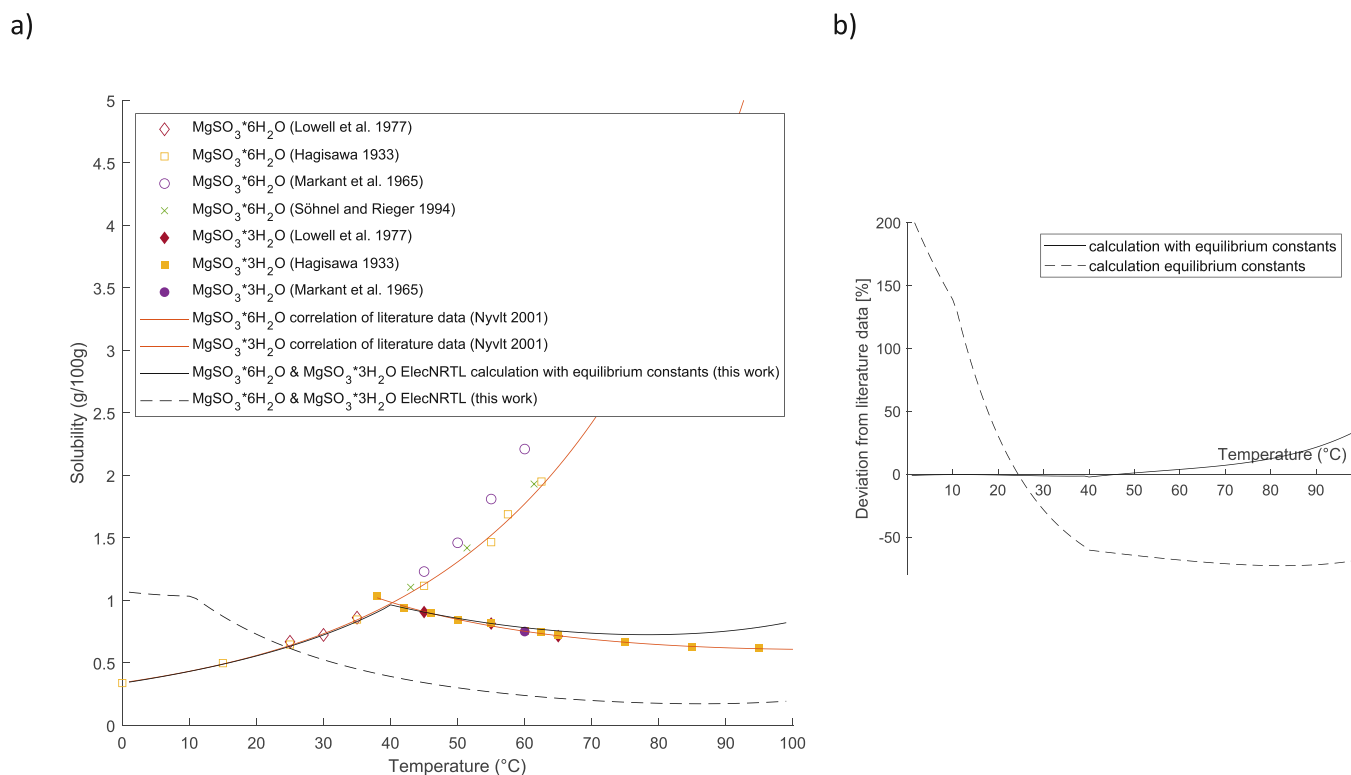


Figure 8. (a) Solubility of MgSO₃ hydrates in water over temperature.^{28–32} (b) Deviation of calculated values from the correlation of literature data by Nyvlt (see eq 26).

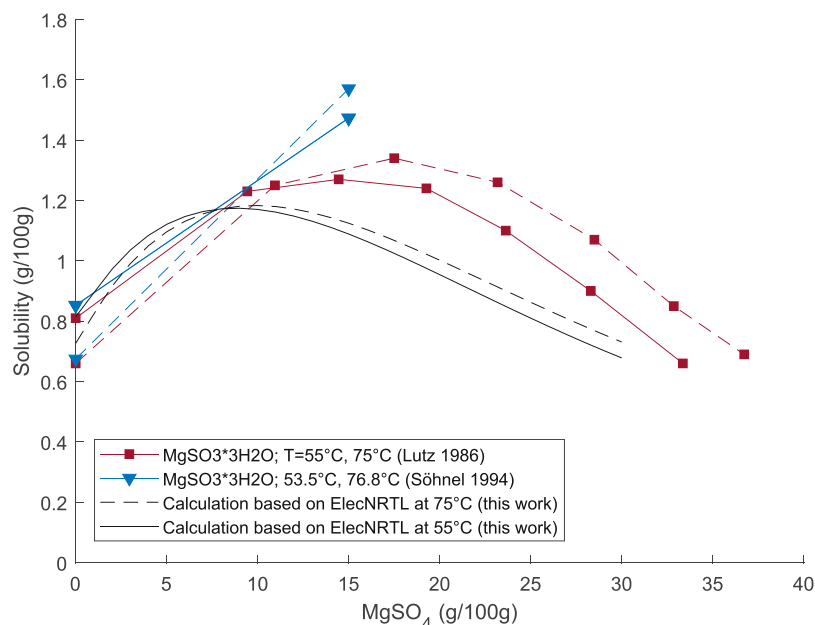


Figure 9. Solubility of MgSO₃ trihydrate over MgSO₄ content at different temperatures.^{31,33}

The calculated solubility shows a similar trend as the solubility reported in literature and lies within the deviation between the different reported experimental data. As for the trihydrate, the model tends to underestimate the solubility at high MgSO₄ contents.

3.5. Solubility of Calcium Sulfit (CaSO₃). Figure 11 shows the calculated solubility of CaSO₃ hydrates in water compared with data from the literature.

In literature, different hydrate forms of CaSO₃ are reported in the temperature range from 30 to 100 °C. However, CaSO₃ hemihydrate is recognized as the dominant one.³³ The calculated solubility of CaSO₃ hemihydrate based on the reference state Gibbs free energies shows very good agreement with the correlation of literature data done by Lutz at temperatures >50 °C with a deviation of <8%.

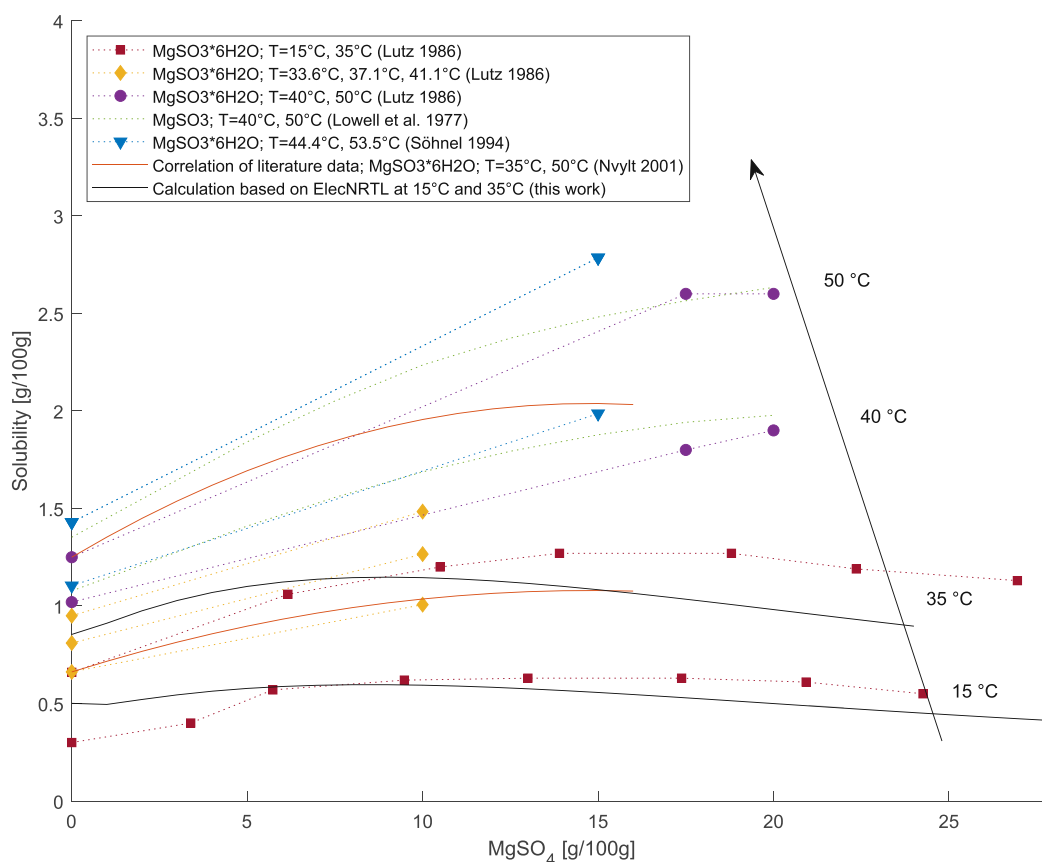
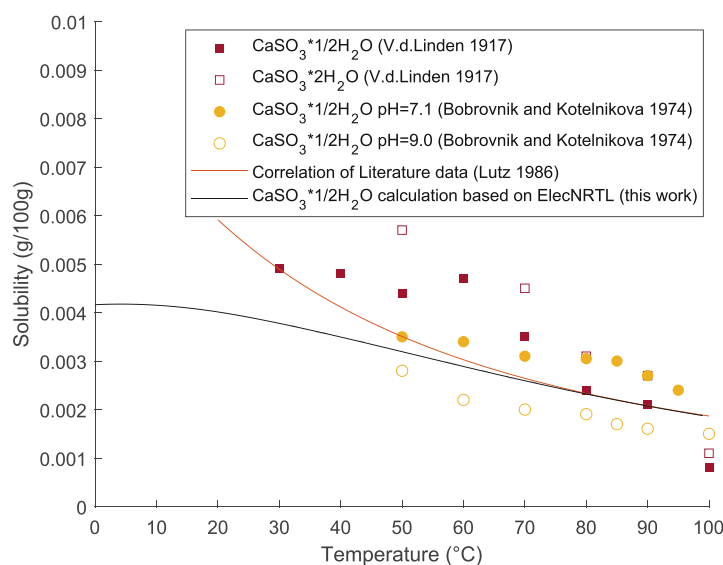


Figure 10. Solubility of MgSO_3 hexahydrate over MgSO_4 content at different temperatures.^{31–33}

a)



b)

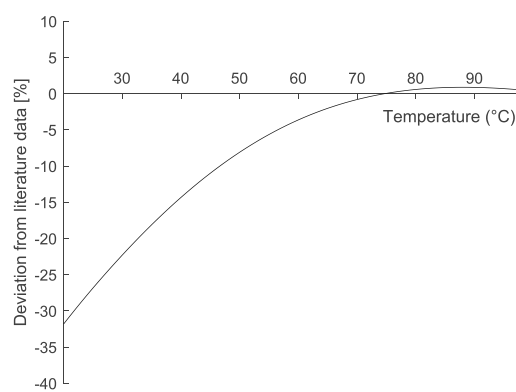


Figure 11. (a) Solubility of CaSO_3 hydrates in water over temperature.^{33–35} (b) Deviation of calculated values from the correlation of literature data by Lutz (see eq 26).

Figure 12 shows the calculated solubility of CaSO_3 hemihydrate in water and a CaSO_4 -saturated solution compared to experimental data from the literature.

The solubility of CaSO_3 hemihydrate is lower in the presence of CaSO_4 . The model describes this decrease in solubility. For temperatures ≥ 80 °C, the model fits very well with the measured

values of van der Linden. For lower temperatures, the model underestimates the solubility of CaSO_3 hemihydrate compared to the data from van der Linden and Lutz. This correlates with the findings from Figure 11, where the model also underestimates the solubility at lower temperatures. Bichowsky measures a lower solubility than van der Linden and Lutz.

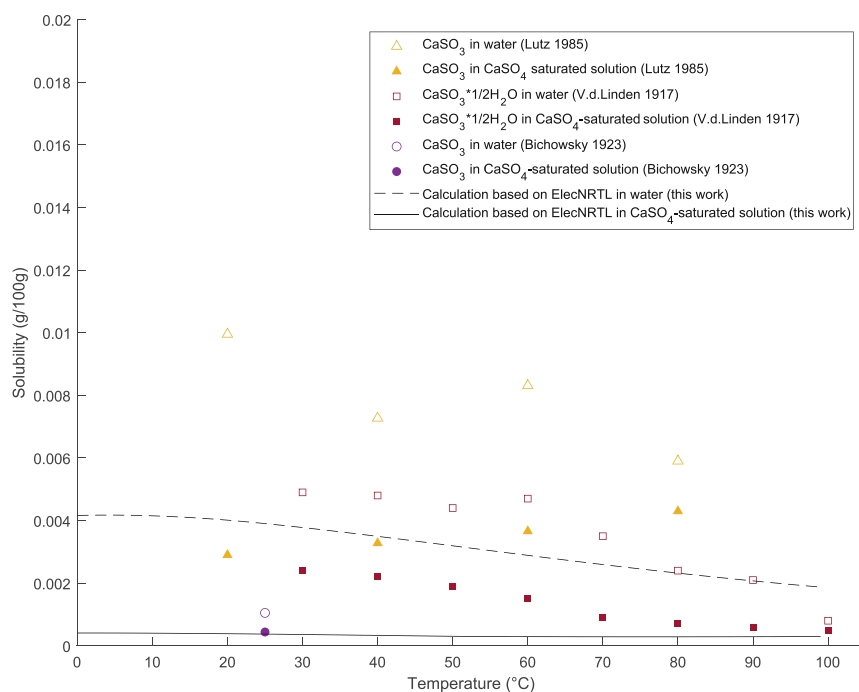


Figure 12. Solubility of CaSO_3 hydrates over CaSO_4 content at different temperatures.^{33,34,36}

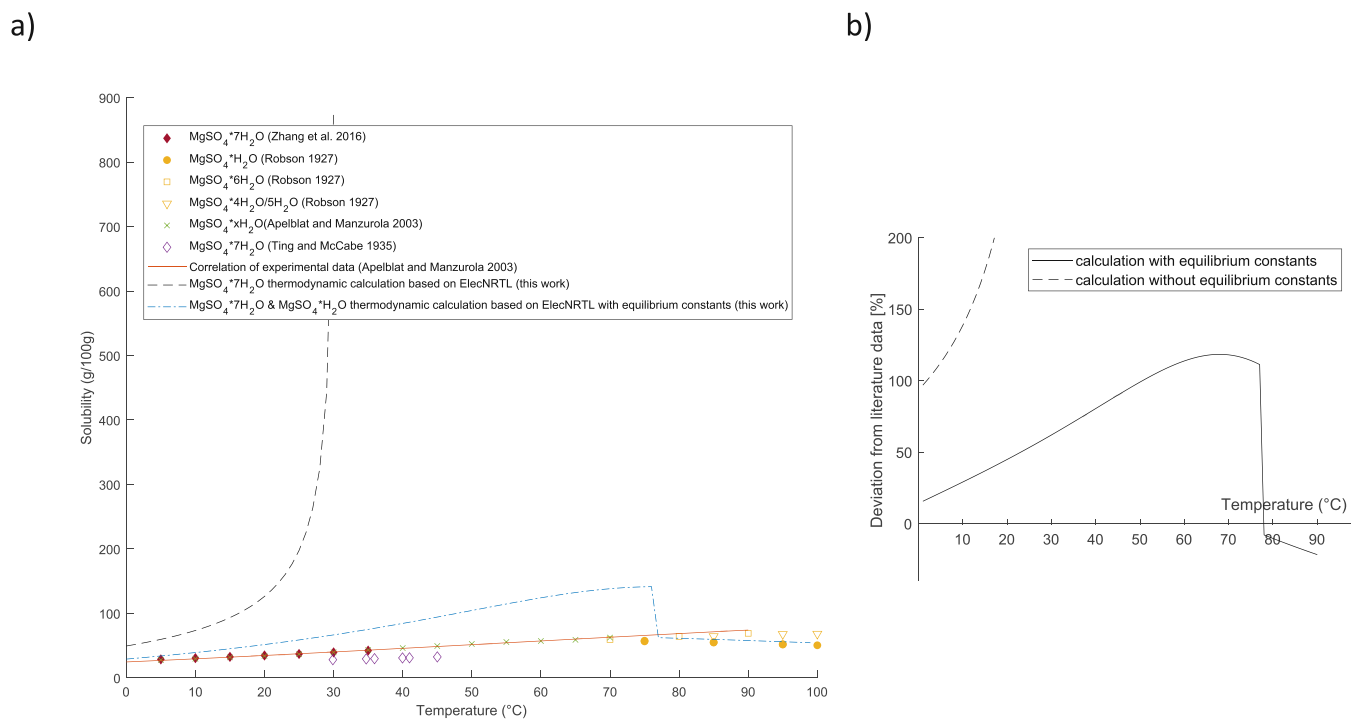


Figure 13. (a) Solubility of MgSO_4 hydrates in water over temperature.^{37–40} (b) Deviation of calculated values from the correlation of literature data by Apelblat and Manzurola (see eq 26).

Compared to the data of Bichowsky, the model describes the solubility in CaSO_4 -saturated solution at 25 °C very well.

3.6. Solubility of Magnesium Sulfate (MgSO_4). Figure 13 shows the calculated solubility of MgSO_4 hydrates in water over temperature compared with data from the literature.

The model recognizes only heptahydrate as the present hydrate form when calculating the solubility based on the reference state Gibbs free energies. Furthermore, the model predicts a significant increase in solubility with increasing

temperatures. However, experimental data from literature show that up to 48 °C heptahydrate is the stable hydrate form, between 48 and 68 °C hexahydrate is the stable form, and monohydrate is the stable one at temperatures higher than 68 °C.^{38,39} When applying the equilibrium constants, the model predicts heptahydrate and monohydrate as stable forms. The model does not recognize hexahydrate as a stable form between 48 and 68 °C. While the calculated solubility of the monohydrate fits the literature data very well, the calculated

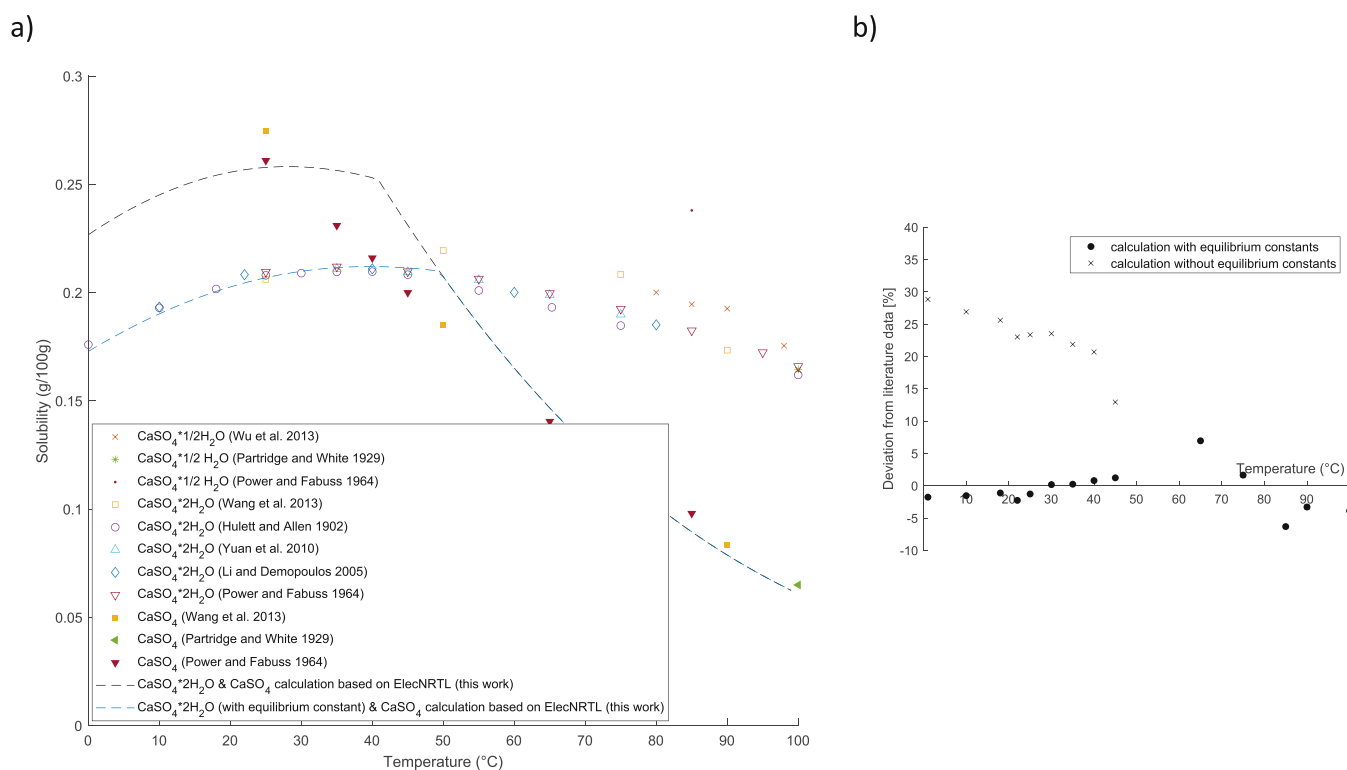


Figure 14. (a) Solubility of CaSO_4 hydrates in water over temperature.^{41–47} (b) Deviation of calculated values from the literature data (see eq 26).

solubility of heptahydrate increases more strongly with temperature than reported in literature. This effect and the fact that hexahydrate is not recognized lead to a significant overestimation of the solubility of up to 118% at a temperature of 70 $^\circ\text{C}$. The experimental solubility data for hexahydrate are scarce, which makes a consistent adaptation of the model difficult.

3.7. Solubility of Calcium Sulfate (CaSO_4). Figure 14 shows the calculated solubility of CaSO_4 hydrates in water over temperature compared with data from the literature.

Experimental data from the literature report the dihydrate as a stable form at temperatures up to around 50 $^\circ\text{C}$. At higher temperatures, the stable form is the anhydrite. The model describes this change in the stable hydrate form very well. When calculating the solubility based on the reference state Gibbs free energies, the model describes the solubility of the anhydrite very well and overestimates the solubility of the dihydrate. The calculated solubility of the dihydrate is improved by applying equilibrium constants for its precipitation reaction.

4. CONCLUSIONS

The electrolyte NRTL activity coefficient model was applied to model the vapor, liquid, and solid phases of the MgO - CaO - CO_2 - SO_2 - H_2O - O_2 system.

To model the SO_2 solubility in water, the study suggests that a simplification of the model to a simple vapor–liquid equilibrium calculation using Henry's law is possible without sacrificing model accuracy. When calculating the SO_2 absorption into $\text{Mg}(\text{OH})_2$ slurry, considering the electrolyte reaction equilibrium is crucial. The model calculates the absorption trend correctly but shows quantitative deviations from available experimental data from the literature. However, experimental data sets for the SO_2 absorption in $\text{Mg}(\text{OH})_2$ in literature are scarce and the evaluation of the model using available data is inconclusive on whether deviations are caused by measurement

uncertainties or model parameters. More experimental data are necessary for a trustful evaluation of the model and a potential adaptation of model parameters.

The model predicts potential stable precipitates in the system at a temperature range from 0 to 100 $^\circ\text{C}$ correctly. The study shows that the chemical equilibrium of the precipitation of $\text{Mg}(\text{OH})_2$, $\text{Ca}(\text{OH})_2$, CaSO_3 hemihydrate, and CaSO_4 anhydrite can be calculated satisfactorily from the reference state Gibbs free energies of the participating components. The chemical equilibrium of the precipitation of MgSO_3 hexahydrate and trihydrate, MgSO_4 monohydrate and heptahydrate, and CaSO_4 dihydrate requires built-in or user-supplied parameters to describe the equilibrium constants K_{eq} as a function of temperature to achieve high accuracy of the model. The model overestimates the solubility of MgSO_4 heptahydrate. Due to its high solubility, MgSO_4 is not a critical precipitate in the system. This leads the authors to the conclusion that the model is applicable to simulate precipitation in the system even though the solubility of MgSO_4 heptahydrate is overestimated.

The study shows that the model describes the chemical system in equilibrium satisfactorily and is a valuable tool for predicting precipitates in the system. However, it must be considered that the model cannot cover the dynamic behavior of hydrate transition and metastability of possible precipitates in fast-changing and unstable systems.

AUTHOR INFORMATION

Corresponding Author

Bahram Haddadi – Institute of Chemical, Environmental and Bioscience Engineering, TU Wien, 1060 Vienna, Austria;

orcid.org/0000-0003-3403-6346;

Email: bahram.haddadi@tuwien.ac.at

Authors

Barbara D. Weiß – Competence Center CHASE GmbH, 1030 Vienna, Austria; Institute of Chemical, Environmental and Bioscience Engineering, TU Wien, 1060 Vienna, Austria; orcid.org/0000-0002-5138-3721

Michael Harasek – Institute of Chemical, Environmental and Bioscience Engineering, TU Wien, 1060 Vienna, Austria; orcid.org/0000-0002-6490-5840

Complete contact information is available at:
<https://pubs.acs.org/10.1021/acs.iecr.3c00868>

Notes

The authors declare no competing financial interest.

ACKNOWLEDGMENTS

The authors specially thank Walter Wukovits of the Institute of Chemical, Environmental and Bioscience Engineering at TU Wien for the support in process simulation and the use of Aspen Plus. This work was financially supported by the Competence Center CHASE GmbH. CHASE Competence Center is subsidized in the frame of COMET – Competence Centers for Excellent Technologies by BMVIT, BMWFW, Wirtschaftsuniversität Wien, State of Upper Austria, and its scientific partners. The COMET program is handled by FFG. The support by the project partner Sappi Papier Holding GmbH is greatly acknowledged.

NOMENCLATURE

A_ϕ	Debye–Hückel parameter
F_p	Poynting factor
G	Gibbs energy
H	Henry's constant
I_x	ionic strength (mole fraction scale)
K	equilibrium constant
M	molecular weight
N_A	Avogadro's number
Q_e	electron charge
R	gas constant
T	temperature
V	volume
Z	compressibility factor
$a_{ij}, b_{ij}, c_{ij}, d_{ij}, e_{ij}, f_{ij}$	unsymmetric binary parameters
a, a_i	attraction coefficient, attraction coefficient of pure component i
b, b_i	limiting volume coefficient, limiting volume coefficient of pure component i
d	mass density
f	fugacity
k	Boltzmann constant
n	mole number
p	pressure
p_i	vapor pressure of pure component i
r_i	born radius of the ionic species i
x	mole fraction in the liquid phase
y	mole fraction in the vapor phase
z_i	charge number of ion i

Greek symbols

ϕ	fugacity coefficient
ϵ	dielectric constant
α_{ij}	non randomness factor
ρ	"closest approach" parameter (following Pitzer set to 14.9)
τ_{ij}	energy parameter

γ activity coefficient

Subscripts

i component i
 m molar
 c critical
 s solvent
 w water

Superscripts

v vapor phase
 l liquid phase
 ∞ infinite dilution
 $*$ reference state
 E excess

REFERENCES

- Zou, Y.; Liu, X.; Zhu, T.; Tian, M.; Cai, M.; Zhao, Z.; Wu, H. Simultaneous Removal of NO_x and SO₂ by MgO Combined with O₃ Oxidation: The Influencing Factors and O₃ Consumption Distributions. *ACS Omega* **2019**, *4*, 21091–21099.
- Steindl, M.; Röder, T.; Simharl, R.; Harasek, M.; Friedl, A.; Sixta, H. Online Raman monitoring of the phase transition of magnesium sulphite hydrate. *Chem. Eng. Process.: Process Intensif.* **2005**, *44*, 471–475.
- Si, T.; Wang, C.; Yan, X.; Zhang, Y.; Ren, Y.; Hu, J.; Anthony, E. J. Simultaneous removal of SO₂ and NO_x by a new combined spray-and-scattered-bubble technology based on preozonation: From lab scale to pilot scale. *Appl. Energy* **2019**, *242*, 1528–1538.
- Schöggel, K.; Steindl, M.; Friedl, A.; Weber, H. K.; Sixta, H. Calculation of physical property data of the system MgO–SO₂–H₂O and their implementation in Aspen Plus. *Lenzinger Berichte* **2006**, *86*, 56–62.
- Zidar, M.; Golob, J.; Veber, M.; Vlady, V. Absorption of SO₂ into Aqueous Solutions. 2. Gas–Liquid Equilibrium of the MgO–SO₂–H₂O System and Graphical Presentation of Operation Lines in an Equilibrium Diagram. *Ind. Eng. Chem. Res.* **1997**, *36*, 4342–4346.
- Pasiuk-Bronikowska, W.; Rudzinski, K. J. Absorption of SO₂ into aqueous systems. *Chem. Eng. Sci.* **1991**, *46*, 2281–2291.
- Weiß, B. D.; Harasek, M. Solubility Data of Potential Salts in the MgO–CaO–SO₂–H₂O–O₂ System for Process Modeling. *Processes* **2021**, *9*, 50.
- Chen, C.-C.; Evans, L. B. A local composition model for the excess Gibbs energy of aqueous electrolyte systems. *AIChE J.* **1986**, *32*, 444–454.
- Mock, B.; Evans, L. B.; Chen, C.-C. Thermodynamic representation of phase equilibria of mixed-solvent electrolyte systems. *AIChE J.* **1986**, *32*, 1655–1664.
- Redlich, O.; Kwong, J. N. S. On the thermodynamics of solutions; an equation of state; fugacities of gaseous solutions. *Chem. Rev.* **1949**, *44*, 233–244.
- Sanku, M. G.; Svensson, H. Modelling the precipitating non-aqueous CO₂ capture system AMP–NMP, using the unsymmetric electrolyte NRTL. *Int. J. Greenhouse Gas Control* **2019**, *89*, 20–32.
- Rumpf, B.; Maurer, G. Solubilities of hydrogen cyanide and sulfur dioxide in water at temperatures from 293.15 to 413.15 K and pressures up to 2.5 MPa. *Fluid Phase Equilib.* **1992**, *81*, 241–260.
- Young, C. L.; Gerrard, W.; Battino, R. Sulfur Dioxide, Chlorine, Fluorine and Chlorine Oxides. *Solubility Data Ser.* **1983**, *12*, 4–77.
- Mondal, M. K. Absorption equilibria of dilute sulphur dioxide in Mg(OH)₂ slurry. *Fluid Phase Equilib.* **2007**, *262*, 111–120.
- Dupré; Bialas, J. Zur Bestimmung der Löslichkeit von Magnesia und Zinkoxyd in Wasser auf Grund des elektrischen Leitvermögens. *Z. Angew. Chem.* **1903**, *16*, 54–55.
- Remy, H.; Kuhlmann, A. Löslichkeitsbestimmungen an schwer löslichen Stoffen. II. Wasserlöslichkeit der Oxyde von Beryllium, Aluminium, Zink, Cadmium, Blei, Kupfer und Silber. *Fresenius, Zeitschrift f. anal. Chemie* **1924**, *65*, 161–181.

- (17) Busch, W. Über die Verwendbarkeit der elektrometrischen Titration zur Löslichkeitsbestimmung schwerlöslicher Oxide. *Zeitschrift für anorganische und allgemeine Chemie* **1927**, *161*, 161–179.
- (18) Whipple, G. C.; Mayer, A. The Solubility of Calcium Carbonate and of Magnesium Hydroxide and the Precipitation of These Salts with Lime Water. *J. Infect. Dis.* **1906**, *3*, S151–S165.
- (19) Hostetler, P. B. The stability and surface energy of brucite in water at 25 degrees C. *Am. J. Sci.* **1963**, *261*, 238–258.
- (20) Einaga, H. The hydrolytic precipitation reaction of Mg(II) from aqueous NaNO₃ solution. *J. Inorg. Nucl. Chem.* **1981**, *43*, 229–233.
- (21) Lambert, I.; Clever, H. L. Alkaline Earth Hydroxides in Water and aqueous solutions. *Solubility Data Ser.* **1992**, *52*, 49–226.
- (22) Dongdong, L.; Dandan, G.; Yaping, D.; Wu, L. Modeling of phase relations and thermodynamics in the Mg(OH)₂ + MgSO₄ + H₂O system with implications on magnesium hydroxide sulfate cement. *Calphad* **2019**, *67*, No. 101675.
- (23) Scholz, F.; Kahlert, H. The calculation of the solubility of metal hydroxides, oxide-hydroxides, and oxides, and their visualisation in logarithmic diagrams. *ChemTexts* **2015**, *1*, 1–9.
- (24) Bassett, H.; Taylor, H. S. CLXXX.—Calcium nitrate. Part III. The three-component system: calcium nitrate–lime–water. *J. Chem. Soc., Trans.* **1914**, *105*, 1926–1941.
- (25) Yeatts, L. B.; Marshall, W. L. Aqueous systems at high temperature. XVIII. Activity coefficient behavior of calcium hydroxide in aqueous sodium nitrate to the critical temperature of water. *J. Phys. Chem.* **1967**, *71*, 2641–2650.
- (26) Bates, R. G.; Bower, V. E.; Smith, E. R. Calcium hydroxide as a highly alkaline pH standard. *J. Res. Natl. Bur. Stand* **1956**, *56*, 305.
- (27) Cameron, F. K.; Robinson, W. O. The System, Lime, Nitric Acid and Water. *J. Phys. Chem.* **1907**, *11*, 273–278.
- (28) Lowell, P. S.; Meserole, F. P.; Parsons, T. B. *Precipitation Chemistry of Magnesium Sulfite Hydrates in Magnesium Oxide Scrubbing*. Interagency Energy-Environment Research and Development series 1977, EPA-600/7-77-109 (EPA-600/7-77-109).
- (29) Hagiwara, H. Studies of Magnesium Sulphite. *Bull. Inst. Phys. Chem. Res.* **1933**, *12*, 976–983.
- (30) Markant, H. P.; McIlroy, R. A.; Matty, R. E. Absorption Studies - MgO-SO₂ Systems. *Tappi* **1962**, *45*, 849–854.
- (31) Söhnel, O.; Rieger, A. Solubilities of Magnesium Sulfite Hydrates. *J. Chem. Eng. Data* **1994**, *39*, 161–162.
- (32) Nývlt, J. Solubilities of Magnesium Sulfite. *J. Therm. Anal. Calorim.* **2001**, *66*, 509–512.
- (33) Lutz, H. D. Sulfites, Selenites and Tellurites. *Solubility Data Ser.* **1986**, *26*, 153–193.
- (34) van der Linden, T. Solubility of calcium sulphite in water and in sugar solutions. *J. Chem. Technol. Biotechnol.* **1917**, *36*, 96.
- (35) Bobrovnik, L. D.; Kotelnikova, L. P. Solubility of calcium sulphite in sugar solutions. *Izv. Vyssh. Uchebn. Zaved., Pishch. Tekhnol.* **1974**, *4*, 155–156.
- (36) Bichowsky, F. R. FREE ENERGY OF THE THIOSULFATE ION. *J. Am. Chem. Soc.* **1923**, *45*, 2235.
- (37) Zhang, Y.; Asselin, E.; Li, Z. Solubility Measurement and Chemical Modeling of MgSO₄·7H₂O in the Ti(SO₄)₂·H₂O System. *J. Chem. Eng. Data* **2016**, *61*, 2363–2370.
- (38) Robson, H. L. THE SYSTEM MgSO₄·H₂O FROM 68 TO 240° I. *J. Am. Chem. Soc.* **1927**, *49*, 2772–2783.
- (39) Apelblat, A.; Manzurola, E. Solubilities and vapour pressures of saturated aqueous solutions of sodium tetraborate, sodium carbonate, and magnesium sulfate at freezing-temperature lowerings of sodium tetraborate and sodium carbonate solutions. *J. Chem. Thermodyn.* **2003**, *35*, 221–238.
- (40) Ting, H. H.; McCabe, W. L. Solubility of Magnesium Sulfate Heptahydrate. *Ind. Eng. Chem.* **1934**, *26*, 1207–1208.
- (41) Wu, X.; Wang, K.; Xiong, Z.; Ye, Y. Solubility of α-Calcium Sulfate Hemihydrate in Ca–Mg–K Chloride Salt Solution at (353.0 to 371.0) K. *J. Chem. Eng. Data* **2013**, *58*, 48–54.
- (42) Partridge, E. P.; White, A. H. THE SOLUBILITY OF CALCIUM SULFATE FROM 0 TO 200°. *J. Am. Chem. Soc.* **1929**, *51*, 360–370.
- (43) Power, W. H.; Fabuss, B. M. Transient Solubilities in the Calcium Sulfate-Water System. *J. Chem. Eng. Data* **1964**, *9*, 437–442.
- (44) Wang, W.; Zeng, D.; Chen, Q.; Yin, X. Experimental determination and modeling of gypsum and insoluble anhydrite solubility in the system CaSO₄–H₂SO₄–H₂O. *Chem. Eng. Sci.* **2013**, *101*, 120–129.
- (45) Hulett, G. A.; Allen, L. E. THE SOLUBILITY OF GYPSUM. *J. Am. Chem. Soc.* **1902**, *24*, 667–679.
- (46) Yuan, T.; Wang, J.; Li, Z. Measurement and modelling of solubility for calcium sulfate dihydrate and calcium hydroxide in NaOH/KOH solutions. *Fluid Phase Equilib.* **2010**, *297*, 129–137.
- (47) Li, Z.; Demopoulos, G. P. Solubility of CaSO₄ 4 Phases in Aqueous HCl + CaCl₂ Solutions from 283 K to 353 K. *J. Chem. Eng. Data* **2005**, *50*, 1971–1982.
- (48) Söhnel, O.; Rieger, A. Phase Transition of Magnesium Sulphite Hydrates in Aqueous Suspension. *Cryst. Res. Technol.* **1993**, *28* (4), 487–493.

Journal Paper III

Die approbierte gedruckte Originalversion dieser Dissertation ist an der TU Wien Bibliothek verfügbar.
The approved original version of this doctoral thesis is available in print at TU Wien Bibliothek.

Finding Optimized Process Conditions to Minimize Precipitations in an SO₂ Absorption Process Using Thermodynamic Process Simulation

Barbara D. Weiß^{a*}, Wolfgang Fuchs^b, Michael Harasek^a

^a Thermal Process Engineering - Computational Fluid Dynamics, Institute of Chemical, Environmental & Bioscience Engineering, TU Wien, Getreidemarkt 9, 1060 Vienna, Austria

^b Sappi Austria Produktions-GmbH & Co. KG, Sappi Europe, Brucker Strasse 21, 8101 Gratkorn, Austria
barbara.weiss@tuwien.ac.at

A process model to describe SO₂ absorption from exhaust gas using an absorptive magnesium-based slurry was developed in Aspen Plus[®] V10. The model includes the thermodynamic description of the electrolyte system MgO-CaO-SO₂-H₂O-O₂-CO₂, including precipitation reactions in the system. The property method electrolyte-NRTL with an asymmetric reference state was chosen as the thermodynamic method. The model was evaluated using plant data for pH value, HSO₃⁻ and SO₃⁻ content of the liquid phase from an industrial SO₂ absorption venturi system of the pulp and paper industry. The model shows good accuracy in describing the pH value and the combined HSO₃⁻ and SO₃⁻ content. Sensitivity analyses were performed to identify key parameters that influence unwanted precipitation reactions in the system and to support the optimization of the SO₂ absorption process. Temperature and the Mg(OH)₂/SO₂ ratio in the system were identified as key parameters influencing the formation and precipitation of sulfites. The pH value was identified as a key parameter affecting the precipitation of magnesium hydroxide. The model predicts the precipitation of Mg(OH)₂ at a pH value of higher than 8 and the precipitation of MgSO₃ trihydrate at a temperature higher than 78 °C or a slurry/SO₂ ratio higher than around 4. The performed analyses can support optimized process design decisions for SO₂ absorption processes to avoid limiting precipitation issues.

1. Introduction

The chemisorption of SO₂ is a well-established technology to reduce SO₂ emissions from SO₂ containing exhaust gas from different industries such as coal-firing plants, sintering plants, or pulp production. Besides the traditionally used absorptive slurry based on limestone (Ozyuguran and Ersoy-Mericboyu 2010), a magnesium based slurry is widely used as an absorbent with the advantage of better recyclability and higher SO₂ removal efficiencies (Liu et al. 2020). Magnesium hydroxide as an absorptive slurry gained increased attention due to the possibility of removing the pollutants SO₂ and NO_x simultaneously (Zou et al. 2019). In the pulp production industry, magnesium hydroxide is used as slurry to control SO₂ emissions and simultaneously recover the cooking liquor. Eqs(1) – (3) summarize the main reactions of the chemical recovery for magnesium-based systems:



After the combustion of black liquor, magnesium oxide is recovered from the ash and hydrated to serve as absorbent for the SO₂ removal in the absorption venturi system. There, SO₂ reacts with the slurry to form magnesium bisulfite, which serves again as cooking liquor for pulp production.

The goal of such chemical recovery system is the full reuse of required chemicals to target a closed-loop process control. However, unwanted precipitation reactions in the system can challenge this goal. Uncontrolled precipitation can lead to blockage of pipes, shortens maintenance intervals, and increases the chemical demand. Therefore, it is essential to understand the reaction system leading to precipitations when designing wet flue gas desulfurization systems. While most studies focus on removal efficiency, the issue of precipitation is often overlooked, leading to a lack of studies targeting that issue in literature. In a previous work, potential salts and their solubility data from literature were studied (Weiß and Harasek 2021). In literature, a solid database for the solubility of potential salts in water is available. However, potential precipitations are dependent on the complex present electrolyte system. A rigorous thermodynamic model can provide a tool to analyze the effect of different parameters on the precipitation by including all necessary electrolyte reactions. The MgO-H₂O-SO₂ system was previously modeled by Zidar et al. using the Rudzinsky+Pitzer-Ion activity coefficient model (Zidar et al. 1997). Steindl et al. described the same system using the electrolyte NRTL method (Steindl et al. 2008). The newer study of Si et al. applies the electrolyte NRTL method on an SO₂ absorption system based on calcium (Si et al. 2019). This study investigates the effect of temperature, pH value, SO₂, and Mg(OH)₂ in the system on precipitation calculated by the electrolyte NRTL method. The flowsheet and input data are based on an industrial absorption plant of the chemical recovery in the pulp industry.

2. Methods

The system was modeled as a steady-state process in thermodynamic equilibrium. The thermodynamic framework, the reaction system, and the flowsheet calculations were set and performed using the sequential modular simulation tool Aspen Plus® V10. The following summarizes the applied methodology.

2.1 Thermodynamic framework

The system was rigorously modeled using the built-in elecNRTL property method in Aspen Plus® V10. This method uses the electrolyte NRTL activity coefficient model as proposed by Chen and Evans and extended by Mock et al. The vapor phase properties were calculated using the Redlich-Kwong equation of state. As for every activity coefficient model, the activity coefficient expresses the deviation of a solution from ideality. The reference state of the system defines which state is referred to as ideal. For ions, the reference state of infinite dilution in the actual mixed solvent present was chosen (asymmetric reference state). For all other components, the reference state is that of a pure compound. The reference state for supercritical, dissolved gases, defined as Henry components in Aspen Plus®, is at infinite dilution (asymmetric reference state) at system temperature and pressure. In the studied system, SO₂, O₂, and CO₂ were defined as Henry components. All pure component and binary interaction parameters were retrieved from the standard implemented data banks in Aspen Plus® V10.

2.2 Chemical system

Aspen Plus® V10 allows the description of electrolyte systems using the true component approach. The true component approach, unlike the apparent component approach, means that all true components of the electrolyte system, including ions, salts, and molecular species, are reported. The chemical equilibrium is calculated using built-in or user-supplied parameters to describe the equilibrium constants K_{eq} as a function of temperature. If no equilibrium constants are given, the equilibrium is calculated from the reference state Gibbs free energies of the participating components. Table 1 summarizes all considered reactions and how the chemical equilibrium was calculated.

Table 1: Considered electrolyte system

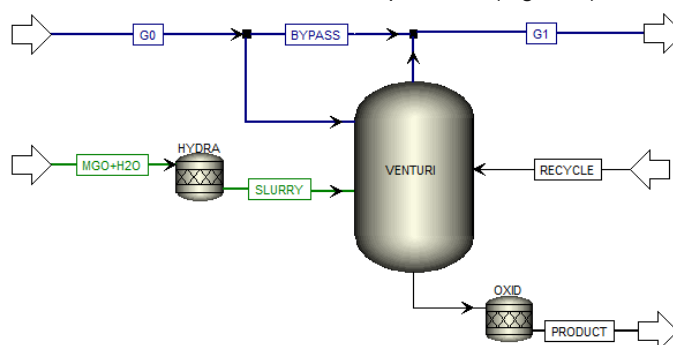
Reaction	Type	Calculation of chemical equilibrium
$2 \text{H}_2\text{O} \leftrightarrow \text{OH}^- + \text{H}_3\text{O}^+$	Equilibrium	built-in coefficients for K_{eq}
$2 \text{H}_2\text{O} + \text{SO}_2 \leftrightarrow \text{H}_3\text{O}^+ + \text{HSO}_3^-$	Equilibrium	built-in coefficients for K_{eq}
$\text{H}_2\text{O} + \text{HSO}_3^- \leftrightarrow \text{H}_3\text{O}^+ + \text{SO}_3^{2-}$	Equilibrium	built-in coefficients for K_{eq}
$\text{H}_2\text{O} + \text{HCl} \leftrightarrow \text{Cl}^- + \text{H}_3\text{O}^+$	Equilibrium	Gibbs free energy calculation
$\text{H}_2\text{SO}_4 + \text{H}_2\text{O} \leftrightarrow \text{H}_3\text{O}^+ + \text{HSO}_4^-$	Equilibrium	Gibbs free energy calculation
$\text{H}_2\text{O} + \text{HSO}_4^- \leftrightarrow \text{H}_3\text{O}^+ + \text{SO}_4^{2-}$	Equilibrium	Gibbs free energy calculation
$\text{MgOH}^+ \leftrightarrow \text{OH}^- + \text{Mg}^{++}$	Equilibrium	Gibbs free energy calculation
$\text{CaOH}^+ \leftrightarrow \text{OH}^- + \text{Ca}^{++}$	Equilibrium	Gibbs free energy calculation
$2 \text{H}_2\text{O} + \text{CO}_2 \leftrightarrow \text{H}_3\text{O}^+ + \text{HCO}_3^-$	Equilibrium	built-in coefficients for K_{eq}
$\text{H}_2\text{O} + \text{HCO}_3^- \leftrightarrow \text{H}_3\text{O}^+ + \text{CO}_3^{2-}$	Equilibrium	built-in coefficients for K_{eq}
$\text{Mg}(\text{OH})_2 \rightarrow \text{OH}^- + \text{MgOH}^+$	Dissociation	-
$\text{Ca}(\text{OH})_2 \rightarrow \text{OH}^- + \text{CaOH}^+$	Dissociation	-

Table 1: Considered electrolyte system, continued

Reaction	Type	Calculation of chemical equilibrium
$2 \text{H}_2\text{O} + \text{CO}_2 \leftrightarrow \text{H}_3\text{O}^+ + \text{HCO}_3^-$	Equilibrium	built-in coefficients for K_{eq}
$\text{H}_2\text{O} + \text{HCO}_3^- \leftrightarrow \text{H}_3\text{O}^+ + \text{CO}_3^{2-}$	Equilibrium	built-in coefficients for K_{eq}
$\text{Mg}(\text{OH})_2 \rightarrow \text{OH}^- + \text{MgOH}^+$	Dissociation	-
$\text{Ca}(\text{OH})_2 \rightarrow \text{OH}^- + \text{CaOH}^+$	Dissociation	-
$\text{MgSO}_4 \rightarrow \text{Mg}^{++} + \text{SO}_4^{--}$	Dissociation	-
$\text{MgSO}_3 \rightarrow \text{Mg}^{++} + \text{SO}_3^{--}$	Dissociation	-
$\text{CaSO}_4 \rightarrow \text{Ca}^{++} + \text{SO}_4^{--}$	Dissociation	-
$\text{CaSO}_3 \rightarrow \text{Ca}^{++} + \text{SO}_3^{--}$	Dissociation	-
$\text{MgCO}_3 \rightarrow \text{Mg}^{++} + \text{CO}_3^{--}$	Dissociation	-
$\text{CaCO}_3 \rightarrow \text{Ca}^{++} + \text{CO}_3^{--}$	Dissociation	-
$\text{Mg}(\text{OH})_2 (\text{s}) \leftrightarrow \text{OH}^- + \text{MgOH}^+$	Salt precipitation	Gibbs free energy calculation
$\text{Ca}(\text{OH})_2 (\text{s}) \leftrightarrow \text{OH}^- + \text{CaOH}^+$	Salt precipitation	Gibbs free energy calculation
$\text{MgSO}_3 \cdot 6 \text{H}_2\text{O} \leftrightarrow \text{Mg}^{++} + \text{SO}_3^{--} + 6 \text{H}_2\text{O}$	Salt precipitation	built-in coefficients for K_{eq}
$\text{MgSO}_3 \cdot 3 \text{H}_2\text{O} \leftrightarrow \text{Mg}^{++} + \text{SO}_3^{--} + 3 \text{H}_2\text{O}$	Salt precipitation	built-in coefficients for K_{eq}
$\text{CaSO}_3 \cdot \frac{1}{2} \text{H}_2\text{O} \leftrightarrow \text{Ca}^{++} + \text{SO}_3^{--} + \frac{1}{2} \text{H}_2\text{O}$	Salt precipitation	Gibbs free energy calculation
$\text{MgSO}_4 \cdot \text{H}_2\text{O} \leftrightarrow \text{Mg}^{++} + \text{SO}_4^{--} + \text{H}_2\text{O}$	Salt precipitation	built-in coefficients for K_{eq}
$\text{MgSO}_4 \cdot 7 \text{H}_2\text{O} \leftrightarrow \text{Mg}^{++} + \text{SO}_4^{--} + 7 \text{H}_2\text{O}$	Salt precipitation	built-in coefficients for K_{eq}
$\text{CaSO}_4 \cdot 2 \text{H}_2\text{O} \leftrightarrow \text{Ca}^{++} + \text{SO}_4^{--} + 2 \text{H}_2\text{O}$	Salt precipitation	built-in coefficients for K_{eq}
$\text{CaSO}_4 \leftrightarrow \text{Ca}^{++} + \text{SO}_4^{--}$	Salt precipitation	Gibbs free energy calculation

2.3 Flowsheet and input data

The developed flowsheet was based on an industrial absorption unit (Figure 1).

Figure 1: Flowsheet of SO_2 absorption venturi system in Aspen Plus® V10

It consists of a flash unit "VENTURI", which calculates the chemical and phase equilibrium at atmospheric pressure of 1.013 bar and without any heat duty. In an industrial venturi system, the physical solubility of SO_2 is considered as the limiting process preventing the system to be in equilibrium (Marocco 2010). To adapt the equilibrium model to the real process, a gas bypass allows adjusting the venturi efficiency. The reactor "HYDRA" covers the hydration of MgO and CaO to $\text{Mg}(\text{OH})_2$ and $\text{Ca}(\text{OH})_2$ respectively, resulting in the input stream "SLURRY". The hydration reactor was implemented as a stoichiometric reactor with a hydration rate of 90 %. The stoichiometric reactor "OXID" covers the oxidation of SO_3^{--} to SO_4^{--} in the liquid outlet of the venturi. Several studies describe the kinetics of the oxidation of SO_2 in the liquid phase. Due to the complex nature and fast kinetics of the reaction (Hudson et al. 1979), it was assumed that the total O_2 in the liquid phase reacts with SO_3^{--} . The initial composition of the exhaust gas "G0" is summarized in Table 2.

Table 2: Gas composition G0 in vol% (standard conditions, dry)

N_2	SO_2	O_2	CO_2	NO
78.43	0.41	5.94	13.52	1.71

In industrial SO_2 absorption processes, the exhaust gas usually passes several absorption units in series, and the liquid outlet of an absorption unit is recycled counter current into the previous unit. The stream "RECYCLE"

represents this liquid recycle stream. The composition of the input streams "RECYCLE" and "MGO+H2O" are summarized in Table 3.

Table 3: Composition of input streams RECYCLE and MGO+H2O in mass-%

	H ₂ O	Mg(HSO ₃) ₂	MgSO ₃	MgSO ₄	CaSO ₃	CaSO ₄	MgCO ₃	MgO	CaO	N ₂	Others
RECYCLE	97.20	1.66	0.82	0.04	0.07		0.03	0.08		0.06	0.05
MGO+H2O	90.95			0.34		0.04		7.84	0.35		0.48

On the presented flowsheet, sensitivity analyses were performed to study the effect of temperature, pH value and the input ratio of slurry and SO₂.

3. Results and discussion

In the following the model is validated using industrial plant data. Furthermore, results of the performed sensitivity analyses are presented and discussed.

3.1 Validation of model with plant data

Table 4 compares the calculated values of the liquid product stream with measured plant data at process conditions.

Table 4: Comparison of calculated values with data of industrial plant (with σ = standard deviation) in product ($T=68$ °C; $\dot{m}_{Gas0}= 374,000$ kg/h, $\dot{m}_{Recycle}= 83,000$ kg/h, $\dot{m}_{Slurry}=3,840$ kg/h, venturi efficiency = 0.55)

	Units	Calculated	Plant data
pH		5.47	5.18 σ = 0.07
SO ₃ ⁻ + HSO ₃ ⁻	mass-% SO ₂	2.94	3.04 σ = 0.22
SO ₃ ⁻	mass-% SO ₂	0.13	0.39 σ = 0.09

The calculated amount of SO₂, which is present as SO₃⁻ and HSO₃⁻ in the liquid product, is in very good agreement with the measured value. The pH value shows only a small deviation of 0.22 pH units, considering the standard deviation of the measurement. Compared to measurements, the model underestimates the amount of SO₂, which is present as SO₃⁻.

3.2 Effect of temperature on solid precipitation

Figure 2a and b show the precipitation as a function of temperature, while all other input parameters were unchanged.

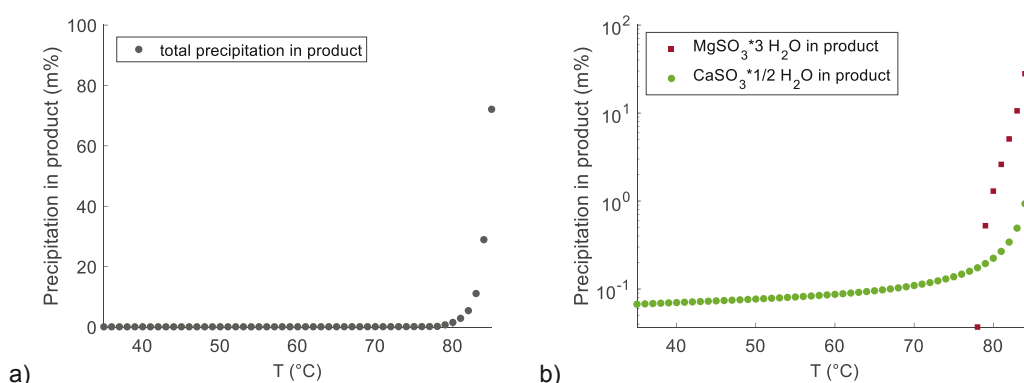


Figure 2: Precipitation in product as a function of temperature; (a) total precipitation mapped in linear scale; (b) precipitation of MgSO₃* 3 H₂O and CaSO₃* 1/2 H₂O mapped in logarithmic scale ($\dot{m}_{Gas0}= 374,000$ kg/h, $\dot{m}_{Recycle}= 83,000$ kg/h, $\dot{m}_{Slurry}=3,840$ kg/h, venturi efficiency = 0.55)

The process model reports precipitation of CaSO₃ hemihydrate (CaSO₃* 1/2 H₂O) over the whole considered temperature range. CaSO₃ hemihydrate has the lowest solubility in water compared to the other considered sulfates and sulfites (Weiß and Harasek 2021). Its solubility decreases with temperature, which corresponds to the increase of CaSO₃* 1/2 H₂O in the product with temperature. However, due to the small amount of calcium

present in the system, the effect of its precipitation in the product stream is small and makes up only around 0.1 mass-% in the product. At temperatures higher than 78 °C, the model also reports MgSO_3 trihydrate ($\text{MgSO}_3 \cdot 3 \text{H}_2\text{O}$) as precipitated solid. This can be explained by the shift in the vapor-liquid phase equilibrium with increasing temperature. The total liquid product flow decreases with increasing temperature. As a consequence, the concentration of MgSO_3 in the liquid product exceeds the solubility limit leading to the precipitation of $\text{MgSO}_3 \cdot 3 \text{H}_2\text{O}$. Another factor is that at higher temperatures, the less soluble $\text{MgSO}_3 \cdot 3 \text{H}_2\text{O}$ is the dominantly occurring form, while at lower temperatures, the more soluble $\text{MgSO}_3 \cdot 6 \text{H}_2\text{O}$ is the stable form (Steindl et al. 2005). The transition from hexahydrate to trihydrate as stable form can explain the precipitation of MgSO_3 at higher temperatures.

3.3 Effect of pH value on solid precipitation

Figure 3 shows the effect of the pH value in the system on solid precipitation.

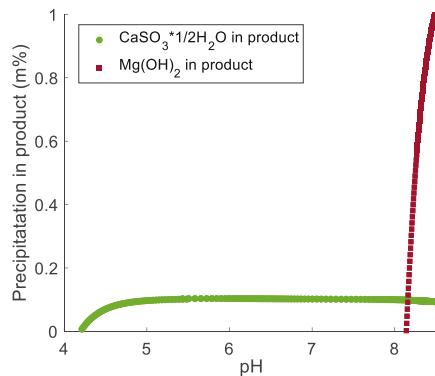


Figure 3: Precipitation in product as a function of pH value adjusted by adding HCl and NaOH ($T = 68 \text{ }^\circ\text{C}$, $\dot{m}_{\text{Gas}0} = 374,000 \text{ kg/h}$, $\dot{m}_{\text{Recycle}} = 83,000 \text{ kg/h}$, $\dot{m}_{\text{Slurry}} = 3,840 \text{ kg/h}$, venturi efficiency = 0.55)

The pH value was adjusted by adding HCl and NaOH to the system. HCl and NaOH were chosen as they are not part of other reactions in the electrolyte system other than their dissociation. The analyses show that $\text{Mg}(\text{OH})_2$ precipitates when a pH value of 8 is exceeded. This corresponds to the studies by Scholz and Kahlert (Scholz and Kahlert 2015).

3.4 Effect of slurry/ SO_2 ratio on solid precipitation

Figure 4a and b show the effect of the mass flow ratio of slurry and SO_2 into the venturi flash on the precipitation.

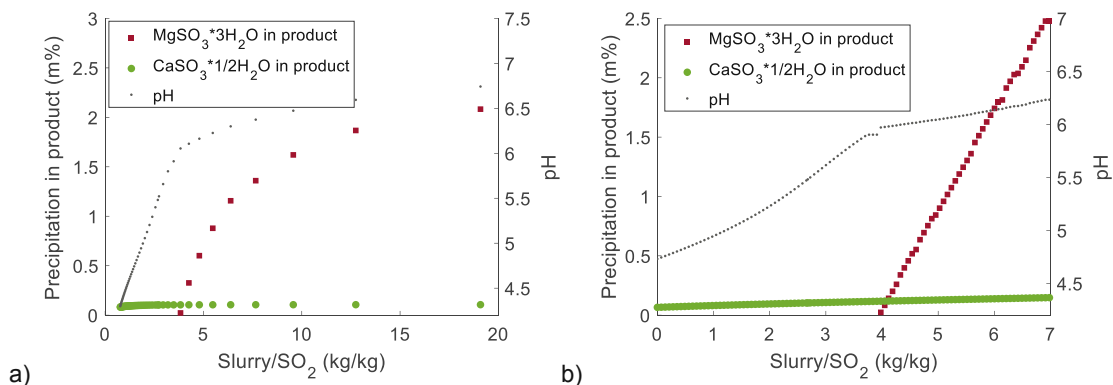


Figure 4: Precipitation in product as a function of the mass flow ratio $\text{Slurry}/\text{SO}_2$; (a) Varying of SO_2 input; (b) Varying of slurry input ($T = 68 \text{ }^\circ\text{C}$, $\dot{m}_{\text{Gas}0} = 374,000 \text{ kg/h}$, $\dot{m}_{\text{Recycle}} = 83,000 \text{ kg/h}$, venturi efficiency = 0.55)

The ratio was varied once by changing the SO_2 input and once by changing the slurry input. Following the Eqs(2) and (3), excess $\text{Mg}(\text{OH})_2$ in the system leads to an increased formation of MgSO_3 . The model reports that at a ratio higher than 4, the solubility limit is exceeded and MgSO_3 precipitates as trihydrate. The start of the precipitation can also be recognized by the inflection point of the slope of pH value in the product. This point is at a pH value of around 5.7 to 6.

4. Conclusions

The simulation showed promising results when compared with industrial measurement data. The performed analyses showed the importance to not only consider removal efficiency but also potential solid precipitation when designing wet flue gas desulfurization systems. The model reports CaSO_3 hemihydrate as precipitated solid in the product under the analyzed conditions. The precipitation of MgSO_3 trihydrate was reported when exceeding a temperature of 78 °C or a slurry/ SO_2 ratio of higher than around 4. $\text{Mg}(\text{OH})_2$ was reported when exceeding a pH value of 8 in the system. Those findings correspond to solubility reports found in literature. The model describes the solids occurring in the product. In a real system, local solubility exceedance can occur and lead to depositions. While the model does not depict those local concentration differences, it gives a good indication of key parameters influencing the precipitation in the system and provides a qualitative assessment of those influencing factors. Based on the performed analyses, it is recommended to ensure temperatures below 78 °C and a slurry/ SO_2 ratio of lower 4 when using a magnesium hydroxide slurry. Furthermore, it is recommended to prevent exceeding a pH value of 8 to limit precipitation issues in the system. For a further evaluation of those findings, measurements using infrared spectroscopy are recommended to identify the solids and to determine the ratio of SO_3^{2-} and HSO_3^- in the liquid product.

Acknowledgements

This work was financially supported by the Competence Center CHASE GmbH. CHASE Competence Center is subsidized in the frame of COMET – Competence Centers for Excellent Technologies by BMVIT, BMWFW, Wirtschaftsagentur Wien, State of Upper Austria and its scientific partners. The COMET program is handled by FFG. The support by the project partner Sappi Papier Holding GmbH is greatly acknowledged.

References

- Hudson J. L., Erwin, J., Catipovic N. M. 1979, Kinetics of Sulfur Dioxide Oxidation in Aqueous Solution, In Interagency Energy-Environment Research and Development series EPA-600/7-79-030 (EPA-600/7-79-030).
- Liu X., Liao C., Le L., Gao H., Zhou J., Feng Z., Lin Z., 2020, Research progress in the environmental application of magnesium hydroxide nanomaterials. In *Surfaces and Interfaces* 21, p. 100701. DOI: 10.1016/j.surfin.2020.100701.
- Marocco L., 2010, Modeling of the fluid dynamics and SO_2 absorption in a gas–liquid reactor. In *Chemical Engineering Journal* 162 (1), pp. 217–226. DOI: 10.1016/j.cej.2010.05.033.
- Ozyuguran A., Ersoy-Mericboyu A., 2010, Flue Gas Desulfurization by Limestone and Hydrated Lime Slurries. In 19, 125–130. DOI: 10.3303/CET1019021.
- Scholz F., Kahlert H., 2015, The calculation of the solubility of metal hydroxides, oxide-hydroxides, and oxides, and their visualisation in logarithmic diagrams. In *ChemTexts* 1 (1). DOI: 10.1007/s40828-015-0006-0.
- Si T., Wang C., Yan X., Zhang Y., Ren Y., Hu J., Anthony E. J., 2019, Simultaneous removal of SO_2 and NO_x by a new combined spray-and-scattered-bubble technology based on preozonation: From lab scale to pilot scale. In *Applied Energy* 242, 1528–1538. DOI: 10.1016/j.apenergy.2019.03.186.
- Steindl M., Röder T., Simharl R., Harasek M., Friedl A., Sixta H., 2005, Online Raman monitoring of the phase transition of magnesium sulphite hydrate. In *Chemical Engineering and Processing: Process Intensification* 44 (4), 471–475. DOI: 10.1016/j.cep.2004.06.011.
- Steindl M., Wolfinger M. G., Friedl A., Weber H. K., Sixta H., 2008, Modelling of the Lenzing SO_2 recovery process and validation with plant data. In *Journal of Cleaner Production* 16 (2), 208–214. DOI: 10.1016/j.jclepro.2006.08.027.
- Weiß B. D., Harasek M., 2021, Solubility Data of Potential Salts in the $\text{MgO-CaO-SO}_2\text{-H}_2\text{O-O}_2$ System for Process Modeling. In *Processes* 9 (1), p. 50. DOI: 10.3390/pr9010050.
- Zidar M., Golob J., Veber M., Vlachy V., 1997, Absorption of SO_2 into Aqueous Solutions. 2. Gas–Liquid Equilibrium of the $\text{MgO-SO}_2\text{-H}_2\text{O}$ System and Graphical Presentation of Operation Lines in an Equilibrium Diagram. In *Industrial & Engineering Chemistry Research* 36 (10), 4342–4346.
- Zou Y., Liu X., Zhu T., Tian M., Cai M., Zhao Z., Wu H., 2019, Simultaneous Removal of NO_x and SO_2 by MgO Combined with O_3 Oxidation: The Influencing Factors and O_3 Consumption Distributions. In *ACS Omega* 4 (25), 21091–21099. DOI: 10.1021/acsomega.9b02502.

Conference Paper

Die approbierte gedruckte Originalversion dieser Dissertation ist an der TU Wien Bibliothek verfügbar.
The approved original version of this doctoral thesis is available in print at TU Wien Bibliothek.

Multistep SO₂ absorption – Making process design choices based on process simulation

B.D.Weiß^{1, 2,*}, B. Haddadi², M.Harasek²

1: Competence Center CHASE GmbH, Ghegastraße 3, 1030 Vienna, Austria

2: Thermal Process Engineering - Computational Fluid Dynamics, Institute of Chemical, Environmental & Bioscience Engineering, TU Wien, Getreidemarkt 9, 1060 Vienna, Austria

*Corresponding author: barbara.weiss@tuwien.ac.at

Keywords: Flue gas treatment, Process optimization, Precipitation, Process design, Pulp industry, Chemical Recovery, Mg(OH)₂

Research field: Process simulation

Abstract

This study proposes two different process designs of a multistep SO₂ absorption process using an Mg(OH)₂ slurry. The first design aims to absorb as much SO₂ as possible in as few steps as necessary until a target SO₂ content in the exhaust gas is reached. The second design focuses on reaching the target SO₂ content in the exhaust gas and minimizing the chemical loss due to precipitation in the system. The process designs were designed and calculated using the process simulation environment of Aspen Plus[®] V10. The results show that the target SO₂ limit is reached after four absorption steps for the first process design. However, the precipitation loss makes up almost 20 wt% based on the product output. The second design requires eight absorption steps to reach the target SO₂ limit in the exhaust gas. However, the precipitation loss can be reduced to 5 wt% based on the product output. The results suggest that minimizing precipitation in the system can improve material process performance.

Introduction

The absorption of SO₂ with a magnesium-based absorptive slurry is a commonly used technology to reduce SO₂ emissions from SO₂-containing exhaust gas [1]. In magnesium bisulfite (Mg(HSO₃)₂) based pulp processes, the chemisorption of SO₂ leads to the recovery of the cooking liquor Mg(HSO₃)₂ following Equation (1) and (2):

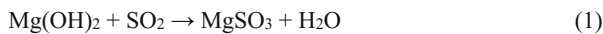


Figure 7 shows the simplified process loop of the chemical recovery in a magnesium bisulfite-based pulping process.

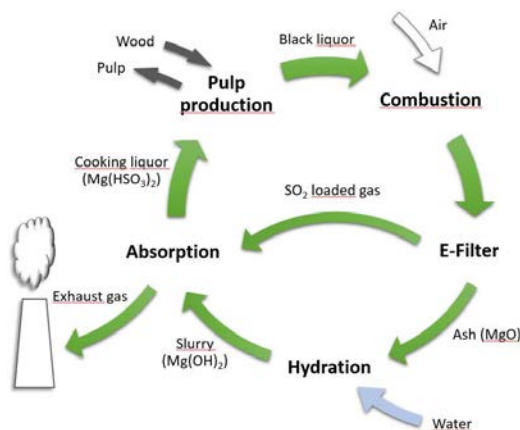


Figure 7: Simplified process loop of the chemical recovery of a magnesium bisulfite pulping process

The absorption of SO₂ with Mg(OH)₂ is a crucial step in recovering the cooking liquor. The chemical reaction system during absorption is complex and consists of equilibrium, dissociation, and precipitation reactions. Previous studies identified CaSO₃ hemihydrate, Ca(OH)₂, Mg(OH)₂, MgSO₃ tri-, and hexahydrate as potential salts precipitating in the system under usual absorption conditions [2], [3]. While reactions leading to the formation of Mg(HSO₃)₂ (see Equation (1) and (2)) are wanted, precipitation reactions are highly unwanted. Precipitation in the system leads to deposits on the process equipment, blockage of pipes, and subsequently to chemical loss as the salts have to be washed out in a regular cleaning step and are not recycled in the recovery process [4]. This challenges the efficiency of the process and increases its ecological footprint. Therefore, this study suggests that it is crucial to not only focus on SO₂ removal efficiency but also to include the issue of precipitation in process simulations to design an optimized process for absorption.

Figure 8 summarizes the input and output streams of the process.

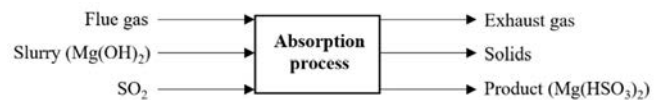


Figure 8: Input and output streams of the absorption process

Solids, which translate into chemical loss, are considered as separated outlet stream. To use the liquid product as cooking liquor, a pH value of around 4.5 is required for the magnesium bisulfate pulping process [5]. To meet this pH value, additional SO₂ has to be added to the liquid product depending on the pH value after absorption. Figure 8 includes this required SO₂ as an input stream.

The following investigates two different process design approaches and proposes an optimized process design based on process simulations.

Methods

The process was modeled as steady-state process in Aspen Plus[®] V10 using the Elec-NRTL property method. The chemical system includes all relevant equilibrium, dissociation, and precipitation reactions. The model covers the precipitation of CaSO₃ hemihydrate, Ca(OH)₂, Mg(OH)₂, MgSO₃ tri- and hexahydrate.

Figure 9 shows the flowsheet of the process as it was implemented in AspenPlus.

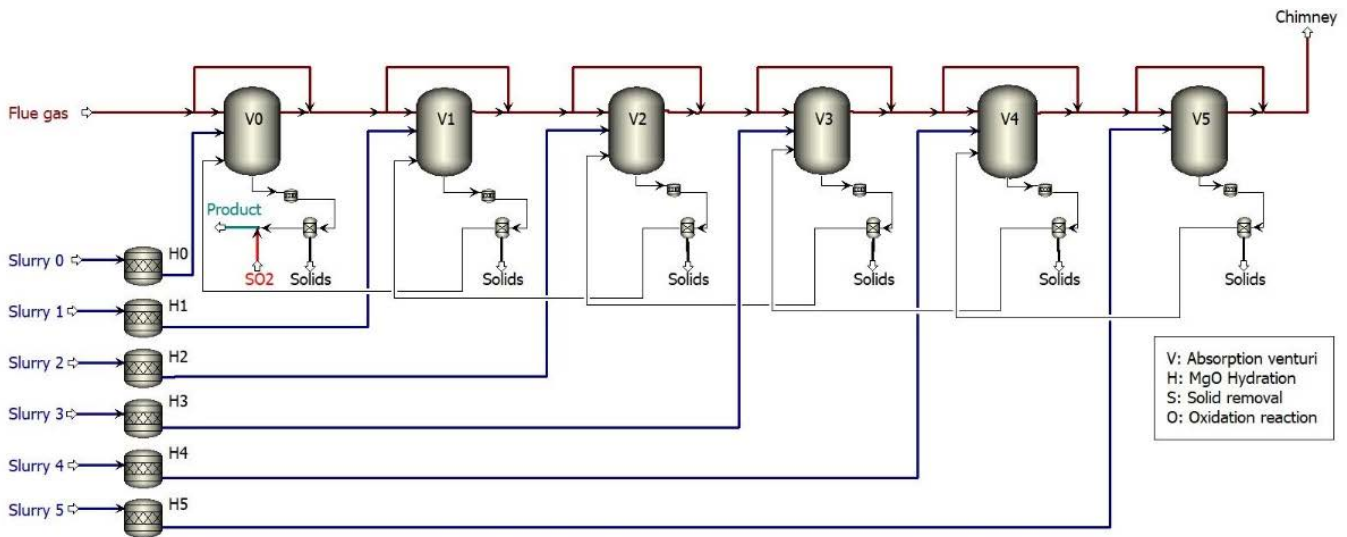


Figure 9: Process flowsheet of multi-step SO₂ absorption (exemplary six steps)

The figure shows exemplary a 6-step absorption process.

Input streams

The flue gas has typical properties for a flue gas coming from a combustion unit in the pulp industry. It enters the absorption process saturated with water and at 68 °C and a pressure of 1.077 bar. Table 5 summarizes the flue gas composition.

Table 5: Flue gas composition in mass-% (wet basis)

H ₂ O	N ₂	CO ₂	O ₂	SO ₂	NO
17.49	58.36	15.81	5.04	1.94	1.36

The total flue gas flow was set to be 100 000 kg/h. The slurry consists of 91.35 wt% H₂O, 8.5 wt% MgO, and 0.15 wt% CaO.

Besides flue gas and slurry, there is also extra SO₂ entering the process. The liquid product, after absorption, needs to have a pH value of 4.5 to be used as cooking liquor in the bisulfite pulping process [5]. Depending on the pH value of the liquid output of the absorption process, extra SO₂ needs to be added to reach a pH value of 4.5. The flow of the extra SO₂ was adjusted to reach this pH value by a design specification.

Output streams

The SO₂ content in the exhaust must not exceed a specific SO₂ limit. In this study, a target content of 450 mg/Nm³ SO₂ was set following the suggestions given by the Austrian Federal Environmental Agency [6]. It needs to be considered that this limit is referred to dry exhaust gas with an oxygen content of 5 %. Equation (3) describes the conversion from the actual O₂ content in the exhaust gas to the reference O₂ content of 5 %:

$$SO_2 \left(\frac{mg}{Nm^3}, 5\% O_2 \right) = \frac{21\% - 5\%}{21\% - O_2(\%)} * SO_2 \left(\frac{mg}{Nm^3} \right) \quad (3)$$

The liquid product stream is set to have a pH value of 4.5. At each absorption unit, a solid stream exits the process representing the loss due to precipitation.

Process units

Stoichiometric reactors cover the hydration of MgO and CaO in the slurry input. The implemented reactors consider complete hydration

of MgO and CaO to Mg(OH)₂ and Ca(OH)₂.

The absorption units are implemented as flash units, which calculate the phase and chemical equilibrium between all entering streams. An industrial absorption unit does not reach equilibrium, with the physical solubility of SO₂ being the limiting process in the system (Marocco 2010). The absorption efficiency in each absorption unit was set to 70 % using a bypass stream for the flue gas. It is assumed that 30 wt% of the flue gas is not reacting with the entering liquid streams but passing through to the next unit without interacting with the entering liquid stream.

After each absorption unit, a stoichiometric reactor covers the oxidation of SO₃⁻ to SO₄⁻ with O₂ in the liquid outlet. The fractional conversion of O₂ was set to 1 due to the fast kinetics of the oxidation reaction [7].

A subsequent split unit separates the precipitates from the liquid stream. All salts present after each absorption stream are removed from the liquid stream and discharged from the process. These solids make up the chemical loss, which occurs during an absorption process due to precipitation in the system.

The described flowsheet was used to design two different process approaches. Sensitivity analyses varying the slurry input of each absorption unit allowed to find optimized process conditions.

Process design maximized absorption

The first design aims to minimize the SO₂ in the exhaust gas with as few absorption units as possible. Sensitivity analyses varying the slurry input streams allowed finding the highest absorption rate of each unit without adding excess slurry. The flowsheet was systematically extended with absorption units until the target SO₂ content in the exhaust gas was reached.

Process design minimized precipitation

The second design aims to minimize precipitation in the system while reducing the SO₂ content in the exhaust until the target SO₂ content. To find the optimized slurry input, sensitivity analyses were performed by varying the slurry input. The optimized slurry input was defined as the highest slurry input possible, where the SO₂ drop in the gas phase was still high and the solid increase low. This point can be identified by plotting the ratio (y) of SO₂ drop in the gas phase

and solid increase over the slurry input following Equation (4):

$$y = \frac{|\Delta SO_2 \text{ in gas phase}|}{\Delta \text{slurry input}} * \frac{\Delta \text{slurry input}}{\Delta \text{solids}} \quad (4)$$

The flowsheet was systematically extended with absorption units until the target SO₂ content in the exhaust gas was reached.

Evaluation and comparison of both process designs

Finally, the process designs were compared and evaluated using the following parameters:

- Number of required absorption units to reach a target SO₂ content in the exhaust gas
- Material loss due to precipitation (kg)
- The ratio of the amount of material loss due to precipitations and final liquid product (%)
- Amount of extra SO₂ required to reach a pH value in the liquid product stream of 4.5
- The ratio between the amount of liquid product and overall slurry input (kg/kg)

Results and Discussion

Figure 10 shows the result of the sensitivity analysis varying the slurry input for the first absorption step (V0). The following describes the choice of operating point for the first absorption step exemplary.

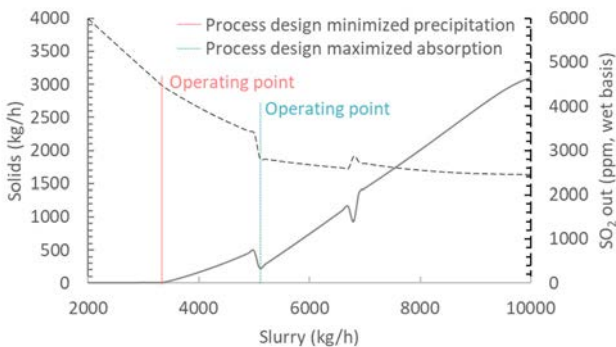


Figure 10: Solid precipitations and SO₂ content in the exhaust gas over slurry input for the first absorption step (V0)

The figure shows the chosen operating points for the first absorption step for each process design. The SO₂ decrease in the exhaust gas flattens significantly at a slurry input of 5100 kg/h. Higher slurry input does not improve the absorption of SO₂ anymore. Therefore, the operating point for the process design maximized absorption is set at a slurry input of 5100 kg/h. The optimized operating point for a process design that aims for minimized precipitations is at a slurry input of 3400 kg/h. At a lower slurry input, almost no precipitation occurs. Only around 9 kg/h precipitates form. Looking closer at the composition of the solid stream shows that the solid stream at a lower slurry input consists mainly of CaSO₃ Hemihydrate. At higher slurry input, MgSO₃ Trihydrate starts precipitating, indicating that the solubility limit of MgSO₃ is exceeded. This point can be clearly identified in Figure 11. Figure 11 shows the ratio between SO₂ decrease and solid increase (y) following Equation (4) over the slurry input.

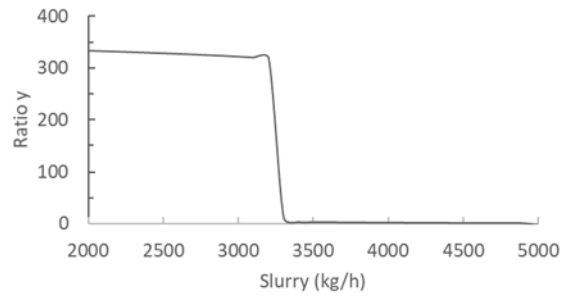


Figure 11: Ratio y (following Equation (4)) over slurry input for the first absorption step (V0)

The ratio drops significantly at a slurry input of 3400 kg/h. A higher slurry input would drastically increase the system's precipitation, making this operating point the optimized point for the process design minimized precipitation.

The slurry input for the subsequent absorption steps is chosen following the same approach until the target SO₂ content in the exhaust gas is reached. Figure 12 summarizes the resulting slurry input for each absorption step for both designs. Fehler! Verweisquelle konnte nicht gefunden werden. shows the SO₂ content in the exhaust gas after each absorption step.

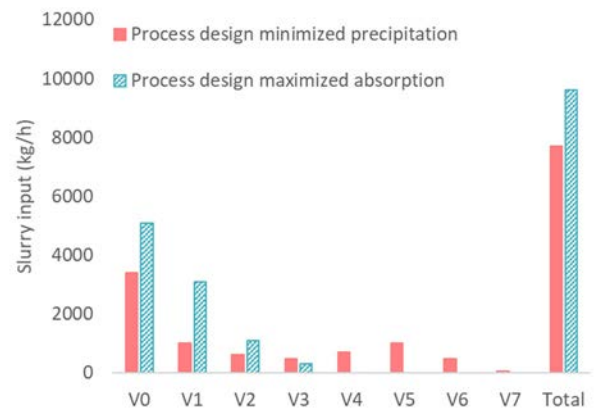


Figure 12: Slurry input for each absorption step and total slurry input for both process designs

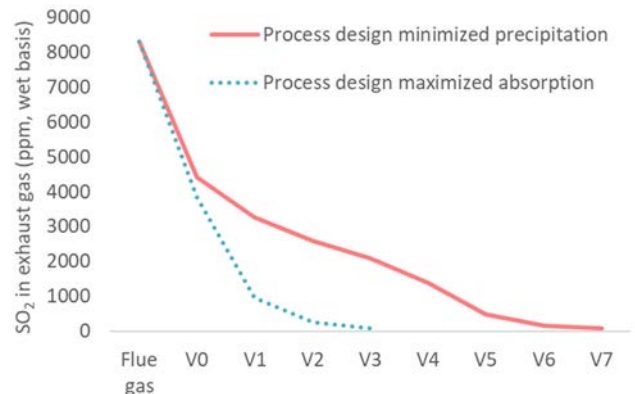


Figure 13: SO₂ content in the exhaust gas after each absorption step for both process designs

Figure 13 shows that the process design maximized absorption requires four absorption steps to reach the target SO₂ content. The process design minimized precipitation requires eight absorption steps. Both designs reach an SO₂ content in the exhaust gas of around

80 ppm on a wet basis. This corresponds to an SO₂ content of around 350 mg/Nm³, referred to dry exhaust gas with an oxygen content of 5%. Although the process design minimized precipitations requires more absorption steps, it requires less overall slurry input to reach the target SO₂ level (Figure 12). While the process design maximized absorption requires a total slurry input of 9700 kg/h, the process design minimized precipitation requires only a total slurry input of 7700 kg/h. Minimizing precipitations can therefore lower the slurry demand by 20%. The lower chemical loss due to precipitation explains the lower slurry demand. Figure 14 shows the solid precipitation after each absorption step and the total solid precipitation for both process designs.

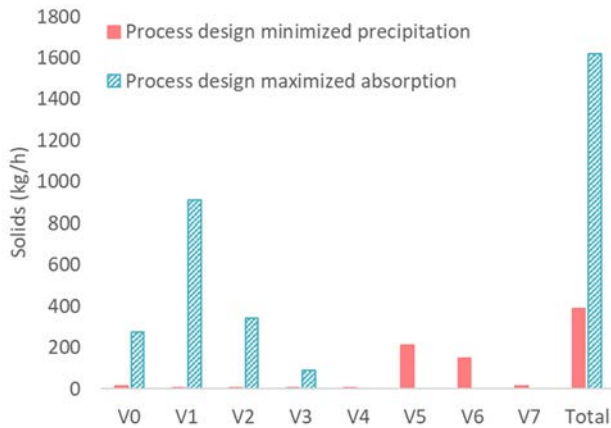


Figure 14: Solid removal after each absorption step and the total solid removal for both process designs

1620 kg/h solids precipitate in the process design maximized absorption. In the process design minimized precipitation only 390 kg/h solids precipitate. Precipitation is therefore minimized by around 75%.

Considering the material input and product output, minimization of precipitation results in an overall better process performance as it reduces chemical loss. This can be illustrated by giving the ratio of final product, which serves as cooking liquor, and slurry input. The amount of chemical loss due to precipitation compared to the product output is given by the ratio of solids and the final product (Figure 15).

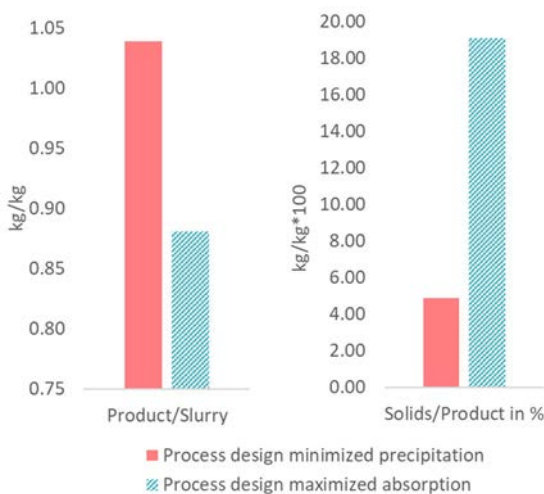


Figure 15: left: Ratio between product and slurry demand; right: Ratio between solids and product expressed in percentage

When designing the process following the minimized precipitation design, the product output is higher than the slurry input, leading to

a ratio of 1.04. When designing the process following the maximized absorption design, the product output is lower than the slurry input, leading to a ratio of 0.88. The ratio between solids and final product output shows that without considering the minimization of precipitations, the amount of chemical loss in the system due to precipitations makes up almost 20% of the amount of the final product.

But slurry input is not the only material input required. Depending on the pH value of the liquid outlet of the absorption process, SO₂ needs to be added to reach the target pH value of the cooking liquor of 4.5. Figure 16 shows the pH value of the liquid after the absorption and the SO₂ needed to reach the target pH value of 4.5 for both process designs.

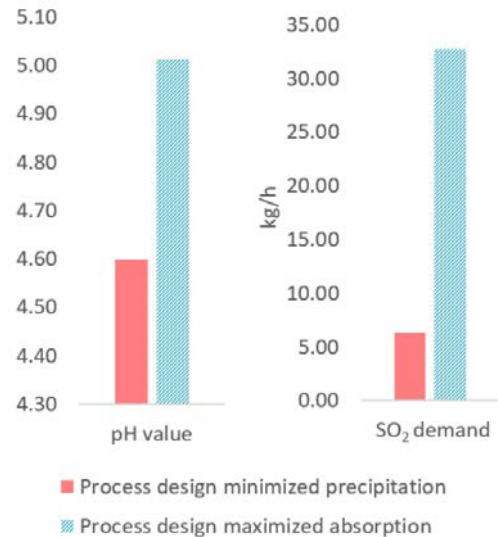


Figure 16: left: pH value of liquid after absorption before SO₂ addition; right: SO₂ demand to reach target pH of 4.5

The minimized precipitation design leads to around five times lower SO₂ demand to reach the target pH value of 4.5. The SO₂ demand is 6.3 kg/h, while the process design maximized absorption requires the addition of 32.8 kg/h SO₂.

Conclusion

The results show that heavy precipitation occurs in the first three absorption steps when designing the process to reach maximized absorption. By lowering the absorption in each step, precipitation can be significantly reduced. However, more absorption steps are necessary to reach the target SO₂ content in the exhaust gas. The process design minimized precipitation results in a five times lower SO₂ demand and a 20% lower slurry demand. This study only compares the two process designs regarding slurry input, SO₂ input, and chemical loss due to precipitation. It does not include the chemicals required to wash out the solid deposits during maintenance intervals. High precipitations also lead to a high washing liquid demand.

The study suggests that a process that aims to minimize precipitations performs more material efficiently due to an overall lower chemical demand and lower chemical loss in the process. The performed analyses show that including unwanted precipitations in process simulation experiments is crucial to find optimized absorption conditions. To make a final judgment about the economic and ecologic advantages of installing extra absorption units to reduce precipitation, a comprehensive case study is necessary, which takes a cradle to grave or cradle to cradle approach for the process, the

process equipment, process chemicals and the energy demand into account.

Acknowledgment

The authors gratefully acknowledge the support by the project partner Sappi Papier Holding GmbH.

References

- [1] X. Liu *et al.*, "Research progress in the environmental application of magnesium hydroxide nanomaterials," *Surfaces and Interfaces*, vol. 21, p. 100701, 2020, doi: 10.1016/j.surfin.2020.100701.
- [2] B. D. Weiß and M. Harasek, "Solubility Data of Potential Salts in the MgO-CaO-SO₂-H₂O-O₂ System for Process Modeling," *Processes*, vol. 9, no. 1, p. 50, 2021, doi: 10.3390/pr9010050.
- [3] B. D. Weiß, W. Fuchs, and M. Harasek, "Finding Optimized Process Conditions to Minimize Precipitations in an SO₂ Absorption Process Using Thermodynamic Process Simulation," *Chem Eng Trans*, vol. 88, pp. 535–540, Nov. 2021, doi: 10.3303/CET2188089.
- [4] M. Steindl, T. Röder, R. Simharl, M. Harasek, A. Friedl, and H. Sixta, "Online Raman monitoring of the phase transition of magnesium sulphite hydrate," *Chemical Engineering and Processing: Process Intensification*, vol. 44, no. 4, pp. 471–475, 2005, doi: 10.1016/j.cep.2004.06.011.
- [5] P. Bajpai, "Pulping Fundamentals," *Biermann's Handbook of Pulp and Paper*, pp. 295–351, Jan. 2018, doi: 10.1016/B978-0-12-814240-0.00012-4.
- [6] J. Stubenvoll, E. Holzerbauer, S. Böhmer, T. Krutzler, and T. Janhsen, "TECHNISCHE MASSNAHMEN ZUR MINDERUNG DER STAUB-UND NO X-EMISSIONEN BEI WIRBELSCHICHT-UND LAUGENVERBRENNUNGSKESSELN," 2007, Accessed: Feb. 13, 2023. [Online]. Available: <http://www.umweltbundesamt.at/>
- [7] J. L. Hudson, J. Erwin, and N. M. Catipovic, "Kinetics of Sulfur Dioxide Oxidation in Aqueous Solution," *Interagency Energy-Environment Research and Development series*, vol. EPA-600/7-79-030, no. EPA-600/7-79-030, 1979.

Submitted Journal Paper IV

Die approbierte gedruckte Originalversion dieser Dissertation ist an der TU Wien Bibliothek verfügbar.
The approved original version of this doctoral thesis is available in print at TU Wien Bibliothek.

Effect of Spraying Characteristics on Combustion of Red Liquor – Virtual Experiments using CFD Simulation

Barbara D. Weiß^{1,2*}, Eva-Maria Wartha², Christian Jordan², Thomas Ladinek³, Michael Harasek², Bahram Haddadi¹

¹Competence Center CHASE GmbH, Ghegastraße 3, 1030 Vienna, Austria

²Institute of Chemical, Environmental & Bioscience Engineering, TU Wien, Getreidemarkt 9, 1060 Vienna, Austria

³Sappi Austria Produktions-GmbH & Co. KG, Sappi Europe, Brucker Strasse 21, 8101 Gratkorn, Austria

*Correspondence: barbara.weiss@tuwien.ac.at

Abstract

Red liquor combustion is a crucial step in the chemical recovery process within the pulp and paper industry, involving multiple stages such as combustion, MgO hydration from ash, and SO₂ absorption using recovered magnesium hydroxide. The formed magnesium bisulfite is then recycled as cooking liquor. The research aims to analyze how different red liquor spraying characteristics affect combustion time, guiding recommendations for optimal spraying characteristics to achieve faster combustion using computational fluid dynamics (CFD).

Red liquor combustion is simulated in the open-source environment OpenFOAM[®], employing Eulerian-Lagrangian coupling simulations, treating red liquor droplets as Lagrangian particles. One-step devolatilization and combustion kinetics are derived from performed non-isothermal thermogravimetric analyses (TGA) and implemented into the model. An industrial red liquor combustion vessel served as a reference case. Through virtual experiments, we explore the impact of spray angle (15° and 30°), droplet size (2 mm and 3 mm), and spray type (fullcone vs. hollowcone) on combustion efficiency. The performed simulations indicate that the combustion time can be reduced by approximately 30 % by reducing the characteristic particle diameter from 3 mm to 2 mm. Furthermore, hollowcone spraying revealed faster combustion times than fullcone spraying. The fastest combustion time was achieved with a characteristic particle size of 2mm, a spraying angle of 30°, and using a hollowcone spray type.

Keywords: Fuel spraying, Lagrangian particle combustion, Pulping liquor, Recovery boiler, CFD Simulation

1 Introduction

The combustion of spent pulping liquor is a crucial part of the chemical recovery process in the pulp and paper industry. Among the sulfite-based pulping processes, magnesium bisulfite pulping is dominant due to its potential for almost complete chemical recovery [1]. During the combustion of magnesium bisulfite spent liquor, also called red liquor, MgO is recovered in the ash. Sulfur is mainly oxidized to SO₂, resulting in an SO₂-loaded combustion gas. The recovered MgO is washed and hydrated to Mg(OH)₂, which subsequently serves as an absorbent in a multi-stage SO₂ absorption process. During the absorption, SO₂ and Mg(OH)₂ form magnesium bisulfite, which can then be reintroduced as pulping liquor. Such chemical recovery minimizes the usage of fresh chemicals, thus lowering the process' environmental footprint. However, the combustion of red liquor affects the chemical usage in the pulping process beyond the chemical recovery, as ineffective combustion leads to soot formation, which is carried through the whole chemical recovery process to the pulp, leading to the coloration of the pulp, thus causing an increased demand of bleaching agents. Figure 1 visualizes the journey of soot in chemical recovery in a simplified manner.

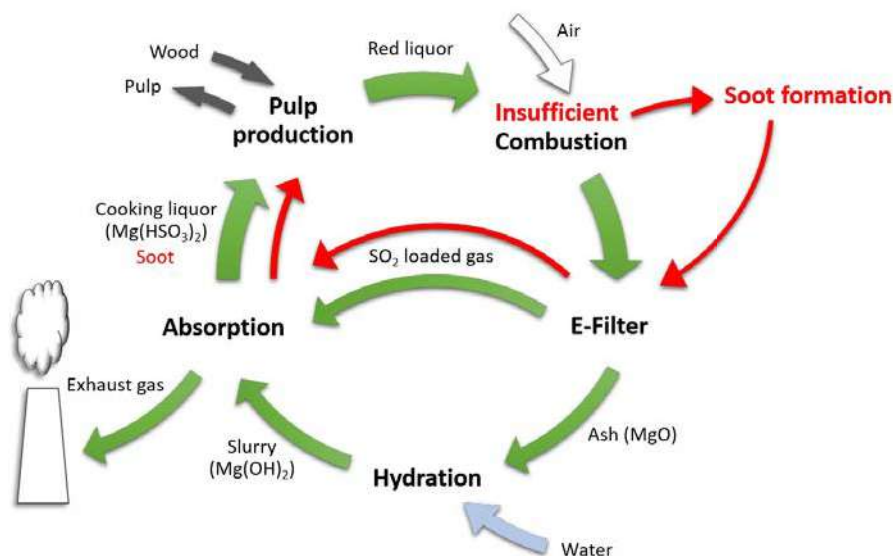


Figure 1: Simplified scheme of the chemical recovery when soot forms during combustion

Improving combustion has, therefore, a dual effect: it enhances the efficiency of the pulp recovery process and reduces the necessity of bleaching agents, resulting in an overall reduced environmental footprint and increased economic viability.

Due to its large inorganic content and high water content, spent pulping liquor has a very low heating value of 12-15 MJ/kg compared to other industrial fuels (e.g., heating oil: 41 MJ/kg), making its effective combustion a unique challenge [2]. Red liquor is sprayed into the furnace with a water content of

around 30 to 40 wt%. The spraying characteristics of the fuel highly influence the combustion efficiency inside the furnace. Optimizing the spraying behavior into a furnace can significantly enhance the combustion efficiency of existing furnaces without the necessity of redesigning the furnace. This study aims to investigate the effect of spraying characteristics on the combustion speed of fuel droplets inside an industrial-scale combustion vessel via computational fluid dynamics (CFD) simulations. While the used reference case is tailored to an industrial-scale combustion vessel of red liquor, the simulation approach and the results can also be expanded to other fuels with high water content and large droplet spraying (mm).

A great part of research focuses on studying the spraying and its influence on the combustion of very fine droplets (μm) [3–5]. Droplet sizes for the combustion of spent pulping liquor are typically in the scale of mm. Although the pulp and paper industry accounts for 1.1 % of direct global industrial combustion and process CO_2 emissions [6,7], and the combustion of spent pulping liquor poses a particular challenge due to its mentioned characteristics, academic research on optimizing the design of spent pulping liquor combustion furnaces and its fuel spraying are scarce. Horton et al. studied in 1992 the effect of spraying on the combustion of black liquor using CFD simulation [8]. Laitinen et al. performed CFD simulations of a black liquor boiler to study the dispersion of sprayed droplets and the secondary air supply system without implementing combustion models [9]. Black liquor refers to the liquor from an alkaline sulfate-based pulping process (Kraft process), while red liquor refers to the liquor from sulfite-based pulp processes. However, to our knowledge, no study has been focused on simulating the combustion of red liquor and deriving recommendations on optimized fuel spraying for such challenging fuels, making this a novel study in the field of applied CFD.

In this study, we apply one-step combustion models for the combustion of red liquor and perform a comparative study on the effect of spraying behavior on droplet combustion time. To model the combustion, we follow an Eulerian-Lagrangian approach, which allows us to track the fuel droplets inside the furnace. A two-way coupling enables the exchange of momentum, energy, and mass between the discrete fuel droplets and the continuous phase. The Eulerian-Lagrangian method is a widely recognized approach to describe liquid fuel spraying [10].

The CFD simulation setup allows us to run experiments in a virtual environment. By varying spraying characteristics such as spraying angle, droplet size, and spray type, we are predicting which factor is most influential in speeding up combustion inside the vessel and which spraying behavior is the most promising regarding combustion time.

2 Material and Methods

In this chapter, we introduce the methods used for our study. Section 2.1 provides the governing equations of the applied Eulerian-Lagrangian approach. In section 2.2, we introduce the used phase change and reaction models. Finally, we present the simulation setup on which the developed workflow was tested, including the simulation geometry, the computational mesh, and the boundary conditions. This chapter closes by summarizing the performed virtual experiments in section 2.4.

2.1 Computational Fluid Dynamics (CFD)

The simulations are performed in the open-source simulation environment OpenFOAM® version 9 using the solver *reactingFoam*. The combustion vessel operates with stable conditions, allowing the simulations to be performed in a steady state. Figure 2 visualizes the concept of the applied Eulerian-Lagrangian approach. Although describing Lagrangian particles can be computationally intensive, this method's advantage lies in its ability to track specific properties of individual particles.

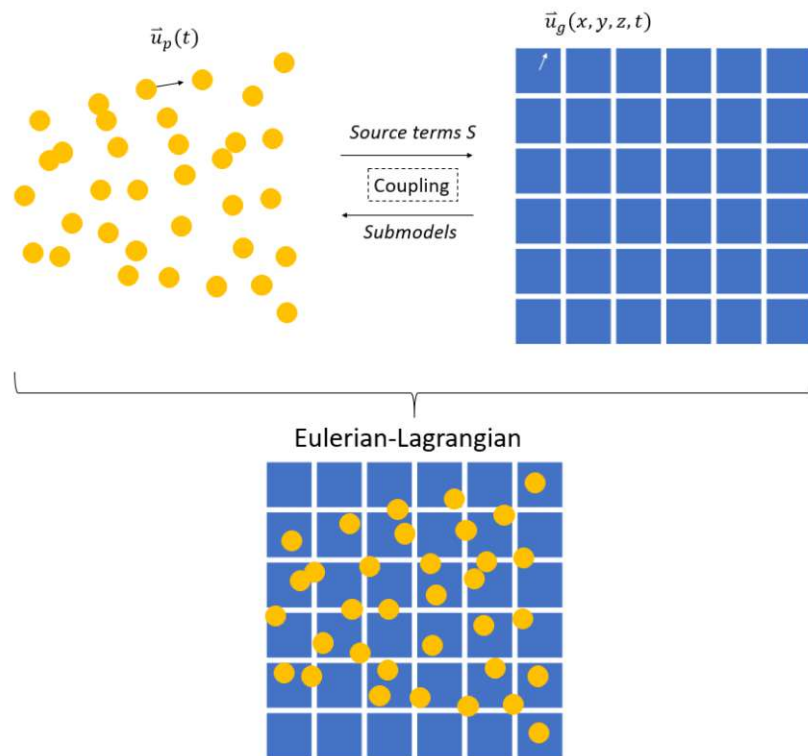


Figure 2: Top left: Lagrangian particles; Top right: Eulerian flow; Bottom: Eulerian-Lagrangian approach (Visualization inspired by Hirche et al. [11])

The gas phase is described as Eulerian phase. The liquid fuel droplets are modeled as wet solid point centers of mass with constant volume and described as Lagrangian particles. The coupling between the Eulerian phase and the Lagrangian particles is realized as a two-way coupling. The influence of the

fuel droplets (Lagrangian particles) on the gas phase (Eulerian phase) is modeled employing source terms. The influence of the gas phase on the fuel droplets is modeled using submodels. To save computational time, particles are grouped into representative parcels, each comprising numerous particles with the same characteristics that are tracked and solved together.

The $k - \varepsilon$ model is used to account for turbulence with the default model coefficients [12,13]. The $k - \varepsilon$ model is commonly used in the simulation of industrial furnaces in OpenFOAM® [14,15]. k represents the turbulent kinetic energy, and ε the eddy dissipation rate. The eddy dissipation rate gives the rate at which turbulent kinetic energy transforms into internal thermal energy due to viscous effects. Radiation was calculated using the P1 model, a commonly used radiation approximation for particle combustion processes, as implemented in OpenFOAM® [16]. The following describes the modeling of the Eulerian Flow and the Lagrangian Particles.

Eulerian Flow

The Eulerian flow is described employing the continuity equation, the momentum equation, the energy equation, and the species equation (Equation (1)-(3)).

The continuity equation with S_m being the source term for mass reads

$$\frac{\partial \rho_g}{\partial t} + \nabla \cdot (\rho_g U_g) = S_m \quad (1)$$

where ρ_g is the density, U_g is the velocity. S_m is resulting from reaction and phase change.

The Momentum equations for compressible fluids reads

$$\frac{\partial(\rho_g U_g)}{\partial t} + \nabla \cdot (\rho_g U_g U_g) - \nabla \cdot (\tau_g) = -\nabla p + \rho_g g + S_u \quad (2)$$

The equation includes viscous force with τ_g being the stress tensor. S_u describes the momentum source term resulting from interaction with the Lagrangian particles.

The energy equation includes diffusion with α_{eff} being the effective thermal diffusivity and reads

$$\frac{\partial(\rho_g(h + K))}{\partial t} + \nabla \cdot (\rho_g U_g(h + K)) - \nabla \cdot (\alpha_{eff} \nabla h) = \nabla p + \rho_g U_g \cdot g + S_h \quad (3)$$

h is the enthalpy, and K the kinetic energy. S_h is the energy source term resulting from the exchange with the Lagrangian particles.

To describe the multi-component nature of the flow, the species equation is applied with S_i being the species source term resulting from reaction and phase change. The species equation reads

$$\frac{\partial \rho_g Y_i}{\partial t} + \nabla \cdot (\rho_g U_g Y_i) - \nabla \cdot \left(\frac{\mu_{eff}}{Sc} \nabla (\rho_g Y_i) \right) = S_i \quad (4)$$

Y_i describes the mass fraction for species i , μ_{eff} the effective viscosity for species transport and Sc the Schmidt number. The last term represents the diffusion of the species' mass fraction.

Lagrangian Particles

Newton's second law of motion describes the movement of the Lagrangian particles. Drag force F_D , gravitational force F_g and lift force F_L are acting on the particle, leading to the following equation

$$\frac{d}{dt} (m_p U_p) = F_D + F_g + F_L \quad (5)$$

where m_p is the particle mass and U_p the particle velocity.

The drag force is calculated with the *sphereDrag* model from the OpenFOAM® library:

$$F_D = \frac{m_p}{U_g} \frac{3 \mu_g C_D Re_p}{4 \rho_p d_p^2} \quad (6)$$

μ_g is the dynamic viscosity and U_g the velocity of the carrier (gas phase) at the cell-occupying particle, ρ_p the particle mass density and d_p the particle diameter. The particle drag coefficient C_D is based on the empirical expression by Putnam [17]:

$$C_D = \frac{24}{Re_p} \left(1 + \frac{1}{6} Re_p^{\frac{2}{3}} \right) \text{ if } Re_p \leq 1000 \text{ and } C_D = 0.424 \text{ if } Re_p > 1000 \quad (7)$$

The lift force is calculated following:

$$F_L = m_p \frac{\rho_g}{\rho_p} \frac{3}{2\pi \sqrt{Re_w}} C_L (U_g - U_p) \times \omega \quad (8)$$

Where $\omega = \nabla \times U$ is the vorticity of the gas at particle location and $Re_w = \frac{\rho_g d_p^2 |\omega|}{\mu_g}$. The lift coefficient

C_L is based on the Saffman-Mei expression [18,19]:

$$C_L = 6.46 \left(1 - 0.3314 \sqrt{\frac{1 Re_w}{2 Re_p}} \right) e^{-0.1 Re_p} + 0.3314 \sqrt{\frac{1 Re_w}{2 Re_p}} \text{ if } Re_p < 40 \text{ and} \quad (9)$$

$$C_L = 6.46 \cdot 0.0524 \sqrt{\frac{1}{2} Re_w} \text{ if } Re_p \geq 40$$

A stochastic dispersion model is applied to account for perturbation of a particle due to turbulence [20]. The particle is perturbed by turbulence if the timestep is smaller than τ_{tur} :

$$\tau_{turb} = \min \left(\frac{k}{\varepsilon}, 0.16432 \frac{k^{1.5}}{\varepsilon U_{rel}} \right) \quad (10)$$

Where

$$U_{rel} = |U_p - U_g - U_{turb}| \quad (11)$$

With U_p being the particle velocity, U_g the gas phase velocity and U_{turb} the turbulent velocity.

The velocity undergoes perturbation in random direction

$$U_{turb} = \sqrt{\frac{2k}{3}} |N| d_v \quad (12)$$

where N is a random normal with mean 0 and standard deviation 1, and d_v a vector with $[a \cos(\theta), a \sin(\theta), u]$. a is random between 0 and 1, u random between -1 and 1, and θ random between 0 and 2π . The model is part of the standard OpenFOAM® library under the name *StochasticDispersionRAS*.

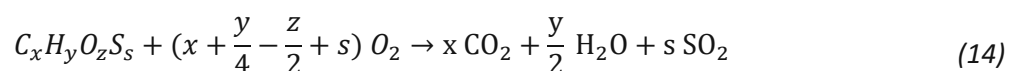
The gas-particle heat transfer is modeled using the empirical Nusselt correlation by Ranz-Marshall [21]:

$$Nu = 2 + 0.6Re_p^{\frac{1}{2}} Pr^{\frac{1}{3}} \quad (13)$$

2.2 Phase Change and Reactions

Phase change and reaction models are implemented to model the combustion of red liquor. Drying, devolatilization, and char combustion are the three main stages of red liquor combustion [2]. The fourth stage is smelt of ash, which is a slow process and disregarded in the performed simulation due to the short residence time of the fuel droplets in the furnace. Red liquor combustion is a complex reaction system during which organic matter is burnt and inorganic matter is recovered in the ash. In this study, a simplified combustion reaction system is implemented that summarizes the complex combustion system into four steps with two reactions:

1. Drying
2. Devolatilization
3. Volatile combustion in the gas phase:



4. Char combustion:



Figure 3 visualizes the combustion steps that are implemented in the simulations.

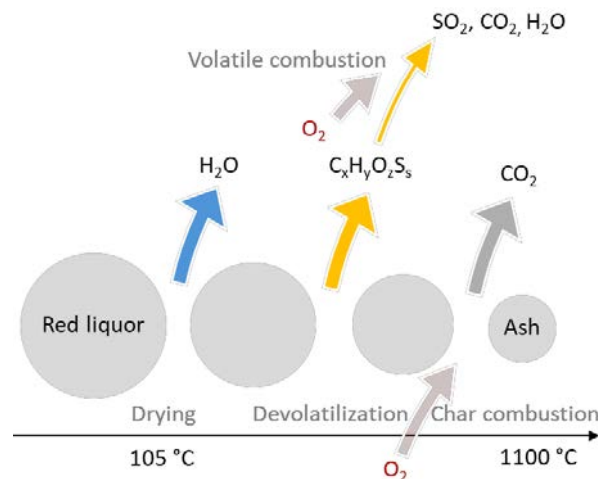


Figure 3: Visualization of implemented combustion steps

The stoichiometry of the gas phase reaction can be derived from the known elemental composition of red liquor. While several studies in literature study the kinetics of black liquor [22,23], the available studies on red liquor are scarce. The composition of red liquor, being highly specific, can introduce significant variations in the kinetics of reactions. Hence, we generated our own kinetics data tailored to our red liquor composition. For this purpose, thermogravimetric analyses were performed. The following section describes the conducted analyses and the implemented phase change and reaction models.

2.2.1 Thermogravimetric Analyses of Red Liquor

Non-isothermal thermogravimetric analyses (TGA) of red liquor were conducted to investigate its devolatilization and combustion behavior. The experiments were carried out using an STA 449 C Jupiter instrument manufactured by NETZSCH. TGA experiments were performed under two different gas environments: Nitrogen (N₂) and an oxidizing environment containing 21 vol% oxygen (O₂). The sample was dried by holding the temperature at 105 °C for 100 min. After drying, the heating rate was set to 15 K/min. The sample was heated to 1100 °C. During the experiments, the weight of the sample was recorded. From the recorded data, various parameters describing the devolatilization and combustion behavior are derived:

- Temperature at which devolatilization starts (T_{Devol})
- Amount of volatiles left when combustion starts (volatile residual coefficient)
- Kinetic data for devolatilization and char combustion

Figure 4 shows the temperature and mass loss referred to the dry basis over time from the TGA results.

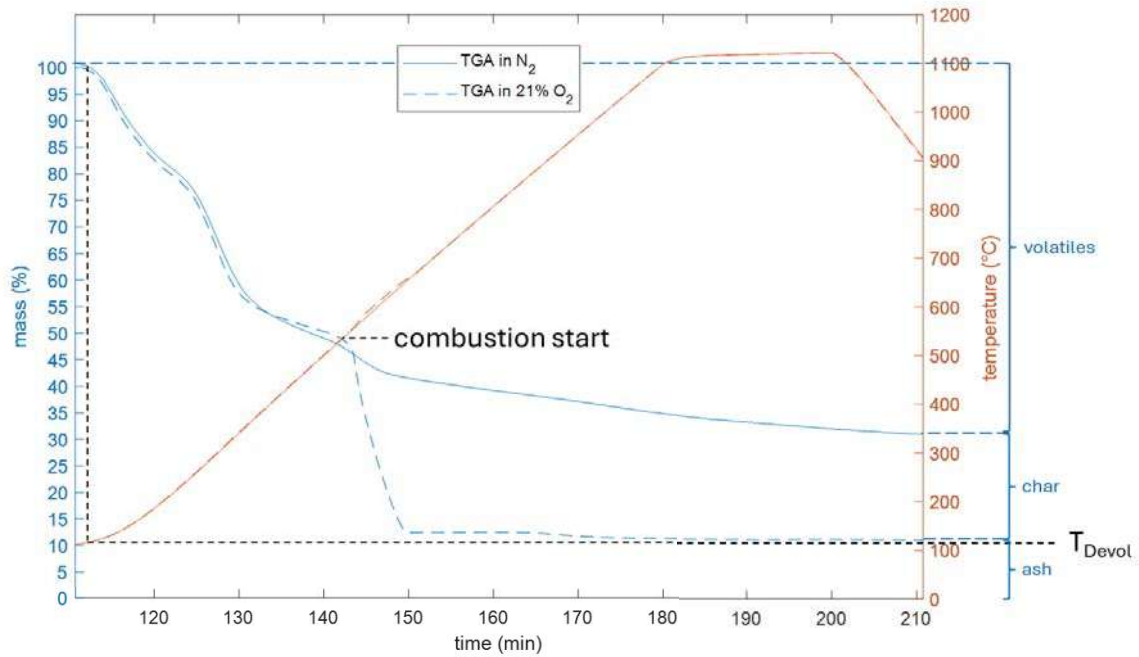


Figure 4: TGA result: Temperature and mass loss (wt% dry mass) over time in N₂ and oxidizing environment after 100 min of drying

The ash, char, and volatile content align with the elemental composition as detailed in section 2.4. Devolatilization initiates at 115 °C (T_{Devol}). Combustion initiates with a residual coefficient of 0.254. The devolatilization process reveals three distinct zones, suggesting a division between light and heavy volatiles. However, for simplicity, we have aggregated the volatiles into a single group in this study.

To obtain kinetic data for devolatilization and char combustion, the Arrhenius equation, which relates the rate constant of a chemical reaction to the temperature and activation energy, was utilized:

$$k_{kin} = Ae^{-\frac{E}{RT}} \quad (16)$$

With A being the pre-exponential factor, E the activation energy, R the universal gas constant, and T the absolute temperature. Non-linear least squares regression was employed to fit the Arrhenius equation to the experimental data. This fitting process yielded the pre-exponential factor (A) and the activation energy (E) for both devolatilization and carbon combustion. Finally, the quality of the fit was assessed by comparing the model predictions based on the optimized parameters with the experimental data.

In our study, we opted for this simplified approach to determine the kinetics of our red liquor system instead of more sophisticated methods, such as the Ozawa-Flynn-Wall model that requires TGA with at least three different heating rates. While these advanced techniques offer comprehensive insights into the kinetics of reactions, our primary goal was to obtain a preliminary indication of the kinetics

rather than delve deeply into kinetic analysis. This approach provided us with a foundational understanding of the kinetics, setting a solid groundwork for future in-depth studies if necessary.

Table 1 summarizes the results for E and A from the data fitting.

Table 1: Activation Energy E and pre-exponential factor A from data fitting

	E (J/kmol)	A (1/s)
Devolatilization	3.54×10^6	3.16
Char combustion	1.17×10^7	44.98

Figure 5 shows the model predictions for the devolatilization based on the values from Table 1 and the experimental data.

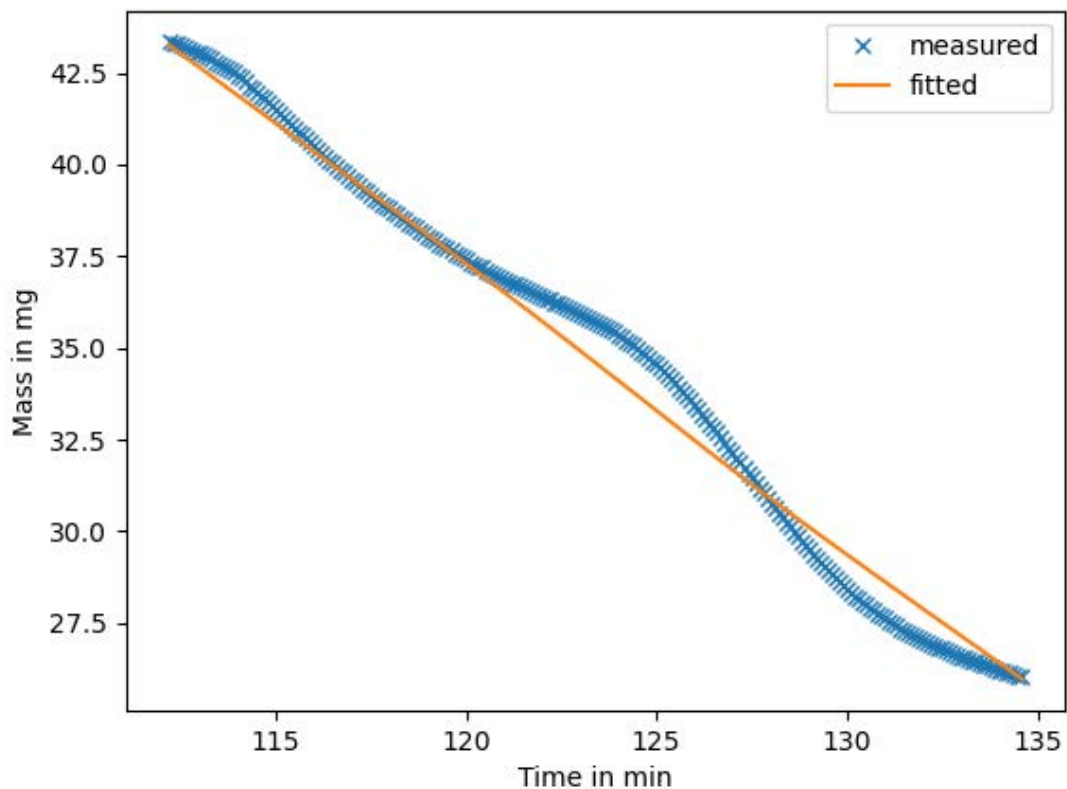


Figure 5: Model prediction for grouped volatiles and experimental mass loss over time during devolatilization ($t = 112 - 135$ min)

Figure 6 shows the model predictions for the char combustion based on the values from Table 1 and the experimental data.

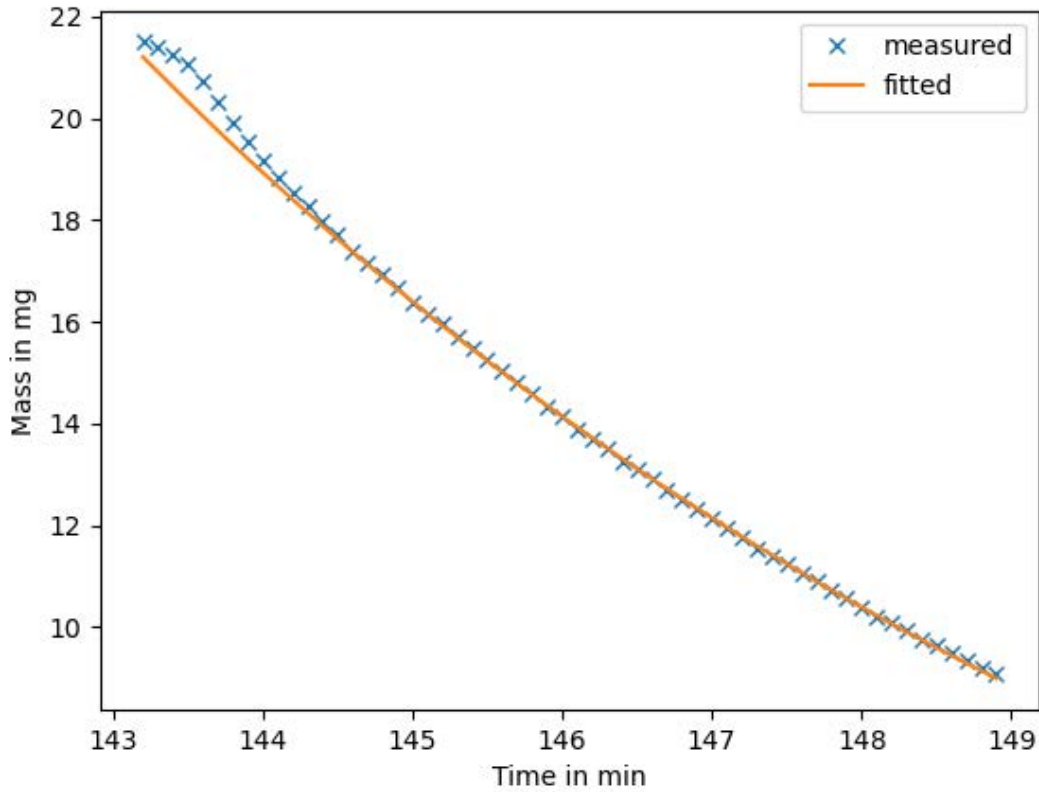


Figure 6: Model prediction and experimental mass loss over time during char combustion (t = 143.2 min - 149 min)

2.2.2 Phase Change and Reaction Models

The following describes the applied phase change and reaction models, including drying of fuel droplets, devolatilization, gas phase combustion, and solid char combustion.

Drying of fuel droplets

Drying of the particle is calculated using the Spalding evaporation model [24]:

$$\frac{dm_{H_2O}}{dt} = \pi d_p Sh \rho_g D_{H_2O} \ln \left(1 + \frac{Y_{H_2O,F} + Y_{H_2O,\infty}}{1 - Y_{H_2O,F}} \right) \quad (17)$$

With D_{H_2O} being the diffusion coefficient, Sh the Sherwood number, which describes the ratio of convective to diffusive mass transport. $Y_{H_2O,F}$ represents the mass fraction of evaporated water in the film surrounding the droplet and $Y_{H_2O,\infty}$ in the far field. A detailed description of the model can be found in [25]. If the saturation pressure is greater than 99.9 % of the critical pressure of water, drying is calculated as flash boiling based on the model by Zuo et al. [26].

Devolatilization

Devolatilization of volatiles is calculated using the single kinetic rate devolatilization:

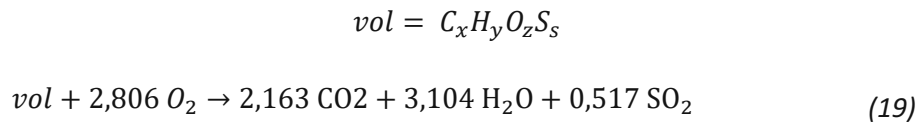
$$\frac{dm}{dt} = k_{kin} \cdot m \quad (18)$$

The kinetic rate k_{kin} is calculated following Arrhenius (Equation (16)). The activation energy E and the pre-exponential factor A are given in Table 1.

We use a pseudo-species $C_xH_yO_zS_s$ to represent the volatile components that combust, as described in equation (14). Because there are no thermophysical properties for such a pseudo species, we calculate the molecular weight according to the reaction equation and otherwise use CH_4 properties as an estimation. To close the overall energy balance of red liquor conversion (dry heating value of 13.4 MJ/kg), we use the latent heat of devolatilization and calculated it to be 8.9 MJ/kg. 20 % of the enthalpy is retained by the particle due to surface reactions.

Gas Phase Combustion

The combustion of volatiles in the gas phase reads



The gas phase combustion is modeled using the Eddy Dissipation Diffusion Model [27]. This Turbulence-Chemistry Interaction Model is commonly used to predict the combustion behavior in turbulent flows [28]. The model does not use kinetic data. The time scale is determined by the minimum turbulence and diffusion time scales. The turbulence mixing time scale is taken from the turbulence model ($k - \epsilon$). The diffusion time scale describes the volatile-oxygen mixing in laminar regions:

$$w_{vol} = \frac{\rho}{C} \min\left(Y_{vol}, \frac{Y_{O_2}}{2.806}\right) \max(t_{diff}, t_{turb}) \quad (20)$$

$$t_{diff} = AB \frac{v_{eff}}{(\Delta t)^2} \quad (21)$$

$$t_{turb} = C_{EDC} \frac{\epsilon}{k} \quad (22)$$

With Y_{vol} being the volatile mass fraction, Y_{O_2} the oxygen mass fraction and 2.806, the stoichiometric oxygen to volatile mass ratio.

Carbon Combustion

The char combustion



is calculated following the single kinetic rate model

$$\frac{dm_{char}}{dt} = k_{kin} m \quad (24)$$

The kinetic rate k_{kin} is calculated following Arrhenius (Equation (16)). The activation energy E and the pre-exponential factor A are given in Table 1.

2.3 Simulation Setup

The simulation setup was based on an industrial red liquor combustion vessel as a reference case. The following describes the simulation geometry, the computational mesh, and the applied boundary conditions.

2.3.1 Simulation Geometry

Figure 7 shows the 3D Geometry of the combustion vessel with its inlets and outlets.

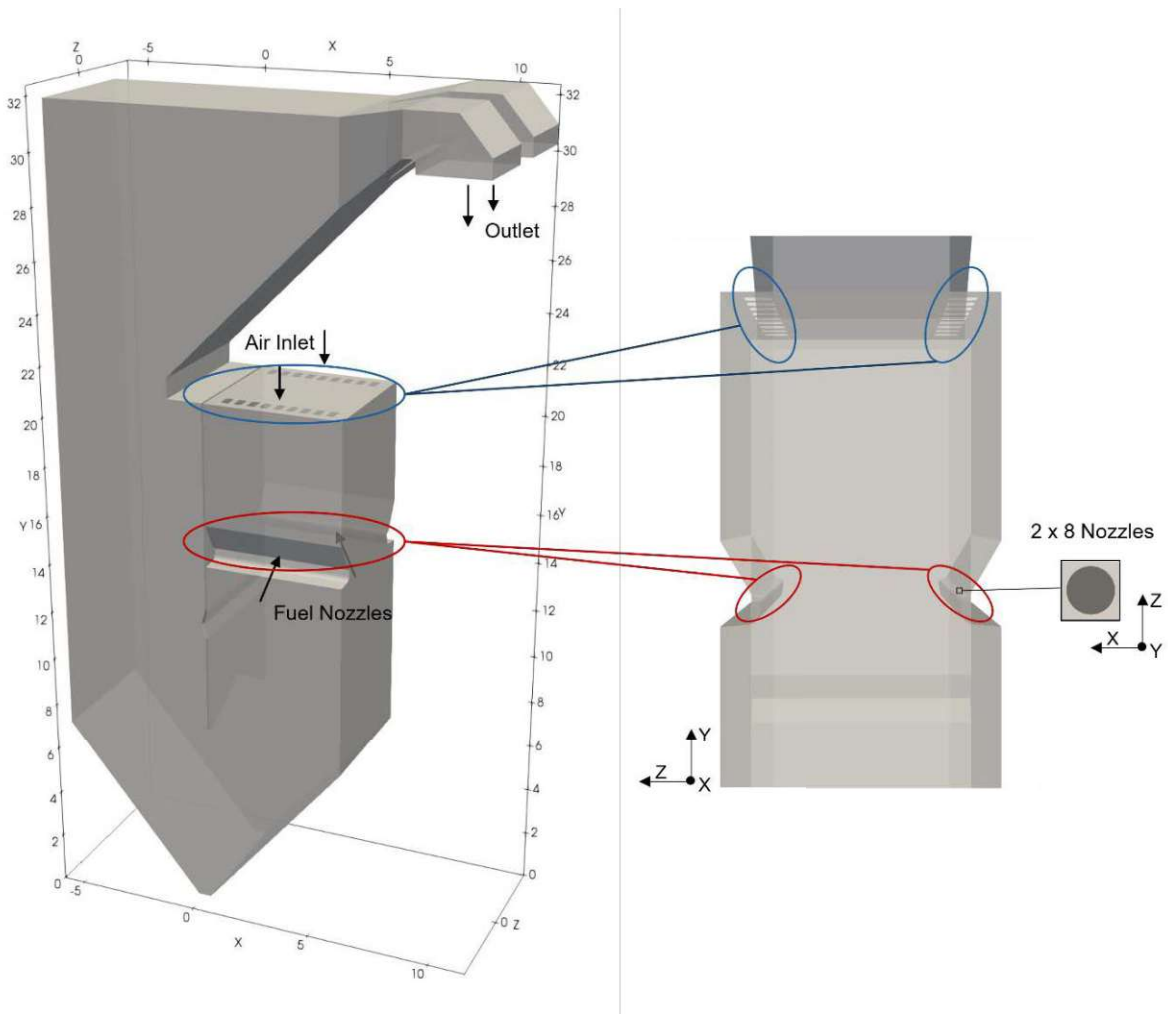


Figure 7: Combustion vessel with inlets and outlets (dimensional grid in m)

The combustion air enters through 18 square openings from the top, while the fuel enters through 16 nozzles modeled as round openings with a diameter of 27 mm. The combustion zone is lined with refractory material, simulated as adiabatic walls. The vessel is simulated until the outlet shown in Figure 1, which is situated before the gas clearing units. As the combustion gas travels towards the outlet, it heats steam through tube bundle heat exchangers, modeled as anisotropic porous zones with a heat sink (Figure 8).

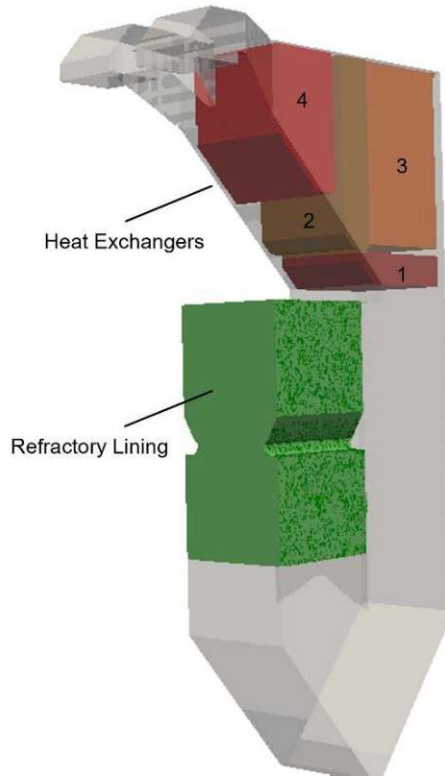


Figure 8: Heat exchanger 1 to 4 in red and brown and refractory lining zone in green

The porosity accounts for pressure loss, and the heat sink for the heat transfer. For each heat exchanger, the porosity $f_{x,y,z}$ is calculated in x, y, and z directions as following

$$f_{x,y,z} = \frac{A_{void}}{A_{total}} \quad (25)$$

With A_{void} being the void area and A_{total} the total area. The pressure loss Δp is calculated according to the Darcy-Forchheimer law

$$\Delta p = - \left(\mu D + \frac{\rho |U|}{2} F \right) U \quad (26)$$

With μ being the dynamic viscosity and ρ the density of the fluid, U the velocity of the fluid. D and F are the Darcy and the Forchheimer coefficients, respectively. Assuming the heat bundles are perforated plates, Idelchik's equation for perforated plates is applied [29]:

$$D = 0$$

And

$$F_{x,y,z} = \frac{(0.707(1 - f_{x,y,z})^{0.375} + 1 - f_{x,y,z})^2}{f_{x,y,z}^2} \quad (27)$$

Table 2 summarizes the applied Forchheimer coefficients F.

Table 2: Forchheimer coefficients F for heat exchangers 1 to 4 in 1/m

	1	2	3	4
F _x	0.1654	0.8742	0.1654	0.8742
F _y	0.1654	0.8742	0.1402	0.6295
F _z	3.3624	3.3449	1.3337	1.8810

The heat transfer over the heat exchangers is known from standard operation of the vessel. Table 3 summarizes the applied heat loss over the heat exchangers.

Table 3: Heat sink of heat exchanger 1 to 4 in MJ

1	2	3	4
2440	1850	1030	1540

2.3.2 Computational Mesh

To perform the CFD simulation, the domain of interest is discretized into a predominantly hexahedral mesh using snappyHexMesh in OpenFOAM®. The domain is divided into four zones with different refinement levels to ensure reasonable computational times while having a fine enough computational grid (Figure 9).

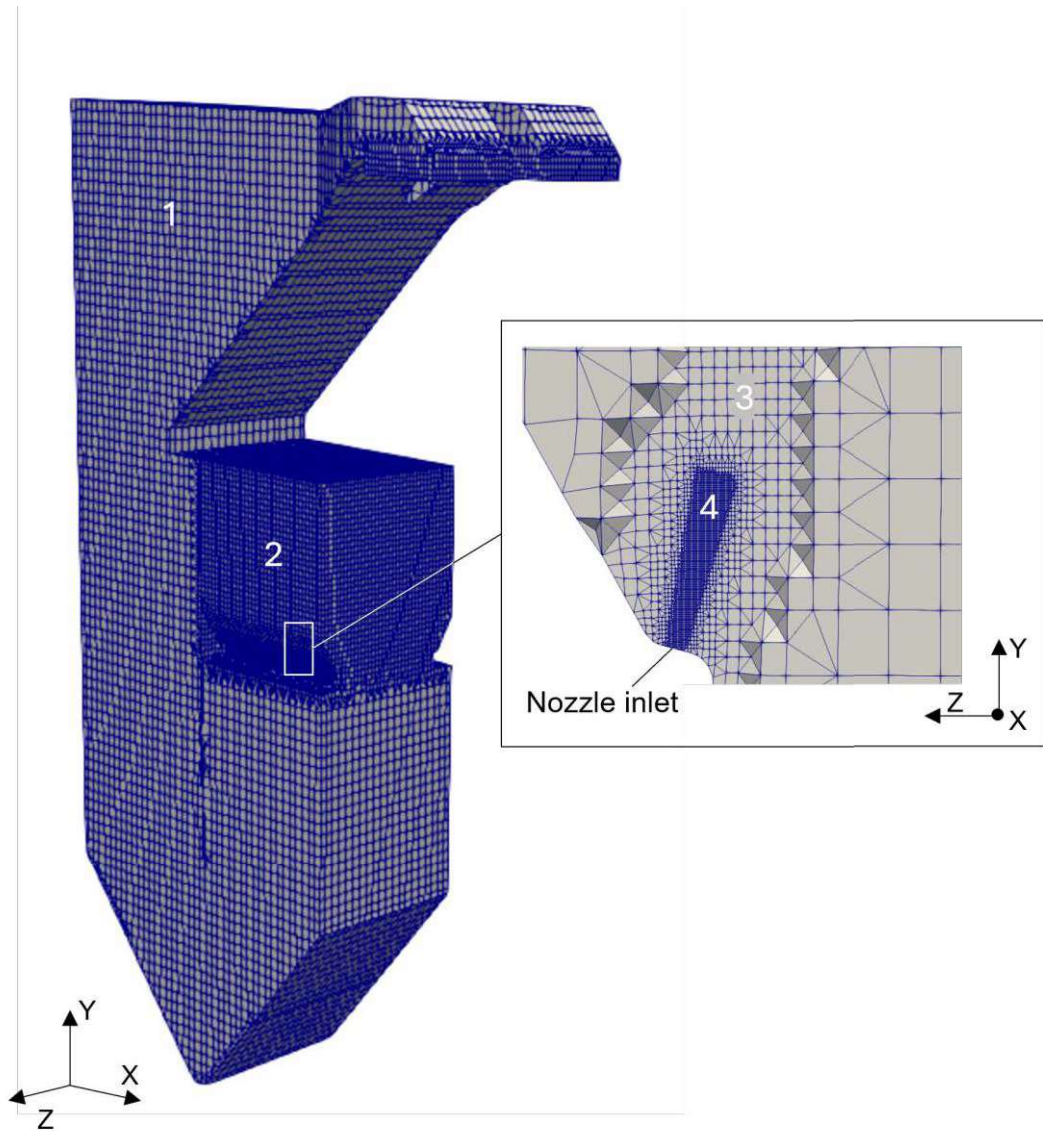


Figure 9: Calculation mesh with four different refinement levels (left: Overall combustion vessel, right: Nozzle inlet area)

The mesh has 867,000 cells and is divided into four regions with different refinement levels (see Figure 9). The mesh has a maximum aspect ratio of 7.7, maximum non-orthogonality of 59, and maximum skewness of 2.3.

The mesh size of the mesh region 4, which is close to the nozzle inlet, is set to meet two conditions: One, the cell size is greater than the size of the fuel droplets (characteristic droplet sizes are 2 to 3 mm), a requirement to track the Lagrangian particles correctly (see chapter 2.1). Second, the cell size is small enough to correctly predict the velocity field of the spraying. To determine which cell size meets the second condition, the velocity field of the spraying was calculated with different cell sizes and com-

pared to literature values. Figure 10 shows the relative velocity along the centerline (Centerline velocity U_c /Maximum velocity at nozzle exit U_m) of the spraying calculated with different cell sizes compared to data from Mi et al. [30].

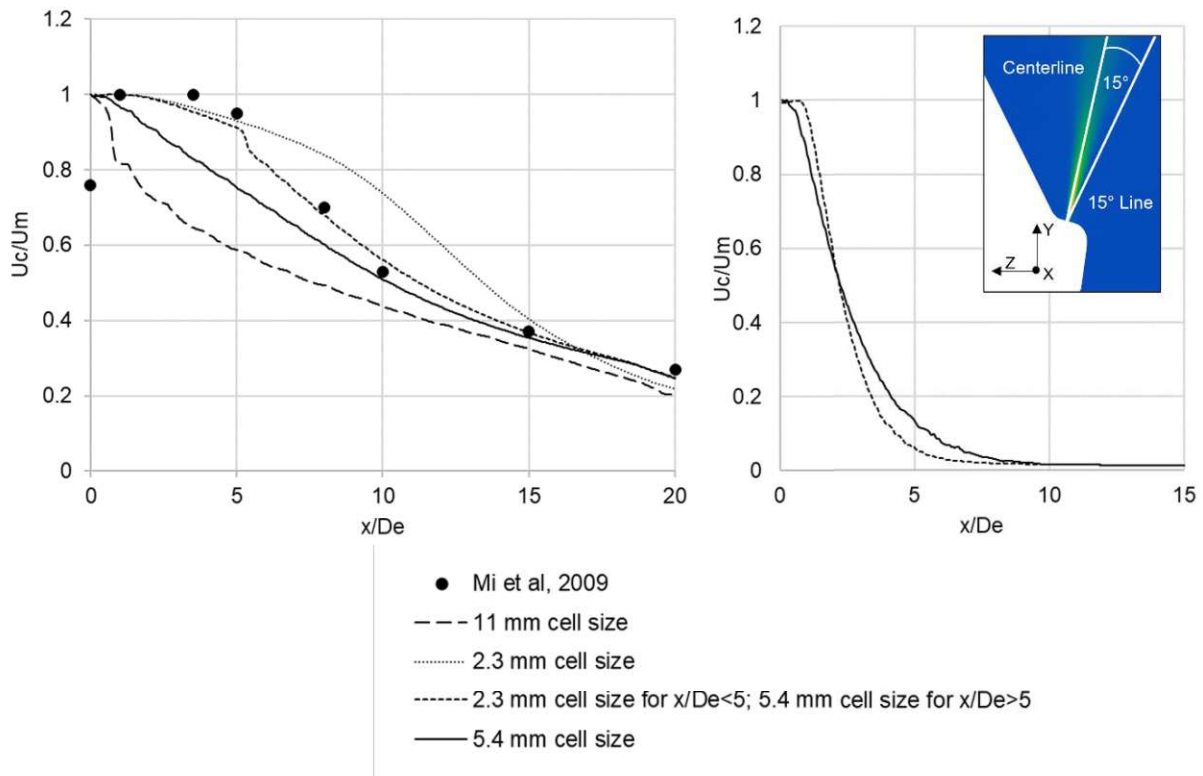


Figure 10: Left: Relative velocity along the center line, Right: Relative velocity along 15° line; (x: Distance from the nozzle; De: Nozzle diameter)

Close to the nozzle, the velocity is predicted the best by applying a cell size of 2.3 mm. Close to the nozzle, the velocity is underestimated when applying a cell size of 5.4 mm. However, 20 cm from the nozzle ($x/De=7$), the velocity is predicted the best when applying a cell size of 5.4 mm. The combination of two cell sizes, 2.3 mm close to the nozzle and 5.4 mm further from the nozzle, predicts the velocity best. However, looking at the 15° line of the nozzle spraying instead of the centerline, both mesh, the optimized mesh, combining the two cell sizes 2.3 and 5.4 mm, and the 5.4 mm mesh, are predicting a similar velocity. To ensure meeting the condition, that the cell size is greater than the size of the fuel droplets and following the observations made through the mesh study, a cell size of 5.4 mm was chosen for the simulation.

Table 4 summarizes the cell average volumes of the different refinement levels of the final mesh.

Table 4: Cell volume of different refinement regions shown in Figure 9

Refinement Region	1	2	3	4

<i>Cell Volume (m³)</i>	4.601*10 ⁻⁴	1.150*10 ⁻⁴	7.189*10 ⁻⁶	1.123*10 ⁻⁷
------------------------------------	------------------------	------------------------	------------------------	------------------------

2.3.3 Boundary Conditions and Evaluation

The applied boundary conditions are based on normal operation conditions of the industrial reference combustion vessel. The red liquor has a water content of 38 wt%. The elemental composition on dry basis is given in Table 5.

Table 5: Elemental composition of red liquor in wt% dry mass

Ash	11.20
Char	21.80
Volatiles	67.00
C	38.80
H	3.79
S	10.69
O	33.90

A volumetric flow rate of 154 034 Nm³/h at 383 °C is specified for the air inlet. The air composition comprises 76.52 wt% N₂, 23.4 wt% O₂, 0.08 wt% CO₂. The red liquor spraying is a two-phase spraying with red liquor and water vapor. Red liquor is injected at a rate of 14.64 l/s with a density of 1302 kg/m³, with a temperature of 106 °C. Simultaneously, water vapor is introduced at a rate of 2.82 kg/s, with a temperature of 162 °C.

To assess the reliability of the simulation we compared our simulations to measurement data available from the industrial reference plant as well as to expectations derived from literature. The assessment includes answering following questions: Are the visualized results physically accurate and reasonable? Is the temperature inside the combustion vessel in agreement with measurement data? Is the gas composition at the outlet in agreement with measurement data? Is the combustion time in agreement with expectations based on literature values?

2.4 Virtual experiments

The red liquor injection was simulated varying three spraying parameters: spray type, spraying angle, and particle size. The particle-size distribution was modeled by drawing random samples from the Rosin-Rammler (Weibull) probability density function (PDF) as described in [31]. The shape parameter n was set to 3. The scale parameter λ , which represents the characteristic particle diameter was varied. Figure 11 summarizes the varied parameters.

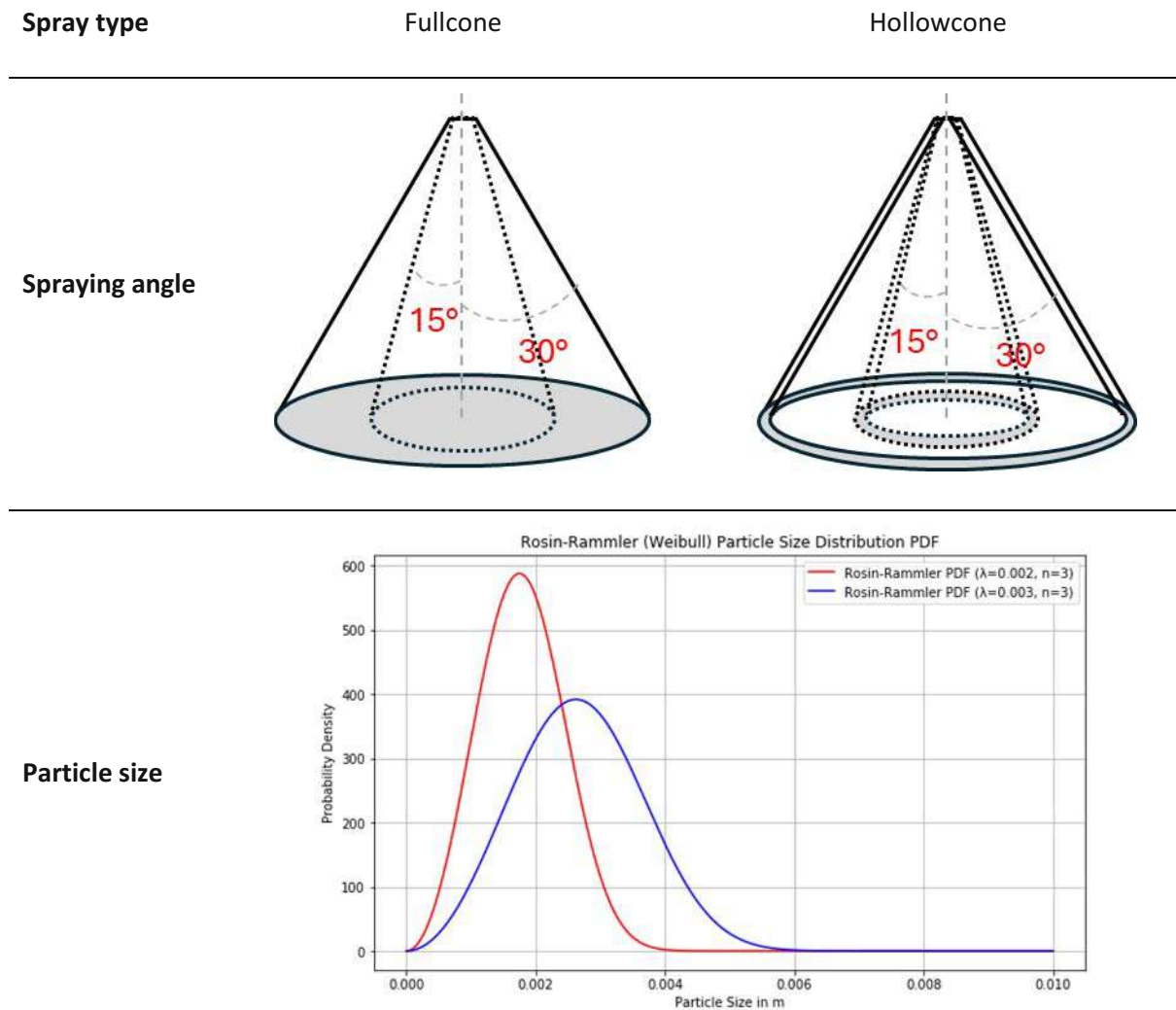


Figure 11: Varied parameters of virtual experiments

Table 8 summarizes the virtual experiments conducted in this study.

Table 6: Parameter setting in virtual experiments

	Particle size λ (mm)	Spraying angle in ($^{\circ}$)	Spray type
Experiment#1	2	30	Hollowcone

Experiment#2	2	15	Hollowcone
Experiment#3	3	30	Hollowcone
Experiment#4	3	15	Hollowcone
Experiment#5	2	30	Fullcone
Experiment#6	2	15	Fullcone
Experiment#7	3	30	Fullcone
Experiment#8	3	15	Fullcone

3 Results and Discussion

The following presents the results of the simulations that were conducted. Firstly, the simulation case with a characteristic droplet diameter λ of 2 mm, a spraying angle of 30° , and the spray type hollow-cone is examined in detail as reference case to assess the accuracy of the simulations. Finally, the outcomes of the virtual experiments are presented.

3.1 Evaluation of Simulation Results

Figure 12 visualizes the Lagrangian particles colored based on their time inside the combustion vessel since injection and their ash content, representing simulation results.

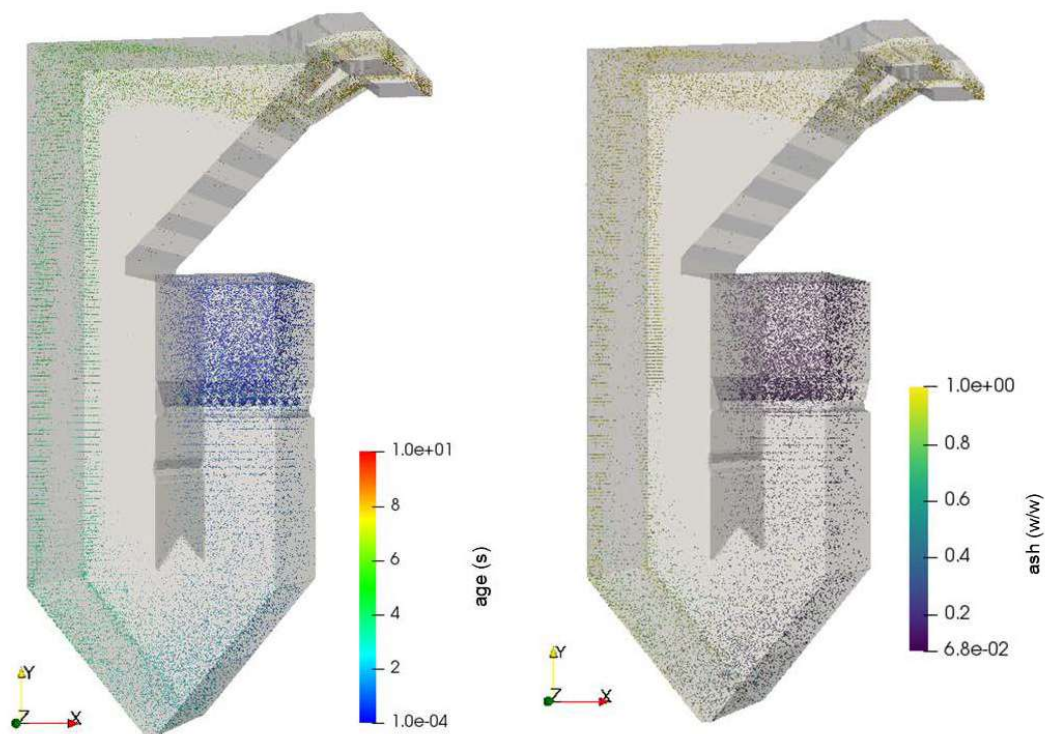


Figure 12: Left: Lagrangian particles visualized scaled by factor 10 colored based on the age in s; right: Simulation results: Lagrangian particles visualized scaled by factor 10 colored based on the ash weight fraction

The particles have a residence time of 8 to 10 seconds in the vessel and enter after around 4 to 5 s the cooling section of the heat exchangers. The increasing ash content of the visualized Lagrangian particles shows the progress of combustion as the particles travel through the combustion vessel. The results show that almost all particles have an ash content of 1 when reaching the vessel exit, only few particles are not completely combusted. We can derive further insides into the reaction system inside the vessel by looking at the Eulerian field. Figure 13 shows the streamlines inside the vessel.

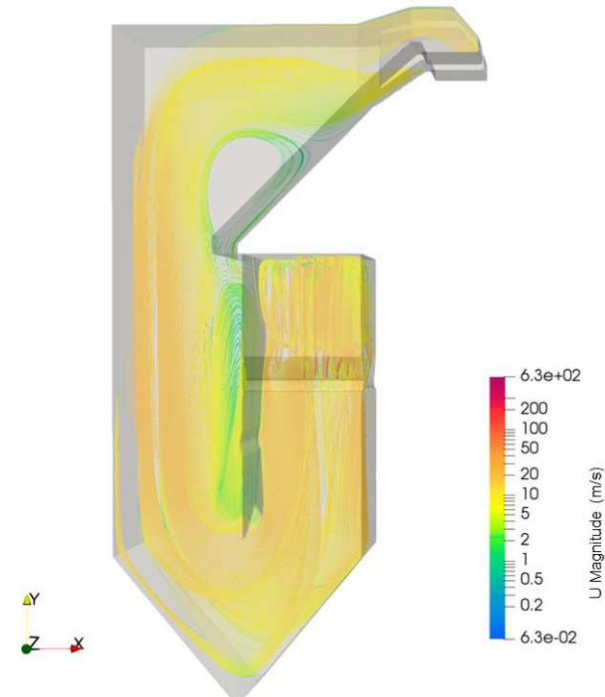


Figure 13: Calculated streamlines in Eulerian field colored based on the velocity in m/s

The streamlines depict the gas flow through the furnace. Figure 14 shows the temperature along with the CO₂ content of the Eulerian field.

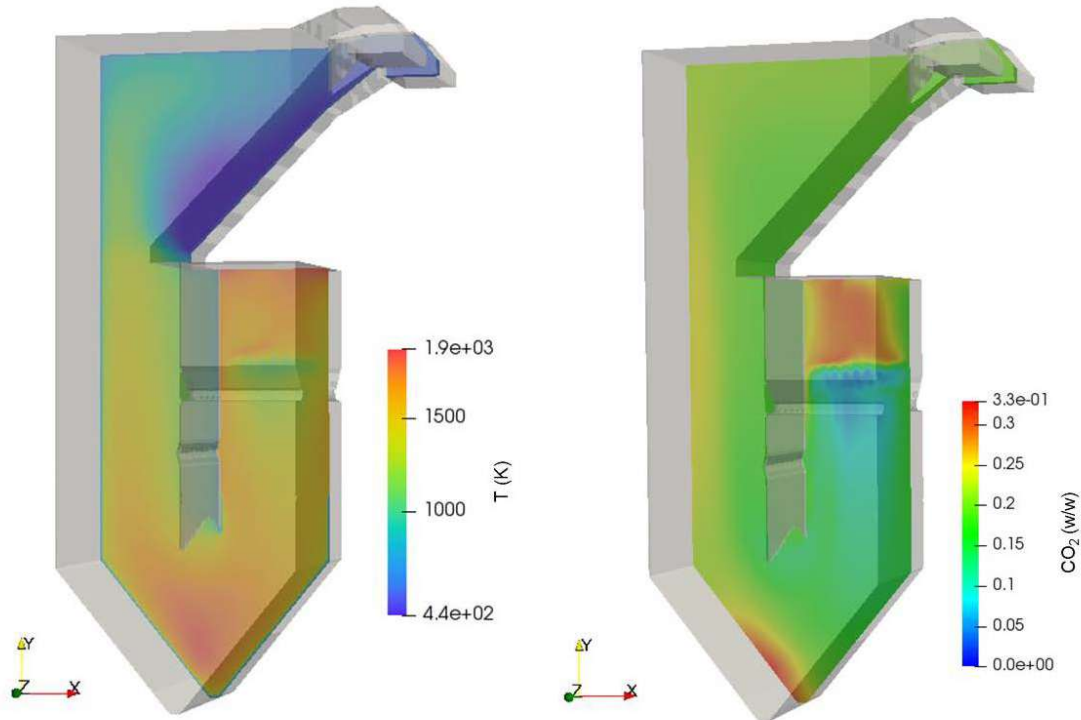


Figure 14: Left: Simulation results for temperature in K in Eulerian field; right: Simulation results for CO₂ weight fraction in Eulerian field

At the area of red liquor injection, the temperature drops due to water evaporation and the endothermic devolatilization. The temperature reaches a maximum of 1900 K inside the vessel due to exothermic combustion reactions and decreases over the heat exchangers due to their cooling effect. The increase in temperature in the area above fuel injection and at the vessel bottom can be traced to exothermic combustion reactions, which is confirmed by the increased CO₂ in those areas. The combustion above fuel injection can be attributed to volatile combustion, while the combustion in the bottom area is due to char combustion. The volatile release and the volatile combustion can be seen in Figure 15.

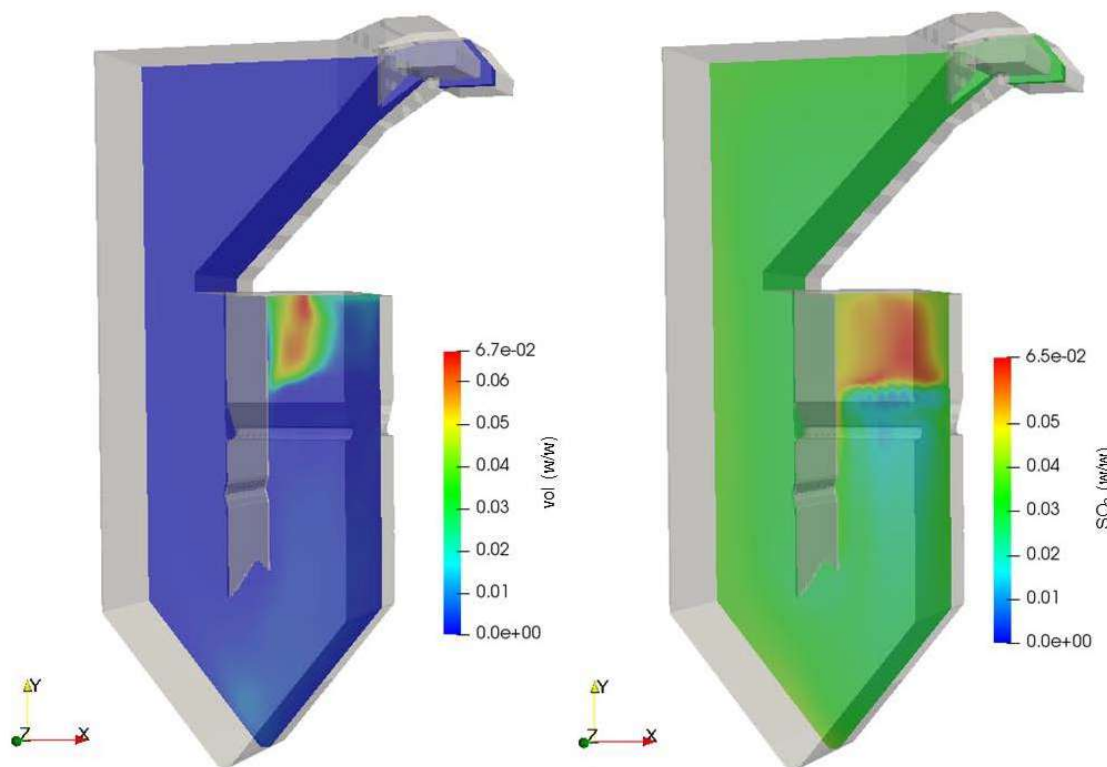


Figure 15: Left: Simulation results for volatile weight fraction in Eulerian field; right: Simulation results for SO₂ weight fraction in Eulerian field

The biggest volatile release is happening in the area above fuel injection, where the volatiles are also combusting as the SO₂ increase in this area indicates.

Industrial data provide three temperature measurements on a plane inside the combustion vessel. The temperature profile at this plane was extracted from CFD simulations to evaluate the simulations (Figure 16).

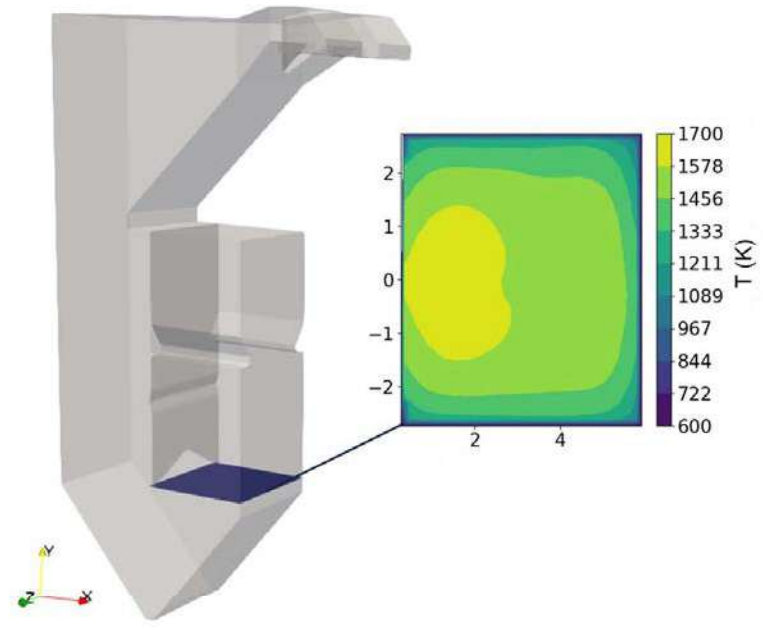


Figure 16: Combustion vessel with simulated temperature profile in K on plane highlighted in blue. The temperature measurements at the plane are located approximately 0.5 m from the wall. The measured temperatures are in the range of 1465 K to 1485 K. The simulated temperatures closely match these measured values.

Further industrial data used to evaluate the performed simulations include the gas outlet composition. Table 7 summarizes the calculated and measured gas outlet composition. The deviation between calculation and measurement is given as

$$Deviation (\%) = \frac{x_{calculated} - x_{measured}}{x_{measured}} \cdot 100 \quad (28)$$

Table 7: Gas composition in vol% dry

	<i>Measurement with standard deviation s</i>	<i>Calculation</i>	<i>Deviation (%)</i>
CO ₂	17.4 (s:0.21)	17.89	3
O ₂	2.29 (s:0.18)	4.65	103
SO ₂	1.13 (s:0.02)	1.92	71

The calculated SO_2 content is 71 % higher compared to the measurement. The simulation assumes that all the sulfur present in the fuel reacts to form SO_2 . However, in reality, sulfur is partially recovered in the ash as MgSO_4 , which explains the lower SO_2 content in the measurement. The CO_2 content has a deviation of 3 % and is, therefore, in good agreement with the measurement. The calculated O_2 content is 103 % higher than the measured one. Looking at the calculated gas composition over the outlet area, it is notable that the gas composition shows local differences across the outlet area (Figure 17).

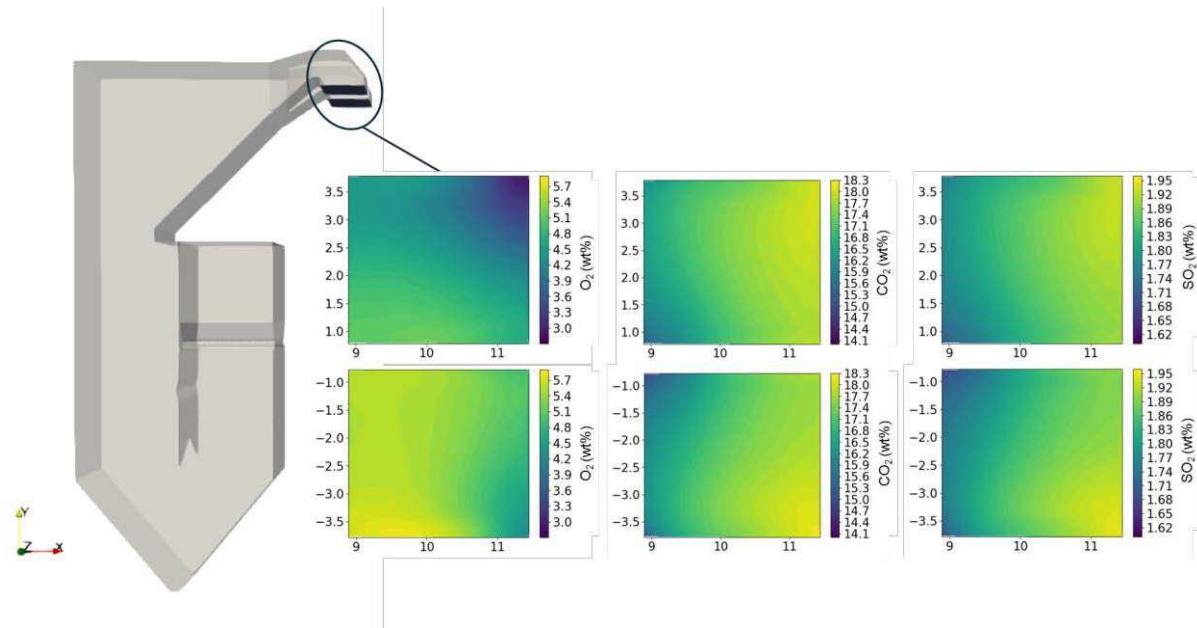


Figure 17: dry wt% of CO_2 , O_2 and SO_2 at the two outlet planes

The O_2 content ranges between 2.8 and 5.8 wt%. Such variation across the outlet area indicates that the measurement depends highly on the position of the sensor. The deviation between measured and calculated O_2 content can therefore be partially attributed to the sensor position and partially to the simplified reaction system in the model.

Figure 18 shows the simulated mean particle mass loss over time as relative mass m/m_0 .

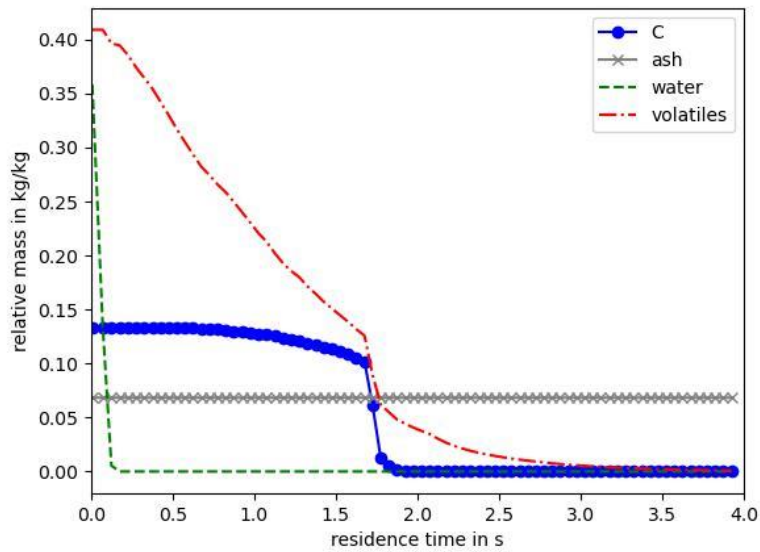


Figure 18: Mean relative particle mass m/m_0 in kg/kg over residence time for the experiment 2mm, 30°, Hollowcone

The water content is depleted in less than 0.2 s. Char combustion begins when the residual coefficient of the volatiles is reached, peaks at around 1.7 s and completes after around 1.9 s. Bajpai et al. provide the following timeframe for black liquor droplet combustion [2]:

- Drying 0.1 - 0.2 seconds
- Devolatilization: 0.2 - 0.3 seconds
- Char combustion: 0.5 – 1 seconds

Järvinen determined the combustion time of 2 mm black liquor droplets in 1000 °C dry air experimentally [32]. The drying and devolatilization was completed after around 2.8 s, the char combustion after around 6 s. While these time frames are not specific to red liquor combustion, they indicate what to expect and show that our simulation results are in the expected range given in literature.

The overall results show a satisfactory alignment with both industrial plant data and literature. Considering that the objective of this study is a qualitative assessment evaluating the influence of spraying characteristics on combustion time rather than quantitative analyses, the simulations are evaluated as reliable for a comparative parameter study.

3.2 Effect of spray characteristics on combustion time

Figure 19 shows the mean combustion time for a particle for the different virtual experiments, and Table 8 gives the exact times in numbers. The combustion time is defined as the time when the char content in the particle reaches the threshold of 0.01.

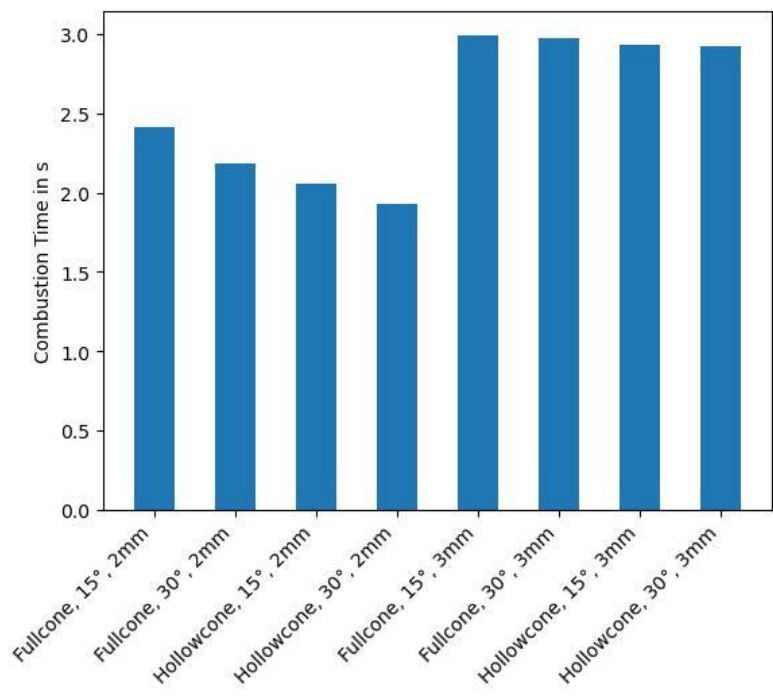


Figure 19: Mean combustion time for a particle for the different virtual experiments

Table 8: Results of design of virtual experiment

<i>Factor</i>	<i>Particle size λ (mm)</i>	<i>Spraying angle (°)</i>	<i>Spray type</i>	<i>Combustion time (s)</i>
Experiment#1	2	15	Hollowcone	2.05
Experiment#2	2	30	Hollowcone	1.93
Experiment#3	3	15	Hollowcone	2.93
Experiment#4	3	30	Hollowcone	2.92
Experiment#5	2	15	Fullcone	2.41
Experiment#6	2	30	Fullcone	2.18
Experiment#7	3	15	Fullcone	2.99
Experiment#8	3	30	Fullcone	2.97

The fastest combustion is achieved when combusting particles with a characteristic particle size of 2 mm with hollowcone spraying and a spraying angle of 30°. Combusting particles with a characteristic particle size of 3 mm with fullcone spraying and a spray angle of 15° shows the longest combustion time. The following discusses the influence of the three investigated spraying characteristics (droplet size, spraying angle, and spray type) on the particle combustion time in detail.

Influence of droplet size

As expected, a smaller mean droplet diameter accelerates combustion due to reduced mass needing evaporation and devolatilization. Figure 20 illustrates this effect by comparing the mean particle mass loss over time across different experiments, with particle size being the sole distinguishing factor in each pair.

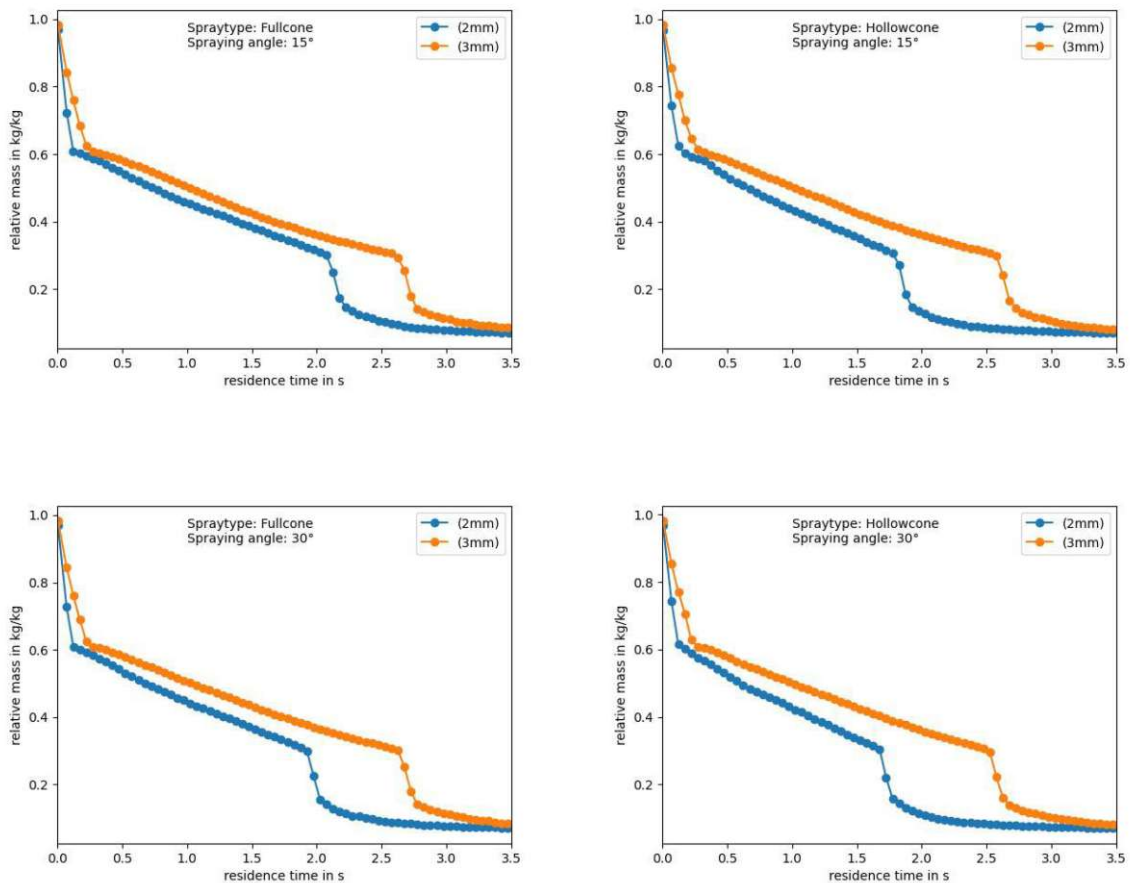


Figure 20: Mean particle mass as relative mass m/m_0 over time for mean droplet size 2mm vs 3mm

The initial drop in mass is attributed to drying, followed by a less steep mass loss due to devolatilization. The rapid decrease in mass loss indicates the main char combustion phase. Table 9 gives the calculated effect of particle diameter reduction on combustion time (CT) in %:

$$\text{Effect of diameter reduction} = \frac{CT_{2mm} - CT_{3mm}}{CT_{3mm}} \quad (29)$$

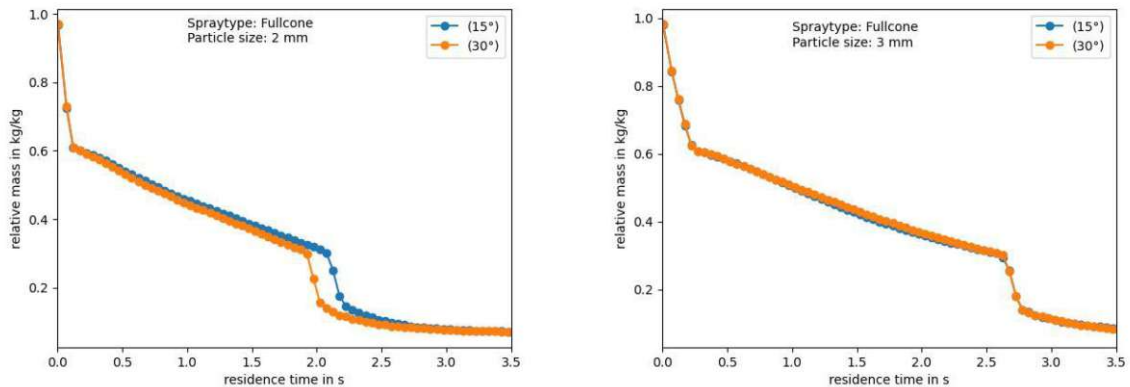
Table 9: Calculated influence of mean droplet size on particle combustion time

<i>Spraying angle (°)</i>	<i>Spray type</i>	<i>Effect of particle reduction (%)</i>
15	Hollowcone	-30
30	Hollowcone	-34
15	Fullcone	-19
30	Fullcone	-27

The reduction in combustion time across all sets of experiments is $\geq 19\%$, highlighting the significant impact of particle size on combustion duration. When spraying as hollowcone with a spraying angle of 30° the combustion time is 34 % faster when reducing the characteristic particle size from 3 mm to 2 mm.

Influence of spraying angle

Figure 21 shows the mean particle mass loss over time across different experiments, with the spraying angle being the sole distinguishing factor in each pair.



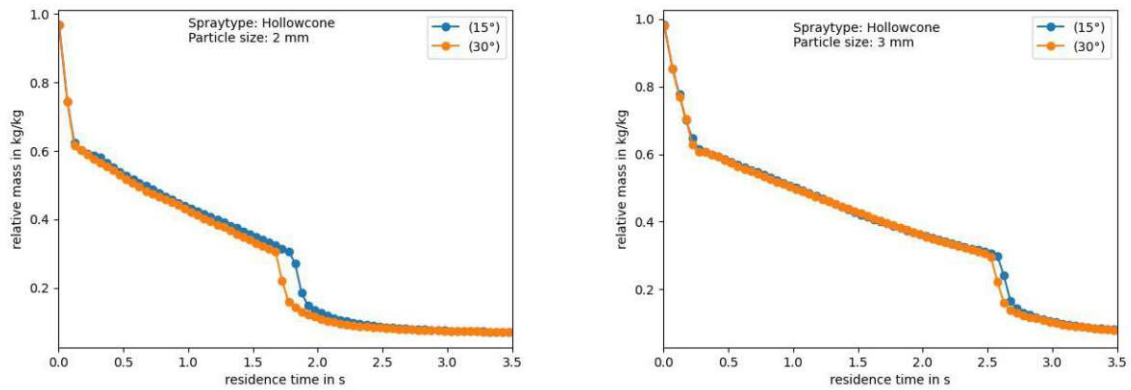


Figure 21: Mean particle mass as relative mass m/m_0 over time for spraying angle 15° vs 30°

Almost all experiments show, that widening the spraying angle accelerates combustion. When combusting particles with a characteristic size of 3 mm with fullcone spraying, no change in combustion time can be observed. Table 10 gives the calculated effect of widening the spraying angle on combustion time (CT) in %:

$$\text{Effect of spraying angle} = \frac{CT_{30^\circ} - CT_{15^\circ}}{CT_{30^\circ}} \quad (30)$$

Table 10: Calculated influence of spraying angle on particle combustion time

Particle size λ (mm)	Spray type	Effect of widened spraying angle (%)
2	Hollowcone	-6
3	Hollowcone	0
2	Fullcone	-10
3	Fullcone	-1

When combusting 2 mm particle, the combustion time is reduced by up to 10 % by using a 30° spray angle instead of a 15° spray angle. When combusting particles with a characteristic size of 3 mm, the effect is insignificant.

Influence of spray type

Figure 22 shows the mean particle mass loss over time across different experiments, with the spray type being the sole distinguishing factor in each pair.

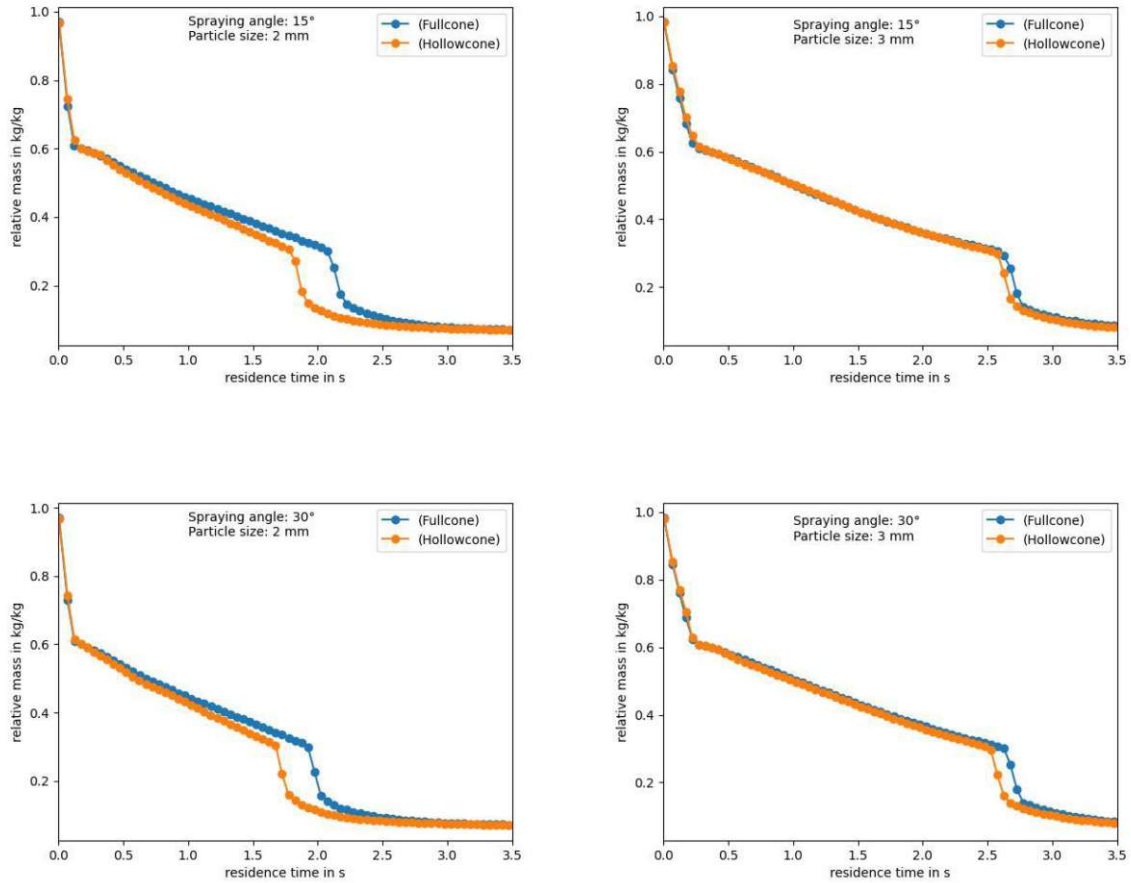


Figure 22: Mean particle mass as relative mass m/m_0 over time for spray type fullcone vs hollowcone

For all cases, hollowcone spraying is beneficial for a fast combustion compared to fullcone spraying. Table 11 gives the calculated effect of changing the spray type on combustion time (CT) in %:

$$Effect\ of\ spray\ type = \frac{CT_{Hollowcone} - CT_{Fullcone}}{CT_{Fullcone}} \quad (31)$$

Table 11: Calculated influence of spray type on particle combustion time

Particle size λ (mm)	Spraying angle ($^\circ$)	Effect of changing spray type (%)
2	15	-15
3	15	-2

2	30	-12
3	30	-2

For all experiments changing the spray type from fullcone to hollowcone has a reducing effect on combustion time. The reduction in combustion time is with 12 and 15 % high when combusting 2 mm particles, while the effect is with 2 % significantly smaller when combusting 3 mm particles.

4 Conclusion and Outlook

A CFD model for the combustion of red liquor was developed, and CFD simulations were performed analyzing the effect of different spraying characteristics on the droplet combustion time inside an industrial-sized combustion vessel. The results demonstrate that our simulations align reasonably well with industrial plant data and literature sources. They also yield physically expected outcomes, affirming the reliability of our CFD setup for qualitative studies investigating the influence of various parameters on combustion time. Through virtual experiments varying spraying characteristics such as characteristic particle size, spraying angle, and spray type, we discovered that the fastest combustion was achieved with a characteristic droplet size of 2 mm, a spraying angle of 30°, and using the hollowcone spray type. These spraying characteristics promote optimal fuel dispersion within the combustion vessel, leading to accelerated combustion rates. Notably, reducing particle diameter exhibited the most significant effect, reducing combustion time by approximately 30 %. Widening the spraying angle from 15° to 30° could further enhance combustion by up to 10 % when combusting droplets with a characteristic size of 2 mm, although this effect was marginal when combusting droplets with a characteristic size of 3 mm. Similarly, switching from fullcone to hollowcone spraying reduced combustion time by up to 15 % when combusting droplets with a characteristic size of 2 mm and 2 % when combusting droplets with a characteristic size of 3 mm. Overall, the influence of spraying characteristics on combustion time was higher for fuel droplets with a characteristic size of 2 mm compared to fuel droplets with a characteristic size of 3 mm.

With our study, we aimed to perform a comparative study of the influence of different spraying characteristics on the combustion time. For that purpose, we implemented one-step combustion models and derived devolatilization and char combustion kinetics from non-isothermal TG analyses. To improve the level of detail of the performed simulations, we recommend expanding the implemented reaction models into a sophisticated reaction system, including the H₂O and CO₂ gasification of char and the resolved description of the devolatilization of single components. It must be noted that such an extension requires detailed experimental kinetic determination. Furthermore, the model can be improved by incorporating particle swelling, a typical behavior of spent pulping liquor during combustion, and non-sphericity of the particles.

5 Acknowledgments

The authors especially thank Karin Wieland from the Competence Center CHASE GmbH for her cooperation on the project. This work was financially supported by the Competence Center CHASE GmbH. CHASE Competence Center is subsidized in the frame of COMET – Competence Centers for Excellent Technologies by BMVIT, BMWFW, Wirtschaftsagentur Wien, State of Upper Austria, and its scientific partners. The COMET program is handled by FFG. The support by the project partner Sappi Papier Holding GmbH is greatly acknowledged. The authors acknowledge TU Wien Bibliothek for financial support through its Open Access Funding Programme.

6 Abbreviations and Symbols

Abbreviations

CFD	Computational Fluid Dynamics
CT	Combustion Time
PDF	Probability Density Function
TGA	Thermogravimetric Analysis

Roman symbols

<i>A</i>	1/s	Pre exponential factor
<i>A_{void}</i>	m ²	Void area
<i>A_{total}</i>	m ²	Total area
<i>C_D</i>	-	Drag coefficient
<i>D</i>	1/ m ²	Darcy coefficient
<i>E</i>	J/kmol	Activation Energy
<i>F</i>	1/m	Forchheimer coefficient
<i>F_D</i>	kg m/s ²	Drag force
<i>F_g</i>	kg m/s ²	Gravitational force
<i>F_L</i>	kg m/s ²	Lift force
<i>K</i>	m ² /s ²	Kinetic energy
<i>N</i>	-	Random normal with mean 0 and standard deviation 1
<i>Nu</i>	-	Nusselt number
<i>Pr</i>	-	Prandtl number
<i>R</i>	J/(K kmol)	Universal gas constant

<i>Re</i>	-	Reynolds number
<i>S_h</i>	J/(m ³ s)	Energy source term
<i>S_m</i>	kg/(m ³ s)	Mass source term
<i>S_u</i>	N/(m ³ s)	Momentum source term
<i>Sh</i>	-	Sherwood number
<i>Sc</i>	-	Schmidt number
<i>T</i>	K	Temperature
<i>T_{Devol}</i>	K	Temperature at which devolatilization starts
<i>U</i>	m/s	Velocity
<i>Y</i>	kg/kg	Mass fraction
<i>a</i>	-	Random between 0 and 1
<i>d</i>	m	Diameter
<i>d_v</i>	-	Vector [<i>a</i> cos(θ), <i>a</i> sin(θ), <i>u</i>].
<i>f_{x,y,z}</i>	-	Porosity
<i>g</i>	m/s ²	Gravitational acceleration
<i>h</i>	J/kg	Enthalpy
<i>k</i>	m ² /s ²	Turbulent kinetic energy
<i>k_{kin}</i>	1/s	Kinetic rate
<i>m</i>	kg	Mass
<i>n</i>	-	Shape parameter in Rosin-Rammler (Weibull) PDF
<i>p_i</i>	kg/(m s ²)	Partial pressure of component <i>i</i>

Δp	kg/(m s ²)	Pressure loss
t	s	time
u	-	Random between -1 and 1
\vec{u}	m/s	Velocity vector

Greek symbols

α_{eff}	m ² /s	Effective thermal diffusivity
ε	m ² /s ³	Turbulent dissipation rate
θ	-	Random between 0 and 2
λ	m	Characteristic particle size
μ	kg/(m s)	Dynamic viscosity
μ_{eff}	kg/(m s)	Effective viscosity
ρ	kg/m ³	Density
τ	kg/(m s ²)	Stress tensor
τ_{tur}	s	Turbulent timestep
ω	1/s	Vorticity

Subscripts

∞	Far field
c	Centerline
F	Film around particle
g	Gas
i	Species i
m	Maximum

7 References

1. Pratima Bajpai. Chapter 1 - Introduction. In *Pulp and Paper Industry: Chemical Recovery*; Pratima Bajpai, Ed.; Elsevier, 2017; pp 1–23, ISBN 978-0-12-811103-1.
2. Pratima Bajpai. Chapter 4 - Combustion of Black Liquor. In *Pulp and Paper Industry: Energy Conservation*; Pratima Bajpai, Ed.; Elsevier: Amsterdam, 2016; pp 67–100, ISBN 978-0-12-803411-8.
3. Lee, J.; Woo, S.; Lee, I.; Han, Y.; Yoon, Y. Characteristics of spray and combustion in gas-centered swirl coaxial injector with varying gas nozzle diameter. *Acta Astronautica* **2024**, *215*, 631–641, doi:10.1016/j.actaastro.2023.12.044.
4. Gopinath, S.; Devan, P.K.; Sabarish, V.; Sabharish Babu, B.V.; Sakthivel, S.; Vignesh, P. Effect of spray characteristics influences combustion in DI diesel engine – A review. *Materials Today: Proceedings* **2020**, *33*, 52–65, doi:10.1016/j.matpr.2020.03.130.
5. Zhao, Y.; Fan, W.; Zhang, R. Experimental study on the effect of injection schemes on fuel spray and combustion characteristics in a compact combustor. *Aerospace Science and Technology* **2023**, *141*, 108510, doi:10.1016/j.ast.2023.108510.
6. Bashmakov, I.A.; L.J. Nilsson; A. Acquaye; C. Bataille; J.M. Cullen; S. de la Rue du Can; M. Fishedick; Y. Geng; K. Tanaka. Industry. In *Climate change 2022: Mitigation of climate change : Working Group III Contribution to the Sixth Assessment Report of the Intergovernmental Panel on Climate Change*; P.R. Shukla, J. Skea, R. Slade, A. Al Khourdajie, R. van Diemen, D. McCollum, M. Pathak, S. Some, P. Vyas, R. Fradera, M. Belkacemi, A. Hasija, G. Lisboa, S. Luz, J. Malley, Eds.; Cambridge University Press: Cambridge, UK and New York, NY, USA, 2022; pp 1161–1244, ISBN 9781009157926.
7. Furszyfer Del Rio; Dylan D.; Sovacool, B.K.; Griffiths, S.; Bazilian, M.; Kim, J.; Foley, A.M.; Rooney, D. Decarbonizing the pulp and paper industry: A critical and systematic review of sociotechnical developments and policy options. *Renewable and Sustainable Energy Reviews* **2022**, *167*, 112706, doi:10.1016/j.rser.2022.112706.
8. Horton, R.; Grace, T. The effects of black liquor spray parameters on combustion behavior in recovery furnace simulations.
9. Laitinen, A.; Laurila, E.; Keskinen, K.; Vuorinen, V. Large-Eddy Simulation of two secondary air supply strategies in kraft recovery boilers. *Applied Thermal Engineering* **2022**, *216*, 119035, doi:10.1016/j.applthermaleng.2022.119035.
10. Shinjo, J. Recent Advances in Computational Modeling of Primary Atomization of Liquid Fuel Sprays. *Energies* **2018**, *11*, 2971, doi:10.3390/en1112971.
11. Hirche, D.; Birkholz, F.; Hinrichsen, O. A hybrid Eulerian-Eulerian-Lagrangian model for gas-solid simulations. *Chemical Engineering Journal* **2019**, *377*, 119743, doi:10.1016/j.cej.2018.08.129.
12. Tahry, S.H.E. k-epsilon equation for compressible reciprocating engine flows. *Journal of Energy* **1983**, *7*, 345–353, doi:10.2514/3.48086.
13. Launder, B.E.; Spalding, D.B. The numerical computation of turbulent flows. *Computer Methods in Applied Mechanics and Engineering* **1974**, *3*, 269–289, doi:10.1016/0045-7825(74)90029-2.
14. Wartha, E.-M.; Haugen, N.E.; Karchniwy, E.; Bösenhofer, M.; Harasek, M.; Løvås, T. The effect of turbulence on the conversion of coal under blast furnace raceway conditions. *Fuel* **2023**, *331*, 125840, doi:10.1016/j.fuel.2022.125840.
15. Bösenhofer, M.; Wartha, E.-M.; Jordan, C.; Harasek, M. The Eddy Dissipation Concept—Analysis of Different Fine Structure Treatments for Classical Combustion. *Energies* **2018**, *11*, 1902, doi:10.3390/en11071902.
16. Sazhin, S.S.; Sazhina, E.M.; Faltsi-Saravelou, O.; Wild, P. The P-1 model for thermal radiation transfer: advantages and limitations. *Fuel* **1996**, *75*, 289–294, doi:10.1016/0016-2361(95)00269-3.
17. Putnam, A. Integratable form of droplet drag coefficient. *ARS Journal* **1961**, *31*, 1467–1468.

18. Mei, R. An approximate expression for the shear lift force on a spherical particle at finite Reynolds number. *International Journal of Multiphase Flow* **1992**, *18*, 145–147, doi:10.1016/0301-9322(92)90012-6.
19. P. Saffman. The lift on a small sphere in a slow shear flow. *Journal of Fluid Mechanics* **1965**.
20. GOSMAN, A.; IOANNIDES, E. Aspects of computer simulation of liquid-fuelled combustors. In *19th Aerospace Sciences Meeting*. 19th Aerospace Sciences Meeting, St. Louis, MO, U.S.A., 12 January 1981 - 15 January 1981; American Institute of Aeronautics and Astronautics: Reston, Virginia, 01121981.
21. W. Ranz; W.R.J. Marshall. Evaporation from drops : Part I. *Chemical Engineering Progress* **1952**, *48*, 141–146.
22. Singh, S.P.; Bansal, M.C. Combustion kinetics for soda black liquor-bagasse pith. *Energy Sources, Part A: Recovery, Utilization, and Environmental Effects* **2016**, *38*, 1197–1205, doi:10.1080/15567036.2014.899409.
23. Järvinen, M.; Zevenhoven, R.; Vakkilainen, E.; Forssén, M. Black liquor devolatilization and swelling—a detailed droplet model and experimental validation. *Biomass and Bioenergy* **2003**, *24*, 495–509, doi:10.1016/S0961-9534(02)00151-4.
24. Spalding, D.B. The combustion of liquid fuels. *Symposium (International) on Combustion* **1953**, *4*, 847–864, doi:10.1016/S0082-0784(53)80110-4.
25. Patricia Sierra Sanchez. MODELING THE DISPERSION AND EVAPORATION OF SPRAYS IN AERONAUTICAL COMBUSTION CHAMBERS; Institut National Polytechnique de Toulouse - INPT, 2012.
26. B. Zuo; A. Gomes; C. Rutland. Studies of Superheated Fuel Spray Structures and Vaporization in GDI engines **2001**.
27. Magnussen, B.F.; Hjertager, B.H. On mathematical modeling of turbulent combustion with special emphasis on soot formation and combustion. *Symposium (International) on Combustion* **1977**, *16*, 719–729, doi:10.1016/S0082-0784(77)80366-4.
28. Wartha, E.-M.; Bösenhofer, M.; Harasek, M. Characteristic Chemical Time Scales for Reactive Flow Modeling. *Combustion Science and Technology* **2021**, *193*, 2807–2832, doi:10.1080/00102202.2020.1760257.
29. Handbook of Hydraulic Resistance, 3rd Edn. By I. E. Idelchik. Begell House, 1994. 790 pp. ISBN 0-8493-9908-4. £138.95. *J. Fluid Mech.* **1998**, *354*, 376–378, doi:10.1017/S002211209726790X.
30. Mi, J.; Kalt, P.; Nathan, G.J. Near-Field Mixing Characteristics of Turbulent Jet Issuing from a Notched-Rectangular Orifice Plate. In *New trends in fluid mechanics research: Proceedings of the Fifth International Conference on Fluid Mechanics (Shanghai, 2007)*; Zhuang, F.G., Zhuang, F.-G., Li, J.-C., Eds.; Tsinghua Univ. Press; Springer: Beijing, Berlin, Heidelberg, 2008; pp 162–165, ISBN 978-3-540-75995-9.
31. Crnjin, F. *Truncated Weibull Distribution Functions and Moments*, 2015.
32. Järvinen, M., P. Numerical Modeling of the Drying, Devolatilization and Char Conversion Processes of Black Liquor Droplets. In *Pulp and Paper Industry: Chemical Recovery*; Pratima Bajpai, Ed.; Elsevier, 2017, ISBN 978-0-12-811103-1.

8 Figures

FIGURE 1: SIMPLIFIED SCHEME OF THE CHEMICAL RECOVERY WHEN SOOT FORMS DURING COMBUSTION.....	2
FIGURE 2: TOP LEFT: LAGRANGIAN PARTICLES; TOP RIGHT: EULERIAN FLOW; BOTTOM: EULERIAN-LAGRANGIAN APPROACH (VISUALIZATION INSPIRED BY HIRCHE ET AL. [11]).....	4
FIGURE 3: VISUALIZATION OF IMPLEMENTED COMBUSTION STEPS	8
FIGURE 4: TGA RESULT: TEMPERATURE AND MASS LOSS (WT% DRY MASS) OVER TIME IN N ₂ AND OXIDIZING ENVIRONMENT AFTER 100 MIN OF DRYING	9
FIGURE 5: MODEL PREDICTION FOR GROUPED VOLATILES AND EXPERIMENTAL MASS LOSS OVER TIME DURING DEVOLATILIZATION (T = 112 - 135 MIN).....	10
FIGURE 6: MODEL PREDICTION AND EXPERIMENTAL MASS LOSS OVER TIME DURING CHAR COMBUSTION (T = 143.2 MIN - 149 MIN).....	11
FIGURE 7: COMBUSTION VESSEL WITH INLETS AND OUTLETS (DIMENSIONAL GRID IN M)	14
FIGURE 8: HEAT EXCHANGER 1 TO 4 IN RED AND BROWN AND REFRACTORY LINING ZONE IN GREEN	15
FIGURE 9: CALCULATION MESH WITH FOUR DIFFERENT REFINEMENT LEVELS (LEFT: OVERALL COMBUSTION VESSEL, RIGHT: NOZZLE INLET AREA)	17
FIGURE 10: LEFT: RELATIVE VELOCITY ALONG THE CENTER LINE, RIGHT: RELATIVE VELOCITY ALONG 15° LINE; (X: DISTANCE FROM THE NOZZLE; DE: NOZZLE DIAMETER)	18
FIGURE 11: VARIED PARAMETERS OF VIRTUAL EXPERIMENTS.....	20
FIGURE 12: LEFT: LAGRANGIAN PARTICLES VISUALIZED SCALED BY FACTOR 10 COLORED BASED ON THE AGE IN S; RIGHT: SIMULATION RESULTS: LAGRANGIAN PARTICLES VISUALIZED SCALED BY FACTOR 10 COLORED BASED ON THE ASH WEIGHT FRACTION.....	22
FIGURE 13: LEFT: SIMULATION RESULTS FOR TEMPERATURE IN K IN EULERIAN FIELD; RIGHT: SIMULATION RESULTS FOR CO ₂ WEIGHT FRACTION IN EULERIAN FIELD	23
FIGURE 14: LEFT: SIMULATION RESULTS FOR VOLATILE WEIGHT FRACTION IN EULERIAN FIELD; RIGHT: SIMULATION RESULTS FOR SO ₂ WEIGHT FRACTION IN EULERIAN FIELD	24
FIGURE 15: COMBUSTION VESSEL WITH SIMULATED TEMPERATURE PROFILE IN K ON PLANE HIGHLIGHTED IN BLUE	25
FIGURE 16: DRY WT% OF CO ₂ , O ₂ AND SO ₂ AT THE TWO OUTLET PLANES.....	26
FIGURE 17: MEAN RELATIVE PARTICLE MASS M/M ₀ IN KG/KG OVER RESIDENCE TIME FOR THE EXPERIMENT 2MM, 30°, HOLLOWCONE	27
FIGURE 18: MEAN COMBUSTION TIME FOR A PARTICLE FOR THE DIFFERENT VIRTUAL EXPERIMENTS	28
FIGURE 19: MEAN PARTICLE MASS AS RELATIVE MASS M/M ₀ OVER TIME FOR MEAN DROPLET SIZE 2MM VS 3MM.....	29
FIGURE 20: MEAN PARTICLE MASS AS RELATIVE MASS M/M ₀ OVER TIME FOR SPRAYING ANGLE 15° VS 30°	31
FIGURE 21: MEAN PARTICLE MASS AS RELATIVE MASS M/M ₀ OVER TIME FOR SPRAY TYPE FULLCONE VS HOLLOWCONE	32

9 Tables

TABLE 1: ACTIVATION ENERGY E AND PRE-EXPONENTIAL FACTOR A FROM DATA FITTING	10
TABLE 2: FORCHHEIMER COEFFICIENTS F FOR HEAT EXCHANGERS 1 TO 4 IN 1/M	16
TABLE 3: HEAT SINK OF HEAT EXCHANGER 1 TO 4 IN MJ	16
TABLE 4: CELL VOLUME OF DIFFERENT REFINEMENT REGIONS SHOWN IN FIGURE 9	18
TABLE 5: ELEMENTAL COMPOSITION OF RED LIQUOR IN WT% DRY MASS	19
TABLE 6: PARAMETER SETTING IN VIRTUAL EXPERIMENTS	20
TABLE 7: GAS COMPOSITION IN VOL% DRY	25
TABLE 8: RESULTS OF DESIGN OF VIRTUAL EXPERIMENT	28
TABLE 9: CALCULATED INFLUENCE OF MEAN DROPLET SIZE ON PARTICLE COMBUSTION TIME	30
TABLE 10: CALCULATED INFLUENCE OF SPRAYING ANGLE ON PARTICLE COMBUSTION TIME	31
TABLE 11: CALCULATED INFLUENCE OF SPRAY TYPE ON PARTICLE COMBUSTION TIME	32